UNIVERSITEIT VAN PRETORIA
UNIVERSITY OF PRETORIA
YUNIBESITHI YA PRETORIA

A TRANSIENT COMPUTATIONAL FLUID DYNAMIC STUDY OF A LABORATORY-SCALE FLUORINE ELECTROLYSIS CELL

by Ryno Pretorius,

Supervisor: Prof. P.L. Crouse

Student Number: 25028996/04423372

Submitted in fulfilment of the requirements for the degree Masters in Chemical Engineering in the Faculty of Engineering, Built Environment and Information Technology University of Pretoria

Date of submission: 2011/07/07

A TRANSIENT COMPUTATIONAL FLUID DYNAMIC STUDY OF A LABORATORY-SCALE FLUORINE ELECTROLYSIS CELL

Synopsis

Fluorine gas is produced industrially by electrolysing hydrogen fluoride in a potassium acid fluoride electrolyte. Fluorine is produced at the carbon anode, while hydrogen is produced at the mild-steel cathode. The fluorine produced has a wide range of uses, most notably in the nuclear industry where it is used to separate ^{235}U and ^{238}U. The South African Nuclear Energy Corporation (Necsa) is a producer of fluorine and requested an investigation into the hydrodynamics of their electrolysis cells as part of a larger national initiative to beneficiate more of South Africa's large fluorspar deposits.

Due to the extremely corrosive and toxic environment inside a typical fluorine electrolysis reactor, the fluid dynamics in the reactor are not understood well enough. The harsh conditions make detailed experimental investigation of the reactors extremely dangerous. The objective of this project is to construct a model that can accurately predict the physical processes involved in the production of fluorine gas. The results of the simulation will be compared to experimental results from tests done on a lab-scale reactor. A good correlation between reality and the simulacrum would mean engineers and designers can interrogate the inner operation of said reactors safely, effortlessly and economically.

This contribution reports a time-dependent simulation of a fluorine-producing electrolysis reactor. COMSOL Multiphysics was used as a tool to construct a two dimensional model where the charge-, heat-, mass- and momentum transfer were fully coupled in one transient simulation. COMSOL is a finite element

analysis software package. It enables the user to specify the dimensions of his/her investigation and specify a set of partial differential equations, boundary conditions and starting values. These equations can be coupled to ensure that the complex interaction between the various physical phenomena can be taken into account - an absolute necessity in a model as complex as this one.

Results produced include a set of time dependent graphics where the charge-, heat-, mass- and momentum transfer inside the reactor and their development can be visualized clearly. The average liquid velocity in the reactor was also simulated and it was found that this value stabilises after around 90 s. The results of each transfer module are also shown at 100 s, where it is assumed that the simulation has achieved a quasi-steady state.

The reactor, on which the model is based, is currently under construction and will be operated under the same conditions as specified in the model. The reactor, constructed of stainless steel, has a transparent side window through which both electrodes can clearly be seen. Thus the bubble formation and flow in the reactor can be studied effectively. Temperature will be measured with a set of thermocouples imbedded in PTFE throughout the reactor. The electric field will similarly be measured using electric induction probes.

KEYWORDS: Fluid dynamics, fluorine electrolysis, coupled analysis, COMSOL Multiphysics, hydrodynamics

Contents

1 Introduction 1
2 Literature 4
2.1 Introduction 4
2.1.1 Gas Evolution 4
2.1.2 Metal Deposition 6
2.1.3 Other Electrolysis reactors 8
2.2 Historical 10
2.3 Industrial Manufacture of Fluorine 14
2.4 Description of a Fluorine Electrolysis Reactor 14
2.4.1 Basic Operations 14
2.4.2 Electrolyte 15
2.4.2.1 Electrolyte Properties 15
2.4.2.2 Electrolyte Manufacture and Specifications 20
2.4.3 Anode and Anode Phenomena 21
2.4.3.1 Polarisation 22
2.4.3.2 Overvoltage 23
2.4.4 Cathode, Cell-Body and Skirting 25
2.4.5 Reversible and Working Voltage 25
2.4.6 Heat Production and Energy Efficiency 26
2.4.7 Fundamental Equations for Transport in Diluted Solutions 27
2.4.8 Product Gasses 30
2.4.8.1 Hydrogen and Fluorine 30
2.4.8.2 Hydrogen Fluoride 31
2.5 Published Fluorine Cell Simulations 32
2.5.1 Modelling coupled transfers in an industrial fluorine electrolyser (Roustan et al., 1997) 32
2.5.2 Modeling of the Trajectories of the Hydrogen Bubbles in a Fluorine Production Cell (Hur et al., 2003) 38
2.5.3 Effect of hydrodynamics on Faradaic current efficiency in a fluorine electrolyser (Espinasse et al., 2006) 42

2.5.4 Electrochemical Engineering Modelling of the Electrodes Kinetic Properties during Two-Phase Sustainable Electrolysis (Mandin et al., 2009) 45

2.5.5 Modeling and Simulation of Dispersed Two-Phase Flow Transport Phenomena in Electrochemical Processes General Conclusion (Nierhaus *et al.,* 2009) 46

2.6 In summary 48

3 Model Development 51

3.1 Reactor Description 51

3.2 Model Description 51

3.2.1 Momentum Transfer 53

3.2.2 Heat Transfer 55

3.2.3 Charge Transfer 56

3.2.4 Mass Transfer 56

3.2.4.1 Electrode Reactions 57

3.2.5 Starting Conditions 58

3.2.6 Boundary Conditions 58

3.2.7 Constants 63

3.2.8 Expressions 64

3.2.9 Mathematical Solution 65

3.2.9.1 Solution Method 67

3.2.9.2 Meshing 68

3.2.9.3 Computing 73

4 Results and Discussion 75

4.1 Momentum Transfer 76

4.1.1 Time Progression 81

4.2 Heat Transfer 85

4.2.1 Time Progression 87

4.2.2 Parametric Study 89

4.3 Charge Transfer 92

4.4 Mass Transfer 98

4.4.1 Time Progression 100
4.5 Simulations of Published Results 103
4.5.1 Modelling coupled transfers in an industrial fluorine electrolyser (Roustan et al., 1997) 103
4.5.2 Effect of hydrodynamics on Faradaic current efficiency in a fluorine electrolyser (Espinasse et al., 2006) 108
5 Conclusions and Recommendations 112
5.1 Experimental Design Simulation 112
5.1.1 Momentum Transfer 112
5.1.2 Heat Transfer 113
5.1.3 Charge Transfer 114
5.1.4 Mass Transfer 114
5.2 Comparison with Published Results 115
5.2.1 Effect of hydrodynamics on Faradaic current efficiency in a fluorine electrolyser (Espinasse et al., 2006) 115
5.2.2 Modelling coupled transfers in an industrial fluorine electrolyser (Roustan et al., 1997) 115
6 Acknowledgments 116
7 References 116

Nomenclature

List of Symbols

Variable/Constant	*Description*	*Units*
C_i	Concentration of chemical species i	$mol \cdot m^{-3}$
$C_{0,i}$	Initial concentration of species i	$mol \cdot m^{-3}$
C_p	Heat capacity at constant pressure	$J \cdot kg^{-1} \cdot K^{-1}$
C_{p0}	Heat capacity at constant pressure at 25 °C	$J \cdot kg^{-1} \cdot K^{-1}$
d_b	Average bubble diameter	m
d_{ie}	Inter-electrode distance	m
D_i	Isotropic diffusion coefficient for chemical species i	$m^2 \cdot s^{-1}$
E	Electric field	$V \cdot m^{-1}$
$\vec{F}$	Volume force vector	$kg^2 \cdot s^{-2} \cdot m^{-2}$
F	Faradays constant	$A \cdot s \cdot mol^{-1}$
$\vec{g}$	Gravitational acceleration	$m \cdot s^{-2}$
i	Current density at specific point in reactor	$A \cdot m^{-2}$
i_n	Current density for electrode n	$A \cdot m^{-2}$
i_0	Exchange current density	$A \cdot m^{-2}$
I	Current	A
k_i	Electrode rate constants	$m \cdot s^{-1}$
$k_{t,i}$	Thermal conductivity of material i	$W \cdot m^{-1} \cdot K^{-1}$
$\vec{N}_i$	Molar flux of species i in the electrolyte	$mol \cdot m^{-2} \cdot s^{-1}$
n	Stoichiometric factor coefficient	(-)
$\vec{n}$	Normal vector	(-)
P	Pressure	kPa
p_i	Reaction order for anodic species	(-)
P_rtr	Pressure of atmosphere inside reactor	kPa

Q	Internal heat source	$W \cdot m^{-3}$
q	Internal heat source	W
q_i	Reaction order for cathodic species	(-)
R_g	Ideal gas constant	$J \cdot mol^{-1} \cdot K^{-1}$
R_i	Molar flux of species i from/into the electrode surface	$mol \cdot m^{-2} \cdot s^{-1}$
r_i	Reaction rate of specie i in the electrolyte	$mol \cdot m^{-3} \cdot s^{-1}$
s_i	Stoichiometric coefficient of species i in electrode reaction	(-)
T	Temperature of electrolyte	K
t	Time	s
T_0	Initial electrolyte temperature	K
T_w	Wall temperature in contact with heating jacket	K
$\vec{u}$	Velocity vector	$m \cdot s^{-1}$
z_i	Charge number of ionic species i	(-)

List of Greek Symbols

Variable/Constant	***Description***	***Units***
α_i	*Electron transfer coefficient*	(-)
β	Thermal expansion coefficient of electrolyte	$^{\circ}C^{-1}$
ε_r	Relative permittivity	(-)
ε	Cell current efficiency	(-)
Φ	Cell electric potential	V
$\Phi_{0,i}$	Reference potential of electrode i	V
Φ_{RV}	Reversible cell voltage	V
Φ_{TN}	Thermoneutral cell voltage	V

ϕ_i	Volume fraction of phase i	(-)
η_i	Viscosity of fluid phase i	$Pa \cdot s$
η_s	Surface overpotential	V
σ_i	Electrical conductivity of material i	$S \cdot m^{-1}$
$\mu_{m,i}$	Ionic mobility of species i	$m^2 \cdot mol \cdot J^{-1} \cdot s^{-1}$
ρ	Electrolyte density	$kg \cdot m^{-3}$
ρ_g	Ideal gas molar density	$kg \cdot mol^{-1}$
ρ_0	Electrolyte density at 25 °C	$kg \cdot m^{-3}$

1 Introduction

Fluorine gas is produced industrially *via* electrolysis of hydrogen fluoride (HF). Two gasses are liberated; *viz* hydrogen (H_2) and fluorine (F_2). Fluorine, the more valuable product, has a wide range of uses. Initially limited to the nuclear industry, other uses were found as fluorine became more readily available.

The Nuclear Energy Corporation of South Africa (NECSA) wishes to better understand the mechanism of gas evolution inside their fluorine electrolysis reactors. To date these reactors have been controlled using a black-box approach due to the hostile environment inside the reactors, which makes it very difficult and also dangerous to investigate the inner workings of the reactor adequately. A detailed simulation will provide the engineering team with a better understanding of these inner workings in order to optimise fluorine production.

The objective of this investigation is to construct a model that can accurately predict the physical processes involved in the production of fluorine gas. The specifications of a lab-scale fluorine cell were used for these simulations. This cell is currently under construction. Once completed the results of the simulation will be compared to the experimental data gathered.

A second set of simulations of fluorine cell data published in the open literature were conducted. The good correlation between the results achieved in this work and those in the literature serve as strong support of the accuracy of the modelling procedure followed. If satisfactory comparative results are obtained, modelling of the industrial scale reactor can commence. This knowledge will give design engineers a clearer idea of how to design and more efficiently operate fluorine electrolysis reactors.

Modelling was done on the software package COMSOL Multiphysics, which employs the Finite Element Method (FEM) to solve systems of partial differential

equations. Only the electrolyte phase is modelled incorporating the fundamental equations describing: electric field, mass-, heat- and momentum transport. The effects of the gaseous phase are included by modifying select liquid phase equations to include the effects of a gaseous phase.

Chapter two of this dissertation gives a review of electrolysis in general, industrial electrolysers and looks at fluorine electrolysis in more detail. The history of fluorine is investigated; its uses and production up to the industrial standard widely used today. The modern fluorine electrolysis reactor is then described in terms of all its components, products and reactants. This includes sections on electrolyte properties and manufacture, anode and anode phenomena, cathode, cell body and skirting characteristics, fundamental transport equations and product gas descriptions. This review takes a closer look at available published fluorine cell simulations. Data from this section are used for comparison with COMSOL simulations.

The third chapter describes the simulation, where the behaviour of the potassium acid fluoride $\left(KF \cdot 2HF\right)$ electrolyte is modelled. The stirring effects of the gaseous products due to convection are included in the simulations. This is done by using a modified Navier-Stokes equation that takes into account the gas phase by adjusting the equation with a volume fraction factor at each relevant term. All relevant equations for mass-, heat-, charge- and momentum transfer used during simulation are shown as well as the physical parameters used. The chapter is concluded with a section on the mathematical and FEM characteristics of the modelling process. The physical characteristics of the product gasses and the effects they have on the electrodes are beyond the scope of this investigation.

Results discussed in this investigation include graphical representations of the momentum-, heat-, charge- and mass transfer simulations. Time progression in the reactor is shown in each case where meaningful results were obtained. A

parametric study of the effect of varying the thermal conductivity of the electrolyte is also included. A detailed comparison is drawn between the COMSOL simulations and the published simulations.

Finally summary conclusions are drawn from the results, and a series of recommendations is made.

2 Literature

2.1 Introduction

Electrolysis is a branch of electrochemistry where a direct current is applied to drive an otherwise none-spontaneous reaction. It has high commercial importance where it is used to separate elements from ores and solutions *via* an electrolyte. The process requires a direct current to pass through an ionic substance (electrolyte) between two electrodes; the anode and cathode (Walsh, 1993: 13).

Metal, semi-conductor, conductive ceramics or polymers and graphite electrodes are commonly used. Carbon electrodes less commonly so, but are necessary in special electrolysers used during fluorine production. Ions and atoms are interchanged and electrons are removed or added *via* the external circuit. Charged ions are attracted to opposite electrodes. The products are collected and taken for further processing. Gasses are collected and purified whereas metals collect on the electrode surfaces. Energy required is the sum of change in Gibbs free energy plus other energy losses incurred in the system. The electric input commonly exceeds the required to facilitate the reaction; this energy is released in the form of heat (Walsh, 1993: 13).

Common industrial electrode processes include gas evolution, metal deposition, metal dissolution, transformation of existing surface phases, oxidation of a fuel, change in oxidation state of a solute metal ion and the hydrodimerisation of an activated olefin (Walsh, 1993: 17).

2.1.1 Gas Evolution

Chlorine

Chlorine was first produced electrochemically by Cruikshank in 1800, but was not economically viable. In 1892, advances in power generator and anode production

techniques made the production of chlorine gas from the chlor-alkali possible on an industrial scale. This process still produces most of the worlds chlorine gas supply (Schmittinger, 2003).

The chlor-alkali process intails passing a direct current through an aqueous solution of sodium chloride. This will in turn decompose the electrolyte to produce chlorine, hydrogen and sodium hydroxide solution. The three different processes used to produce chlorine are the diaphragm cell process, the mercury cell process and the more recently developed membrane cell process. Each method represents a different method of keeping the chlorine produced at the anode separate from the caustic soda and hydrogen produced at the cathode. Chlorine is also produced as a byproduct is the electrolysis of hydrochloric acid and molten alkali and alkaline earth metal chlorides. Chlorine production is the worlds largest consumer of industrial electricity and therefore the most significant gaseous product produced by electrolysis (Schmittinger, 2003).

Fluorine

Fluorine gas is produced from the electrolysis of hydrogen fluoride in an electrolyte and will be discussed at length in chapters to follow.

Hydrogen

Hydrogen, the most basic element, is mainly produced from hydrocarbons on an industrial scale, but can also be produced form by electrolysis or as a byproduct of electrolytic processes. Electrolytically produced hydrogen only accounts for 5% of global supply. An aqueous solution of ionic salts (used to increase the conductivity of water) is used as electrolyte and produces hydrogen at the cathode and oxygen at the anode. The cathode and cell body is constructed of steel or coated steel. The cell body is coated with a corrosion resistant material and the cathode is coated and/or acitivated with various catalysts to reduce hydrogen overvoltage. The anode can be constructed of nickel, or nickel coated steel (Häussinger *et al.*, 2003). Electrolytic hydrogen is very pure, but can contain

unwanted traces of oxygen, which can be removed by reaction with hydrogen over a platinum catalyst (Schmittinger, 2003).

Oxygen

Oxygen is produced industrially by various techniques, the most common technique being fractional distillation of air; it can also be produced as a side product during the electrolysis of water. The latter is also used to produce oxygen for space and underwater craft (Häussinger *et al.*, 2003).

2.1.2 Metal Deposition

This technique is used to produced amongst others the following metals: aluminium, lithium, potassium, sodium, magnesium and calcium. Some metals cannot be produced by the electrolysis of the metallic salt in a water solution dude to the reactivity of said metallic ion with water protons. This in turn leads to the production of hydrogen gas instead of the metal during electrolysis. The metallic salt is used instead, as this is water free medium.

Aluminium

Industrially aluminium is produced with the Hall-Héroult from alumina ore dissolved in cryolite. AlF_3 is added to the molten mixture to reduce the melting point of cryolite, lower surface tension, viscosity and density as well as decreasing the solubility of reduced species. Calcium and lithium fluoride can be added to further lower the operating temperature of this electrolysis cell. The mixture is electrolysed and results in liquid aluminium precipitation at the cathode, this precipitate then sinks to the bottom of the reactor due to the density difference of the metal and the electrolyte. The aluminium, removed *via* a vacuum operated syphon, is then transferred to be cast into ingots. The carbon anode in turn oxidises as it reacts with oxygen produced at this electrode. Other gases produced include CO_2, as the carbon anode is consumed and HF, from the AlF_3 (Frank *et al.,* 2003).

Copper

Electrolysis is used to further refine copper that is intended for use in the electrical industry. Impure copper anodes are dissolved electrolytically in acidic copper sulphate solutions. The copper is then deposited onto stainless steel cathodes. The plated copper is then removed from the stainless steel plates and sent for further processing. Impurities are then collected as sludge from the bottom of the electrolysers (Seidel, 2004, a).

Lithium

Lithium is found in nature in mineral deposits and brine solutions. The salt is usually carbonated and chlorinated before the lithium is extracted. Most commonly it is produced from the electrolysis of the molten salt chloride solution which usually contains potassium chloride as a supporting electrolyte in a Downs cell. Potassium has a higher decomposition potential than that of lithium and will not interfere with lithium production. Cells are fabricated from low 0.25-.03% steel or carbon steel. An alternative method to produce lithium is *via* electrolysis in non-protic solvents (Seidel, 2004, f).

Magnesium

Three main electrolytic production techniques exist for the production of magnesium metal, al involve the electrolysis of molten magnesium chloride, but differ in the preparation of the electrolyte, cell design and by-product treatment. Chloride is produced as by-product and can be recycled or sold. Molten magnesium is sent for processing and is cast as ingots. A graphite anode is used in conjunction with a steel cathode surrounding each anode (Seidel, 2004, c).

Potassium

Potassium metal was first produced from the electrolysis of potassium hydroxide. Later electrolysis methods use an electrolyte comprised of KOH, K_2CO_3 and KCl. The Downs process can also be utilised to manufacture potassium metal.

Electrolytic manufacture of potassium metal has fallen out of favour for the more commercially viable process of producing potassium from the reaction of the halide salt with sodium or calcium-carbide to produce potassium and a metallic halide salt (Burkhardt *et al.*, 2003).

Sodium

Commercial production of sodium is done *via* the electrolysis of molten sodium chloride in a reactor known as the Downs cell. In this process calcium chloride is added to lower the melting point of the electrolyte, as the higher decomposition potential of calcium will not compromise the purity of the sodium metal. The cell consists of several graphite anodes surrounded by steel cathodes. Chlorine is produced at the one electrode and a mixture of molten calcium and magnesium metal at the other. The mixture is cooled to precipitate calcium metal (Seidel, 2004, c).

Zinc

The electrolytic recovery of zinc is favourable in complex ores that do not lend themselves to pyrometallurgical processes where zinc cannot be concentrated to significant levels. The zinc mineral is oxidised to a crude oxide and leached with return acids from cells. The zinc sulphate solution is purified and electrolysed (Seidel, 2004, e).

2.1.3 Other Electrolysis reactors

Electrochemical machining

ElectroChemical Machining (ECM) offers an alternative way of machining hard surfaces without degrading the tools used to do the machining. The process can be used to smooth surfaces, drill holes and form complex shapes (where the anode takes the shape of the cahode). The metal to be machined (for example iron) is connected to the positive end of a direct current supply (where the metal is dissolved), the dissolved metal then precipitates as a metal-hydroxide (in the

case of iron). A gas (usually hydrogen) forms at the cathode. This method is used in the following industries: aircraft engine industry, medical industry, car industry, offshore industry, manufacturing industry, electronics and several hybrid ECM processes (Seidel, 2004, b).

Electroplating

During electroplating or electrodeposition ions of a dissolved metal are plated onto a metallic, or even non-metal electrode (cathode) surface, with the advent of a direct current. The dissolved metal is either dissolved from the anode and/or added as a salt. The anode metal is dissolved (oxidised) and plated (reduced) at the cathode. The deposited layer imparts the properties (abrasion, aesthetic, corrosion and wear resistance) of a more expensive metal to a cheap metal surface or to build up the metal thickness of undersized parts. Commonly coated metals are cadnium, chromium, copper, gold, silver, nickel, tin and zinc (Seidel, 2004, e).

Electrowinning

Electrowinnig can occur from aqueous solutions or fused molten salts. In the first case the metal ore is converted into an acid-soluble form, leached with an acid, leached solution is purified/concentrated and finally the metal solution is electrolysed where the metal is deposited on the cathode, done during copper/zinc metal purification/production. The latter case is where the metallic salt is electrolysed in its molten state as discussed in previous sections where Aluminium, Sodium Lithium and Magnesium metal production is discussed (Seidel, 2004, c).

Organic electrochemistry

Organic electrochemical reactors facilitate an electroorganic reaction where an organic substance is chemically transformed by an electric current. This technique has been most successfully implemented in the fine chemicals area.

Pharmaceutical intermediates and high value added chemicals are produced in medium to small scale production faculties (Seidel, 2004, d).

Sodium hydroxide

Sodium hydroxide is most commonly produced from the electrolysis of sodium chloride in aqueous solution; this process produces a sodium hydroxide solution and forms hydrogen and chlorine gas. To create sodium hydroxide crystals, the solution is evaporated until the water content becomes low enough (Minz, 2003)

2.2 Historical

C.W. Scheele discovered fluorine in 1771 (Groult, 2003). Edmond Fremy was the first to produce small quantities of fluorine gas by the electrolysis of fused fluorides (Rudge, 1971: 2). It was however Ferdinand Frederick Henri Moissan who first produced fluorine in 1886 by the electrolysis of a solution of potassium hydrogen fluoride in liquid hydrogen fluoride.

The electrolysis was done in solution due to the low conductivity of hydrogen fluoride and iridium/platinum electrodes were used. The reaction chamber was cooled to -50 °C to lower the partial pressure of hydrogen fluoride. Moissan won a Nobel Prize for this cell, which would later be known as a “low temperature cell” (Groult *et al.,* 2007). He died in 1907 shortly after returning from Stockholm. The belief is widely held that he died due to his work with fluorine causing him to develop acute appendicitis. It is however a contentious issue as to how his work with fluorine could cause appendicitis.

Moissan’s work with low temperature electrolysis of fluorine was continued by Otto Ruff, using what was essentially a copy of Moissan’s cell. The high temperature cell was pioneered in 1919 by Argo and co-workers, where molten anhydrous potassium acid fluoride at 239 °C was used as an electrolyte with a graphite anode within a cathodic copper container (Rudge, 1971:1-3).

The modern medium temperature cell was first used by Lebeau and Damiens in 1925 using a 51 % molar percentage of hydrogen fluoride, reducing the melting point to 65.8 °C. This was also the first time a nickel anode was used, reducing polarisation problems previously experienced. This work was later refined by Cady in 1942 where a 41 % hydrogen fluoride composition $(KF \cdot 2HF)$ gave the system a melting point of 71.7 °C. Cady used a nickel or non-graphitic carbon anode, reducing polarisation problems and solving the disintegration and swelling problems graphite anodes experience in $KF \cdot 2HF$. Cady's work was the final nail in the coffin of all other configurations and operating temperatures of fluorine cells and is now used as standard (Rudge, 1971:1-3).

It was not until the discovery of nuclear fission and all the possibilities it presented that fluorine production was escalated from purely academic to industrial scale manufacture. Fluorine is used in the preparation of uranium hexafluoride (UF_6), made from uranium tetrafluoride (UF_4), for the diffusional or centrifugal separation of ^{235}U and ^{238}U (Rudge, 1971:3-5). Uranium tetrafluoride (UF_4) is manufactured by reacting uranium dioxide with hydrogen fluoride, a precursor used in fluorine gas manufacture (Clark *et al.,* 2005). Uranium hexafluoride is produced by the following equation (Groult, 2003):

$$UF_4 + F_2 \rightarrow UF_6$$

The main consumers of fluorine gas in this early era were the American “Manhattan Project” and the British “Tube Alloy” project for the purposes of nuclear weapon development. Fluorine production at this stage was done with nickel anodes, which didn’t present a commercial future due to the high corrosion rates of the nickel anodes, nickel fluoride sludge formation and limited current efficiency (Rudge, 1971:3-5).

Germany also took major strides during the war years, for purposes of atomic energy investigations and principally the incendiary agent chlorine trifluoride. The only German plant of sizable capacity, Falkenhagen near Berlin, was capable of producing 600 to 700 tons per year. The plant consisted of 60 high temperature cells with silver cathodes, indicating the importance the Germans attached to the production of fluorine gas during World War II (Rudge, 1971:5-6).

Fluorine is also widely used in the polymer industry. Polyolefin and other plastic containers can be treated with fluorine to make them resistant to permeation and solution by polar solvents contained within. Other polymer surfaces (polyethylene, polypropylene, rubber, polyester and aramid among others) are treated with fluorine to improve significantly surface adhesion and dispersion properties (Shia, 2005).

A wide variety of fluorine inorganic compounds are produced and used. Sulphur hexafluoride (SF_6), a gaseous highly dielectric compound, whose electrical- and thermal stability and ease of handling has made it a sought-after insulating medium for the production of high voltage electrical switch gear, breakers and substations (Shia, 2005).

Sulphur tetrafluoride (SF_4) is produced under controlled reaction conditions with sulphur and fluorine. It is most commonly used to form fluorochemical intermediates in the herbicidal and pharmaceutical industries due to its selective fluorination capability. Fluoro-halogen products include chlorine trifluoride, used in UF_6 processing and bromine trifluoride, used by the oil well industry in chemical cutting. Iodine- and antimony pentafluorides are used as selective fluorinating agents to produce fluorochemical intermediates. Boron trifluoride (BF_3) can be used as a polymerization initiator, a catalyst in some isomerization, alkylation, esterification, sulfonation reactions and as flux for magnesium soldering (Shia, 2005).

Ammonium bifluoride (NH_4HF_2), finds uses in the chemical industry as a fluorinating agent, textile industry as neutralizer for alkalides, the metal industry by pickling stainless steel and pre-treatment of metals before phosphating, galvanizing or nickel plating. Other uses of ammonium bifluoride include preservation of wood (Shia, 2005).

Lithium hexafluorophosphate $(LiPF_6)$ is widely used in the notebook computer, mobile phone, consumer electronics and electrical vehicle industries, where it is used as electrolyte in lithium-ion batteries (CHENCO GmbH, 2007). Other inorganic fluorochemicals include NF_3 (used to plasma etch silicon wafers and in plasma-enhanced vapour deposition) and XeF_2 (used as strong fluorinating agent and in etching of silicon in the production of micro-electromagnetic systems), while primary lithium batteries use graphite fluorides electrodes as cathodes. Graphite fluorides are also used as lubricating agents (Groult, 2003).

Fluorination of metals like tungsten and rhenium produces the respective volatile metal hexafluorides (WF_6 and ReF_6). The vapours produced are employed in the chemical vapour deposition industry to produce metal coatings and finely formed components (Shia, 2005). Aluminium fluoride (AlF_3) and cryolite (Na_3AlF_6) are used in aluminium refinement as a flux; they lower the melting temperature and increase the conductivity of the electrolyte during electrolysis (CHENCO GmbH, 2007).

Fluorinated organic materials are produced using fluorine. The first organic fluorinated materials that come to mind are HydroFluoroCarbons (HFCs) used as refrigerants (CHENCO GmbH, 2007). Other uses include regiospecific introduction of fluorine into bio-systems for cancer treatment, as well as the manufacture of perfluorinated materials. The high thermal and chemical stability of perfluorocarbons makes them ideal for high temperature lubrication, thermal

testing of electronic components and speciality fluids for various pumping and hydraulic applications. The high solubility of oxygen in perfluorocarbons (specifically perfluorinated aliphatics and cycloaliphatics) has led to their use as synthetic blood substitutes (Shia, 2005).

2.3 Industrial Manufacture of Fluorine

Three basic steps are required to manufacture elemental fluorine, namely (Klose, 2004: 56):

- Conversion of fluorspar into anhydrous hydrogen fluoride according to Equation 2-1.

$$CaF_2 + H_2SO_4 \rightarrow CaSO_4 + 2HF \qquad 2\text{-}1$$

- Electrolysis of hydrogen fluoride (HF) in molten potassium acid fluoride ($KF \cdot 2HF$) resulting in the formation of fluorine gas, according to Equation 2-2.

$$2HF \rightarrow H_2 + F_2 \qquad 2\text{-}2$$

- Purification of fluorine gas by a separation process.

2.4 Description of a Fluorine Electrolysis Reactor

2.4.1 Basic Operations

Fluorine gas production takes place in an electrolysis cell where a molten potassium acid fluoride electrolyte ($KF \cdot 2HF$, 40.8 mass percentage HF) is subjected to an electric field (Groult, 2003). Fluorine gas is liberated at the anode and hydrogen gas at the cathode. Hydrogen fluoride cannot be used due to its low electrical conductivity (Shia, 2005). Industrial cells typically operate at $6\ kA$

utilizing 30 plate carbon anodes. Cooling is required and a high current efficiency expected. However, low energy efficiency is common (Groult, 2003), 18 % is considered commonplace (Rudge, 1971:45). Bubble formation and motion are major sources of flow in the electrolysis cell. The hydrodynamic properties of the electrolyte and the efficiency of the electrolysis reaction are strongly coupled to the flow of bubbles in the reactor. This is also true for diluted species transport and electrical performance. This is due to the stirring effect of bubble motion and the high resistivity of bubbles compared to that of the electrolyte (Mandin *et al.*, 2009).

2.4.2 Electrolyte

As mentioned above, a fluorine-containing salt (potassium acid fluoride) is used as an electrolyte due to the low electrical conductivity of pure HF. The fluorine containing salt is heated to just above melting point and held at this temperature during electrolysis. It is critical that the solution stays above its melting point to ensure fluidity. Electrolyte entrained with exiting gas streams can solidify in the gas outlets; this can cause clogging and leads to dangerous explosions caused by explosive recombination of hydrogen and fluorine gas (Shia, 2005).

2.4.2.1 Electrolyte Properties

Modern fluorine electrolysis cells use $KF \cdot 2HF$ as the electrolyte salt. The reason $KF \cdot 2HF$ is specifically used as the potassium fluoride salt is due to the melting point of the salt at the given composition (40.8 % HF), see Figure 2-1. Another consideration is the partial pressure of hydrogen fluoride over the potassium fluoride/hydrogen fluoride system and its variations with composition and temperature; see Figure 2-2 (Rudge, 1971: 7-9).

The usual working limits are a hydrogen fluoride content of between 38 % and 42 %, with the operating temperature ranging between 80 °C and 110 °C. The

specific mole fraction of HF in $KF \cdot 2HF$ ensures a low HF partial pressure at a convenient operating temperature. It was found that it is advantageous to operate cells at low hydrogen fluoride concentrations and at lower temperatures, minimizing loss of hydrogen fluoride in the product streams. It is, however, required to strike a balance between hydrogen fluoride loss (and by extension, removal later in the process) and an increase in working voltage. As the operating temperature and hydrogen fluoride concentration decrease the conductivity of the electrolyte decreases, requiring a higher voltage to maintain the same production rate (Rudge, 1971: 7-9).

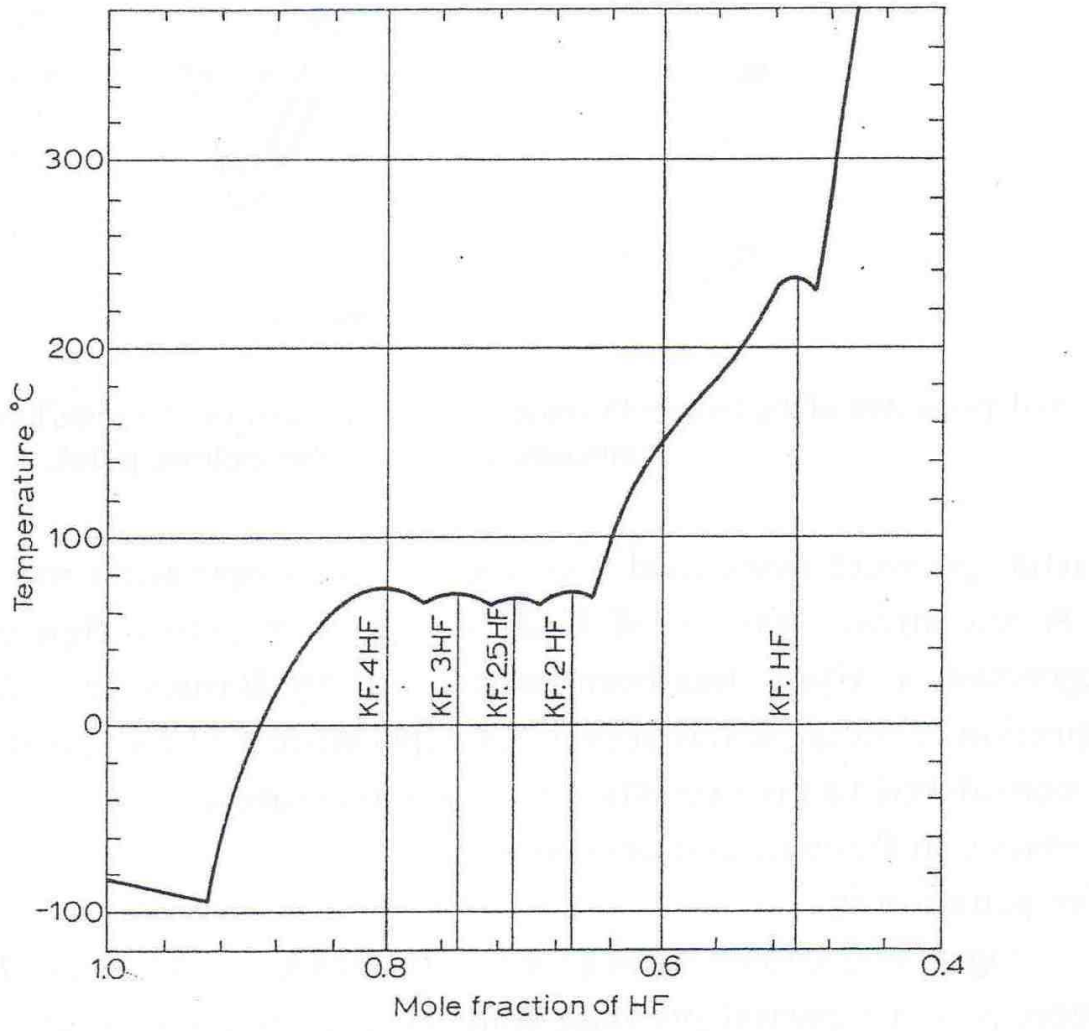

Figure 2-1: Melting point versus composition diagram for a potassium fluoride/hydrogen fluoride system (Rudge, 1971).

Electrolyte density variation with temperature is shown in Figure 2-3, while electrolyte conductivity over the range 37 to 45 % hydrogen fluoride at 80 °C to 100 °C is given by Figure 2-4 (Rudge, 1971: 10-11).

Another property to consider is the surface tension of the various electrolyte mixtures. This is due to the effects surface tension has on the phenomena occurring on the carbon anodes. Surface tension decreases with an increase in temperature. A reduction in HF concentration increases the electrolyte surface tension; for each 1 % increase in HF content a surface tension decrease of about 2.5 dyne/cm is observed. It was found that water has only a small effect on surface tension, but a myriad of negative effects on the fluorine production process (Rudge, 1971: 10-12).

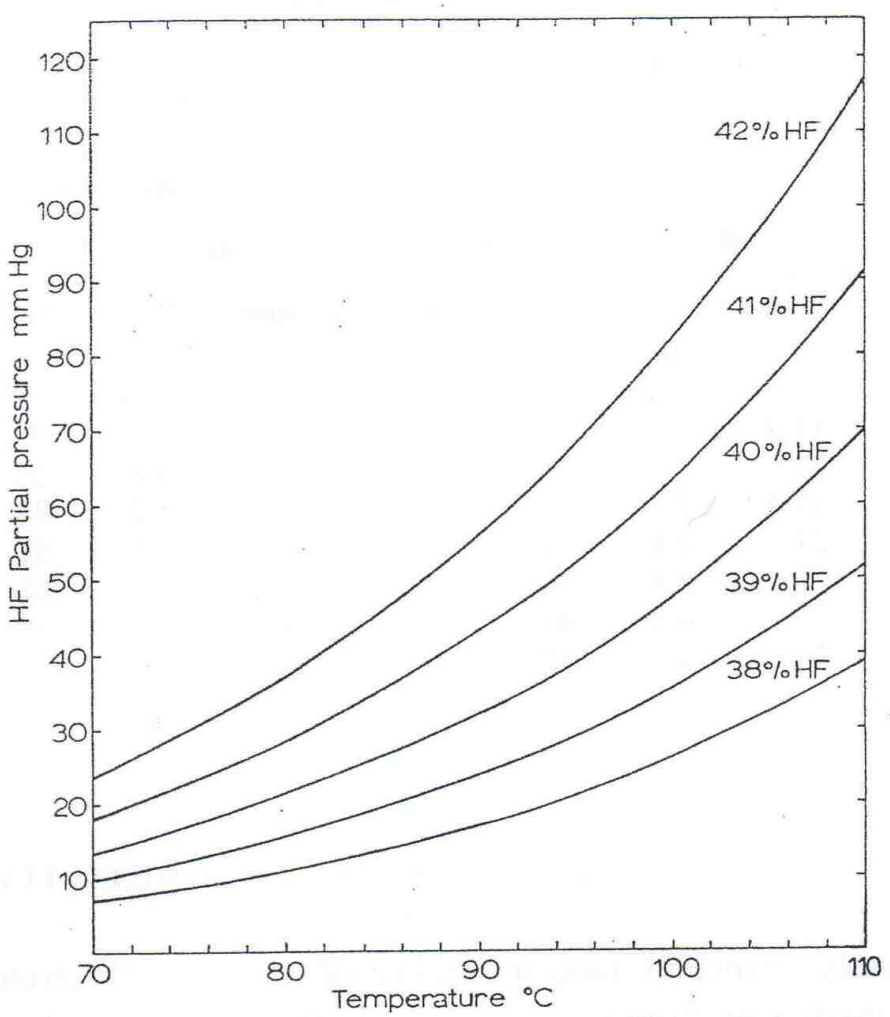

Figure 2-2: Partial pressures of hydrogen fluoride over potassium fluoride/hydrogen fluoride system of varying compositions, for various electrolyte temperatures (Rudge, 1971).

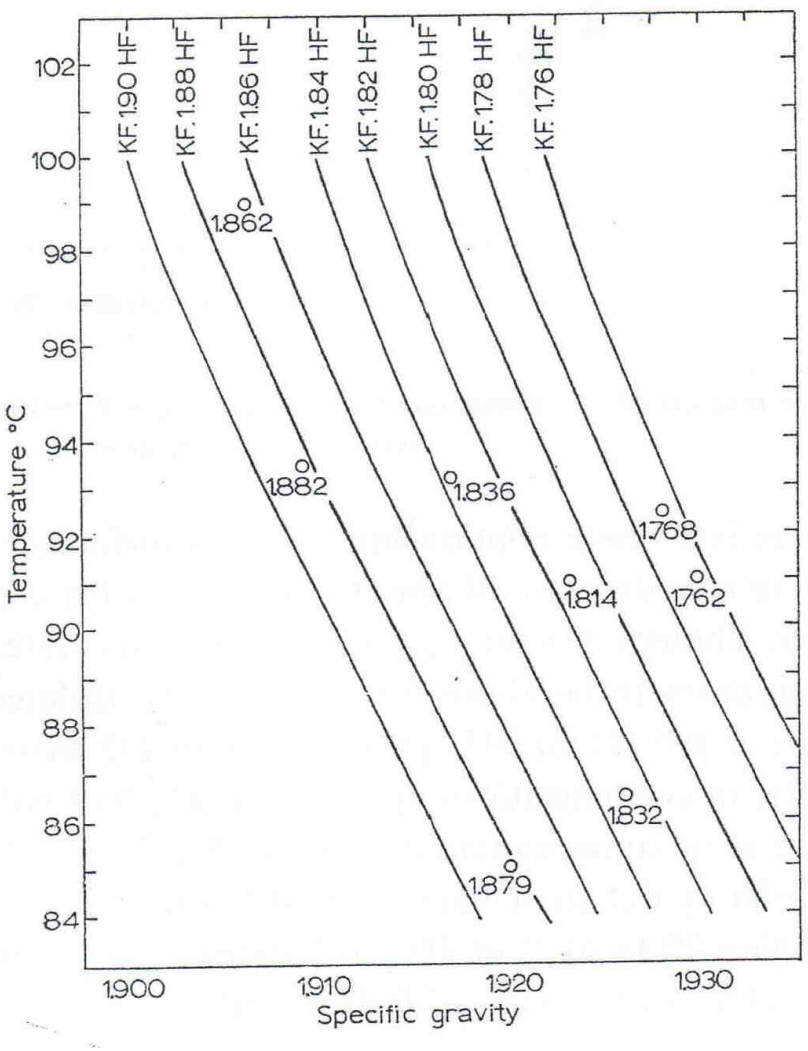

Figure 2-3: Potassium fluoride/hydrogen fluoride electrolyte density at various compositions and varying with temperature (Rudge, 1971).

A density variation for the electrolyte as a function of temperature and constant acid number was derived from Figure 2-3. It was assumed that the gradient of density variation with temperature remains a constant for any acid number of potassium acid fluorides. The equation was then adjusted for acid number by specifying the density of the specific potassium acid fluoride mixture at 25 °C. The volume expansivity of the electrolyte was predicted using Equation 2-3 (Smith *et al.*, 2005: 69). An insignificant isothermal compressibility was assumed.

$$\rho = \rho_0 / e^{\beta(T-25^\circ C)} \qquad 2\text{-}3$$

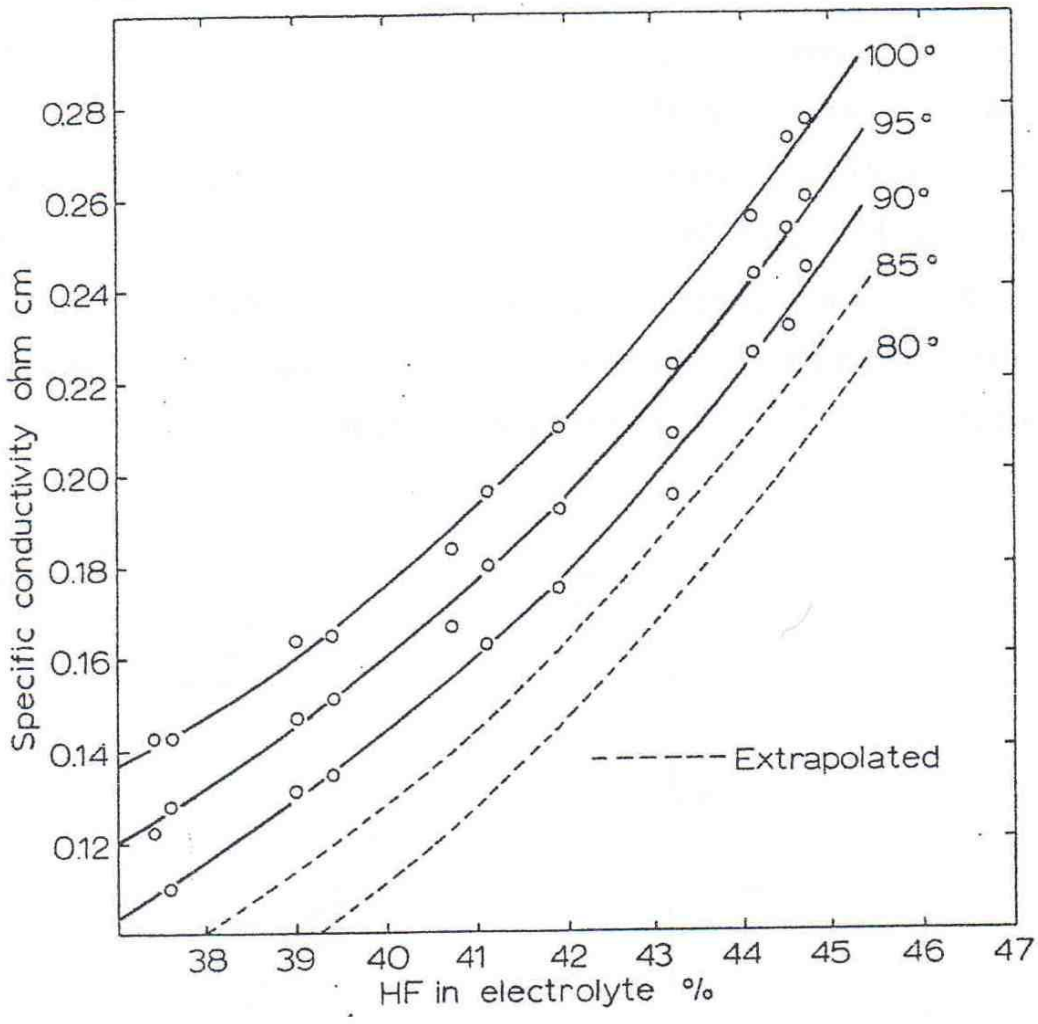

Figure 2-4: Potassium fluoride/hydrogen fluoride electrolyte conductivity, with variation in hydrogen fluoride composition, for various temperatures (Rudge, 1971).

2.4.2.2 Electrolyte Manufacture and Specifications

Electrolyte is manufactured by adding liquid hydrogen fluoride to solid potassium fluoride in a steam jacketed steel vessel, with cooling water regulating the exothermic reaction. This is done until sufficient product is produced to cover a dip-pipe used to introduce liquid hydrogen fluoride. The vessel is then heated

and agitated, while liquid hydrogen fluoride is introduced, until the required composition is reached. Excess hydrogen fluoride is removed and moved to an absorption system. Composition is regulated by measuring the liquid height in the tank and therefore the corresponding density. Electrolysis only removes hydrogen fluoride from the electrolyte. HF can easily be replaced during electrolysis (Rudge, 1971: 13 and Crouse, 2010).

Composition specifications vary from manufacturer to manufacturer. Two important and common specifications are low water and sulphur contents. Heavy metal specification is far more inconsistent. Some manufacturers add certain metals to affect fluorine production efficiency. Metals like Al and Mg modify the carbon fluoride surface film, increasing charge transfer by formal traces of metal fluorides (Rudge, 1971: 13 and Groult, 2003).

2.4.3 Anode and Anode Phenomena

Anodes are manufactured from non-graphitized carbon. Anodes manufactured from graphite were found to be unsuitable since exfoliation takes place due to intercalation of the constituents of the melt between the lamellar graphene layers (Groult, 2003).

Anodes are manufactured from petroleum coke and a pitch blend calcined at low enough temperatures to prevent graphitisation. Carbon is used because it has low electrical resistivity, high strength and resistant to fluorine attack. During electrolysis of potassium bifluoride, fluorine gas is produced at the positive electrode or anode (Shia, 2005).

The anode connection is considered to have the most detrimental effect on anode lifetime. During the anode lifetime, contact resistance has a tendency to cause corrosion of the metallic contacts causing the carbon anode to break due to contact loss. The resultant reduced contact area leads to the overheating and

burning of the remaining carbon still in contact with the current source, which eventually causes catastrophic failure of the anode (Rudge, 1971: 44).

2.4.3.1 Polarisation

Polarisation is defined as the condition under which, at a fixed voltage, a decrease occurs in the current flowing through the cell to a value which is significantly smaller than normal operating currents. The decrease can be sudden or gradual. The polarisation problem, essentially an anodic problem, has plagued both high and medium temperature carbon anode fluorine cells from the earliest years. The problem, first reported by Argo and co-workers in 1919, was attributed to the “non-wetting” effect of the electrolyte on the graphite. It was found that a carbon anode is initially wettable by the electrolyte but even after a brief current exposure time the contact angle increases to 150º and is no longer “wetted” by the melt. It has been contributed to the presence of the intercalation compound $(CF)_n$, later confirmed with X-ray analysis (Rudge, 1971: 15-18). Electro-polishing of the surface at higher voltages leads to enhanced fluorine evolution by making the surface more easily wettable (Crassous *et al.,* 2009). This large contact angle resulted in the formation of lenticular fluorine bubbles that tend to stick to the anode surface. Bubbles do not detach easily and slip up the electrode due buoyancy forces, coalescence or passing of gas from one bubble to another (Rudge, 1971: 15-18). In order to prevent the formation of graphite-oxides $(C_xO(OH)_y)$, the water concentration must be kept very low (below 20 ppm). These graphite oxides in turn form the graphite fluoride film during fluorination of the electrolyte (Groult *et al.,* 2000).

Suggested methods to overcome film formation are either controlling the compounds in the electrolyte or by preventing gas bubble accumulation. Water content must be minimised (as previously mentioned), addition of nickel salts (like nickel fluoride) have been proven effective. Preliminary electrolysis of the electrolyte with a nickel anode reduces water content and introduces nickel into

the electrolyte, although the beneficial nickel effect is usually transient when introduced *via* electrolysis. Nickel salt addition is a more permanent solution to the problem. In the case of the latter solution, porous electrodes have been shown to be effective. The pores must, however, not be large enough to be flooded by the electrolyte (Rudge, 1971:21-25).

2.4.3.2 Overvoltage

Anode overvoltage accounts for more than 30 % of the cell's 9-12 V operating voltage (Shia, 2005). XPS studies have shown that a carbon fluoride film forms on the surface of the anode and causes this overvoltage, the same film responsible for polarisation in the previous section. Electrons may be transferred easily to the electrolyte through the $C-F$ film on the anode during fluorine evolution, but the overall composition of the film makes it more difficult (Groult *et al*., 2000). It has been established that the carbon fluoride film is composed of graphite intercalation compounds (GICs) where the $C-F$ bonds are ionic and/or semi-ionic and non-conducting graphite fluorides (CF_x) (Groult, 2003).

The trace graphite fluorides are presumed to inhibit charge transfer. Electric charge transfer is impeded and contact with the electrolyte is lost due to the low electrical conductivity of the film and the fact that it is strongly non-wetting. A further consequence of the non-wetting characteristics of fluorinated carbon is the clinging of lenticular fluorine bubbles to the anode surface reducing its effective surface area. A typical contact angle of the fluorine bubble with the anode is between 120 and 160 degrees, explained by the capability of the low surface energy fluorinated carbon film to repulse the electrolyte. Overvoltage is caused by a carbon fluoride $(C-F)$ solid layer and a fluidized layer composed of electro-active species (HF_2^-, K^+, HF), that diffuse spontaneously under the gaseous film adding significant resistance (Groult, 2003).

Thermodynamically HF decomposition requires a potential of 2.9 V, but an anode-cathode voltage of 8-10 V is required to maintain a current density of 10-12 $A \cdot dm^{-2}$ in industrial cells. The total voltage is the sum of five contributions (Groult, 2003):

- Reversible decomposition voltage (≈2.9 V)
- Ohmic drop in the electrolyte (≈3 V)
- Ohmic drop in the electrodes (≈0.5 V)
- Cathode overvoltage (≈0.2 V)
- Anode overvoltage (≈2.5 V)

The high anode overvoltage is attributed to the carbon fluoride layer and the fluidized layer on the anode, this film causes poor wettability of the electrode, which in turn results in a small electro-active area (Groult, 2003; Groult *et al.*, 2000).

The areas not covered by the bubbles now experience all the charge transfer and become overheated due to the high current density in this relatively small area and can result in electrode breakdown, possibly by vaporisation. This effect shifts position as the bubbles move up the electrode, causing a visible sparking effect, possibly due to incandescence of the fluorine gas or heat of reaction of fluorine with the anode. This effect is sometimes called the “Anode Effect” and serves to electro-polish the anode, by burning off the carbon fluoride layer. Excessive water leads to faster electrode erosion, as water facilitates the carbon fluoride layer production (Rudge, 1971: 19-20).

The unusually high overpotential experienced in a fluorine electrolyser results in a strong irreversibility at each electrode leading to significant current losses due to heat generation. This interaction necessitates the coupling of the electrical and thermal transfer phenomena (Roustan *et al.,* 1997).

2.4.4 Cathode, Cell-Body and Skirting

Electrolysis of potassium bifluoride results in hydrogen gas production at the negative electrode (cathode). The cathode and cell-body are mostly manufactured from steel or Monel, but steel is generally used due to its lower cost.

Skirting is used to separate the hydrogen and fluorine gas compartments and is usually manufactured from magnesium or Monel (Shia, 2005). The skirt can however also be manufactured from steel if cost is an issue, at the cost of reactor durability. The presence of the skirt means that the distance between the anode and cathode is large. This in turn results in a large Ohmic drop (Roustan *et al.,* 1997).

During electrolysis it was found that cathode polarisation appears concurrently with the development of bipolarity of metal parts interposed between cathode and anode. This phenomenon is especially relevant with regard to the diaphragm skirt. Bipolarisation causes hydrogen to form in the fluorine compartment, which could cause explosions at higher bipolar hydrogen production rates. Bipolarity may also cause erosion of the skirt. In practice perforations of the interposed areas between the electrodes prevent the onset of the bipolarisation effect (Schumb *et al.,* 1947).

2.4.5 Reversible and Working Voltage

The reversible cell voltage (Φ_{RV}) or thermodynamic decomposition voltage is the minimum potential required for product formation during electrolysis. The electromotive force (emf) is the reversible cell voltage, but of opposite sign. The reversible cell voltage is the difference between the reversible electrode potentials. A typical industrial fluorine electrolyser has a reversible cell voltage of around $2.9\ V$ (Rudge, 1971: 34, Heitz & Kreysa, 1986:93-101). The working voltage is the voltage applied in cells during operation and is increased to values

higher than the reversible voltage to achieve desired current densities. These additional energy components are introduced irreversibly as a result of cell overvoltages (activation-, diffusion- and reaction-) and IR-drop in the electrolyte, electrode connectors and at the electrodes (Heitz & Kreysa, 1986:76-77).

2.4.6 Heat Production and Energy Efficiency

The thermodynamic decomposition voltage (reversible cell voltage) of an electrochemical reaction corresponds to the free energy change of that reaction. The difference between the free energy and enthalpy of the reaction is reversibly exchanged with the environment. For practical purposes it is useful to consider isothermal operation, this is achieved by exchange with the environment or additional electrical input. The term thermoneutral voltage refers to the voltage required to operate the cell isothermally. The difference between the cell voltage and the reversible voltage is the amount of heat produced within a cell and is given by Equation 2-4 (Heitz & Kreysa, 1986:75-77, Roustan *et al.*, 1997):

$$q = I \cdot \left(\Phi - \Phi_{TN}\right) \qquad 2\text{-}4$$

A similar equation is given by Rudge (1971: 34) in Equation 2-5:

$$q = I \cdot \left(\Phi - \Phi_{RV}\right) \qquad 2\text{-}5$$

Most cells operate at lower current efficiencies; recombination of fluorine and hydrogen is the main cause of low current efficiency. Allowance has been made for this in the form of the following empirical equation (Equation 2-6) that can be added into the heat production equation (Rudge, 1971: 34).

$$q\,(\text{additional}) = I \cdot \left[2.81 \cdot \frac{\left(100 - \varepsilon\right)}{100}\right] \qquad 2\text{-}6$$

Equations 2-5 and 2-6 are modified to utilize current density instead of current and combined into Equation 3-5 to give the total heat loss term in the fluorine electrolysis cell. A further modification was required to attain the correct units for Equation 3-5; division by the inter electrode distance of 60 mm. This modification is justified by the fact that the model has a linear potential drop between the electrodes. The potential drop should in fact exponentially drop off next to the electrodes, however.

The equations provided by Rudge (1971) were used, as the reversible cell voltage is a known value, whereas the value for the thermoneutral voltage was not mentioned by Roustan *et al.* (1997).

Heat is also generated within the electrodes, this amount of heat generated can be calculated using Equation 2-7. This equation provides a heat generation value in units of $W \cdot m^{-3}$.

$$Q = i \cdot E \qquad 2\text{-}7$$

Equation 2-7 would have had to be used if the potential drop between electrodes were not linear as explained above.

2.4.7 Fundamental Equations for Transport in Diluted Solutions

During electrolysis ions are driven through the solution by the electric field; positive ions (cations) are driven towards the negative electrode (cathode) and negative ions (anions) are driven towards the positive electrode (anode). The flux of a solute species due to electric field migration, diffusion in a concentration gradient, and convection with the fluid velocity is given by the right hand side of Equation 2-8 (Newman, 1991: 3):

$$\vec{N}_i = -z_i \mu_i F C_i \nabla \Phi - D_i \nabla C_i + \bar{u} C_i \qquad 2\text{-}8$$

The ionic flux is proportional to the charge on the ion and the magnitude of the electric field, *i.e.* the negative of the gradient of electrical potential (Newman, 1991: 3). Diffusion, a function of a diffusion coefficient and concentration gradient, also contributes to the molar flux. Lastly, molar flux is a function of the product of fluid velocity and ion concentration, representing number of moles passing through a unit area oriented perpendicular to the velocity (Newman, 1991: 9).

Transport in dilute species is dictated by the following four principle equations (Equations 2-7 to 2-10), providing the basis for analysis of electrochemical systems (Newman, 1991: 335).

The material balance is based on the differential conservation law and is given by Equation 2-9.

$$\frac{\partial C_i}{\partial t} = -\nabla \cdot \vec{N}_i + r_i \qquad \text{2-9}$$

It is furthermore approximated (quite accurately) that the solution is electrically neutral, expressed by Equation 2-10.

$$\sum_i z_i C_i = 0 \qquad \text{2-10}$$

Current density in the electrolyte solution due to the motion of charged species is dictated by Equation 2-11.

$$\vec{i} = F \sum_i \vec{N}_i \qquad \text{2-11}$$

The Navier-Stokes and continuity equations are used to model fluid velocity (Newman, 1991: 336).

Electrode kinetics is dictated by Equations 2-12 and 2-13 below. The reaction at the electrode surface is given by Equation 2-12.

The molar flux of the reactive ions is the normal component of current density (Newman, 1991: 336).

$$R_i = -\frac{s_i}{nF} i_n \qquad 2\text{-}12$$

Current density distribution is expressed using the Butler-Volmer equation, Equation 2-13 (Newman, 1991: 337). It relates current density to the exchange current density, surface overpotential and kinetic parameters dependent on concentration:

$$i_n = i_0 \left[\exp\left(\frac{\alpha_A F}{R_g T} \eta_s \right) - \exp\left(\frac{\alpha_C F}{R_g T} \eta_s \right) \right] \qquad 2\text{-}13$$

In Equation 2-13 i_n, η_s are positive for anodic processes and negative for cathodic processes. Equation 2-13 is related to concentration *via* Equation 2-14 (Newman, 1991: 194).

$$i_0 = nFk_C^{1-\beta} k_A^{\beta} \prod_i C_i^{(qi+(1-\alpha_i)s_i)} \qquad 2\text{-}14$$

Equation 2-14 serves to incorporate the effect s of the diffusive layer that forms outside the double layer that exists next to the electrode.

2.4.8 Product Gasses

As mentioned before, hydrogen and fluorine gas are produced in the reactor. Oxygen, nitrogen and tetrafluoromethane (a poisonous compound) may be additional contaminants in the product streams (Crouse, 2010, Speciality Gasses of America, 2009, a).

Nitrogen and oxygen contamination can be due to air ingress while oxygen can be produced inside the reactor due to the electrolysis of contaminant water. The burning of carbon anodes results in the production of carbon tetrafluoride. The hydrogen fluoride impurity in the fluorine stream is caused by the high hydrogen fluoride partial pressure of the electrolyte even at low temperatures (Rudge, 1971: 39).

2.4.8.1 Hydrogen and Fluorine

Fluorine, positioned at the top right of the periodic table is the most reactive element. This makes it prone to oxidise most material it comes into contact with, including plastics, reducing agents and organic material. Gaseous fluorine can react with water to form hydrofluoric acid. Due to abovementioned reasons fluorine gas is very toxic and may be fatal if inhaled. It can cause severe burns to the eyes, skin and respiratory system (Speciality Gasses of America, 2009, b).

Hydrogen is highly flammable and poses an explosive hazard. Hydrogen can easily ignite in air, if the hydrogen concentration surpasses 5.7 % (Speciality Gasses of America, 2009, c).

It was found that 95 % of the hydrogen bubbles produced do not spread more than 2 cm from the cathode surface. Fluorine bubbles tend to be large and lenticular and tend to stick to the anode surface. Considering these two facts a fluorine cell does not require a diaphragm, as a skirt is sufficient to keep to gases from recombining explosively (Rudge, 1971: 35-39).

2.4.8.2 Hydrogen Fluoride

Hydrogen fluoride is an extremely dangerous substance and a possible mutagen. It is incompatible with and corrosive to strong bases, metals, glass, leather, water, alkalis, concrete, silica, sulphides, cyanides, carbonates. It is therefore also very toxic and could cause death if inhaled or ingested. Furthermore it is readily absorbed through the skin. Therefore even skin contact may be fatal. Hydrogen fluoride acts as a systemic poison and causes severe burns; contact requires immediate medical attention as effects may only occur at a later time (Speciality Gasses of America, 2009, d).

High temperatures at the anode due to bad heat conduction, caused by lack of circulation, can lead to high hydrogen fluoride concentrations in the fluorine gas stream. This is caused by an increase in the partial pressure of hydrogen fluoride at these elevated temperatures (Rudge, 1971: 35-44).

The problem can be overcome by increasing heat transfer by either cooling the cathode from within or adding nickel to the electrolyte which will enhance bubble detachment, increasing turbulence and effectively increase heat transfer. The fluorine stream will typically contain between 5 and 20 % hydrogen fluoride, which must be removed before sale (Rudge, 1971: 35-44).

The most obvious, but very costly and inefficient, way of removing this impurity is by refrigeration. It has been shown that at refrigeration temperatures as low as -80°C about 2 % of the hydrogen fluoride still remains, indicating that higher temperatures will be even more ineffective. This fact coupled with the difficulties of compression makes refrigeration an undesired method of hydrogen fluoride removal (Rudge, 1971: 35-44).

Absorption of hydrogen fluoride is the next logical step. If sufficient contact can be ensured, sodium fluoride at room temperature could provide the required recovery of hydrogen fluoride from the fluorine stream. Another proposed method involves the contact of the contaminated fluorine stream with the electrolyte or a mixture of potassium acid fluoride and hydrogen fluoride, stripping the fluorine of hydrogen fluoride. One more possibility found to be potentially viable is contacting the fluorine stream with fluorosulphonic acid. This easily regenerative method has been shown to reduce the hydrogen fluoride content of a fluorine stream containing 15 % of the contaminant to as little as 0.3 % at 20 °C. Economic factors tend to limit the use of the last two proposed solutions, as they have not yet been proven to be reliable. If they were, they would most probably only be so in large installations (Rudge, 1971: 35-44).

2.5 Published Fluorine Cell Simulations

A study was conducted on two recently published simulations of fluorine electrolysers. The conditions in these cells were replicated using COMSOL Multiphysics. The resulting simulations were compared to published results; the comparison can be seen in the results and discussion section (section 4) of this dissertation.

2.5.1 Modelling coupled transfers in an industrial fluorine electrolyser (Roustan et al., 1997)

The writers of this publication used Flux-Expert® (FE) based on the Galerkin finite element code to model the momentum-, charge- and heat transfer. A two dimensional cross-section of an industrial electrolyser is modelled. The complexity of the behaviour of the cell is modelled by making use of coupled variables from the various transfer phenomena.

The publication seeks to describe the very specific characteristics of the fluorine cell that are difficult to obtain due to the harsh environment inside the cell as described previously. The model takes advantage of the symmetrical characteristic of the reactor being modelled and only considers half the reactor for computing efficiency reasons. A cross-section of the reactor is shown in Figure 2-5.

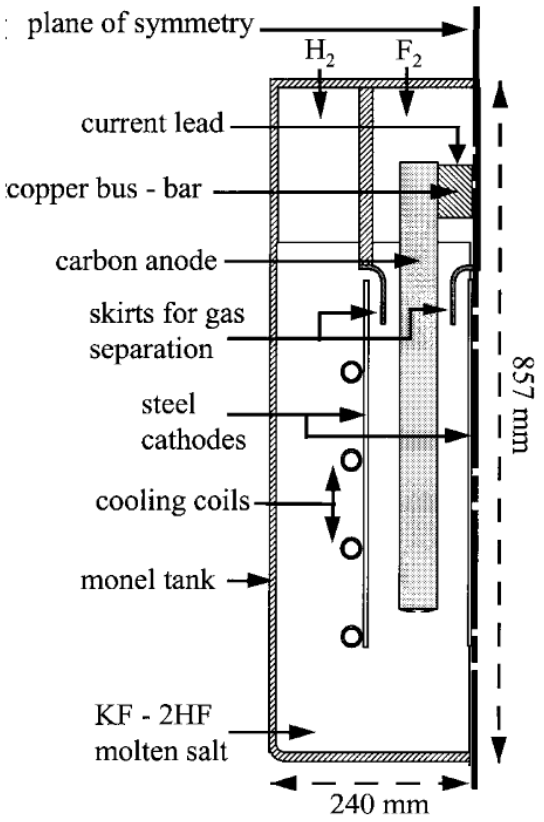

Figure 2-5: Cross section of the industrial electrolyser modelled by Roustan et al. (1997).

The charge transfer was calculated and results were obtained. The potential drop as determined by simulation is shown in Figure 2-6. It was found however (not unexpectedly) that these results did not conform to reality.

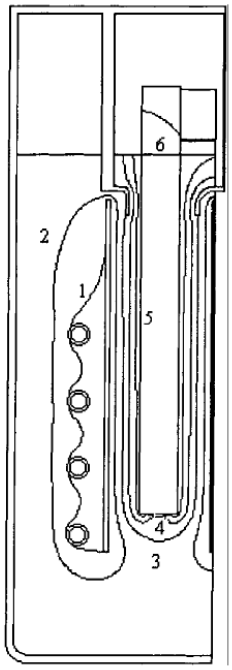

Figure 2-6: Simulated equipotential curves. Key: (1) 0.0 V; (2) 0.4 V; (3) 0.8 V; (5) 1.2 V; (6) 2.0 V (Roustan et al., 1997).

The writers of this article concluded that the model needs to account for the large potential drop observed in fluorine electrolysers by introducing an artificial boundary layer (illustrated in Figure 2-7, a). This boundary layer is a very thin resistive layer of unknown electrical conductivity. The conductivity of this layer is a function of the thickness of the boundary layer and the current density. The current density is in turn determined using the Butler-Volmer equation (Equation 2-8) or experimental data. New equipotential curves were obtained and are shown in Figure 2-6, b.

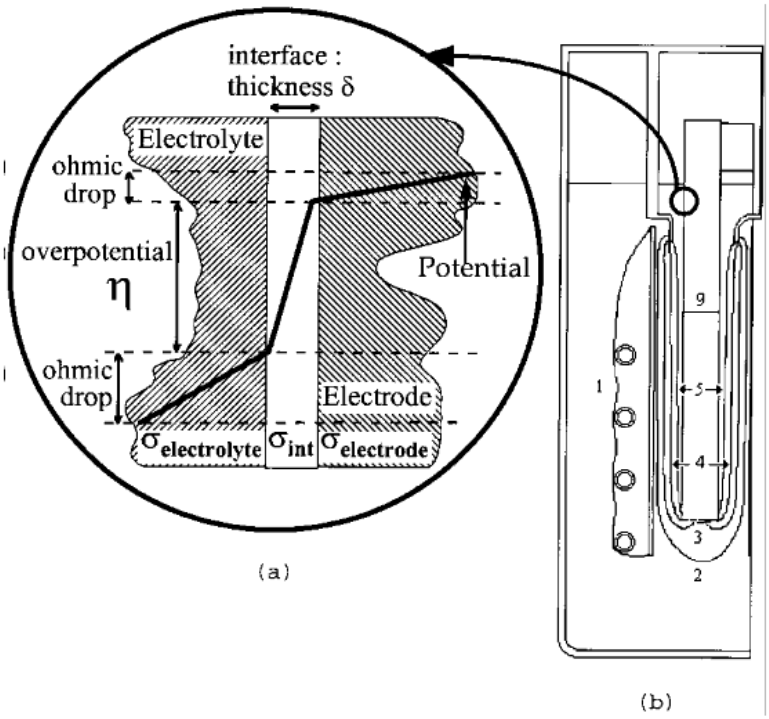

Figure 2-7: Diagrammatic representation of the thin boundary layer (a) used to account for the large overpotential and new equipotential curve (b). Key: (1) 0.0 V; (2) 0.5 V; (3) 1.0 V; (4) 1.5 V; … (9) 9.5 V (Roustan et al., 1997).

Experimental measurements done with small copper wires showed a 95% agreement between simulacrum and reality.

The next step was simulating heat transfer using the charge transfer data acquired, as the main source of heat in the cell is Ohmic losses. The model takes into account heat loss *via* radiation and convection through the external surfaces of the reactor. The model also takes into account cooling of the electrolyte due to the cooling coils and heat flow due to gas flow out of the reactor. The simulation produced isothermal curves that can be seen in Figure 2-8. It was however found that these values did not correspond to experimental results, so a higher value of thermal conductivity ($20\ W \cdot m^{-1} \cdot K^{-1}$) was used and produced the second set of results in Figure 2-9.

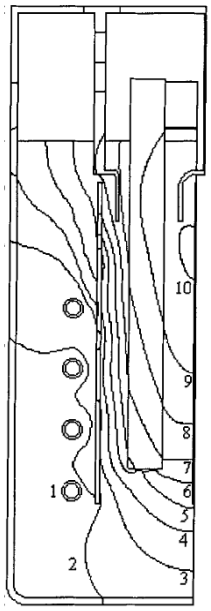

Figure 2-8: Temperature profiles computed with the experimentally determined value of thermal conductivity. Key: (1) 325 *K*; (2) 340 *K*; (3) 355 *K*; (4) 370 *K*; (5) 385 *K*; (6) 400 *K*; (7) 415 *K*; (8) 430 *K*; (9) 445 *K*; (10) 457 *K* (Roustan et al., 1997).

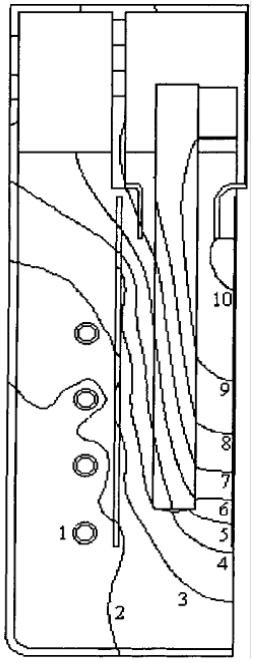

Figure 2-9: Temperature profiles computed with the higher value of thermal conductivity. Key: (1) 325 *K*; (2) 331 *K*; (3) 337 *K*; (4) 343 *K*; (5) 349 *K*; (6) 355 *K*; (7) 361 *K*; (8) 367 *K*; (9) 373 *K*; (10) 379 *K* (Roustan et al., 1997).

The last step of this simulation was the addition the Navier-Stokes equations for non-compressible single phase Newtonian fluids to take into account the hydrodynamics of the reactor. It was assumed that the bubble effects can be neglected. The new temperature curve that takes into account the hydrodynamics of the reactor is shown in Figure 2-10. This simulation still uses the higher value of thermal conduction to obtain a reasonable temperature distribution. A final vector plot of velocity was also produced and can be seen in Figure 2-11. The figure is limited by its use of low resolution arrows which have lost useful interpretability in reproduction. It does however show swirling of electrolyte under the anode as well as a maximum calculated fluid velocity of $0.45\ m \cdot s^{-1}$, neither of which were able to be confirmed by experimentation.

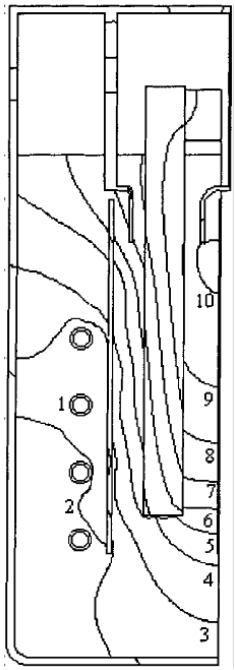

Figure 2-10: Temperature profiles computed with the higher value of thermal conductivity and the influence of hydrodynamics. Key: (1) 325 *K*; (2) 332 *K*; (3) 339 *K*; (4) 346 *K*; (5) 353 *K*; (6) 360 *K*; (7) 367 *K*; (8) 374 *K*; (9) 381 *K*; (10) 388 *K* (Roustan et al., 1997).

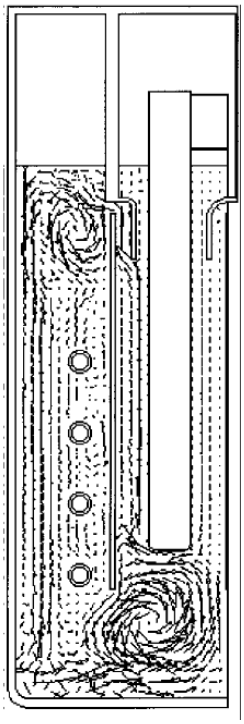

Figure 2-11: Velocity vector plot of the simulation produced by Roustan et al., 1997.

2.5.2 Modeling of the Trajectories of the Hydrogen Bubbles in a Fluorine Production Cell (Hur et al., 2003)

Hur and co-workers conducted a study of temperature and fluid velocity fields in a fluorine production cell. The study was conducted by modelling the momentum and heat transfer processes of a fluorine electrolyser. The reactor setup that was modelled is shown in Figure 2-12. Only a fourth of the cell was modelled due to the symmetric nature of the cell. This saved on computational time without compromising quality of results. The computational domain used is outlined by the dotted lines in Figure 2-12.

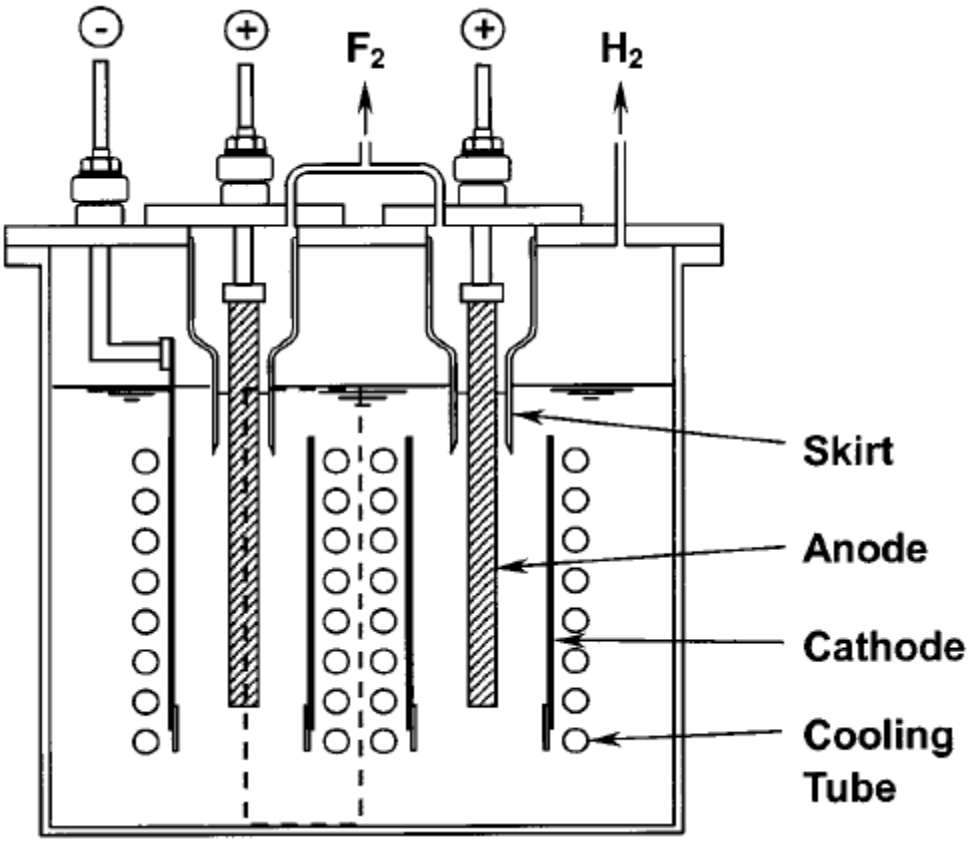

Figure 2-12: Cross section of the fluorine electrolyser modelled by (*Hur et al., 2003*).

Equations that govern the conservation of momentum, mass and energy were applied along with a set of equations that govern the behaviour of the hydrogen bubbles. Temperature and fluid velocity field were modelled using the penalty function formulation and the finite element method. These results were then used as an input into the solution of the number concentration of the bubbles based on the Streamline Upwind/Petrov Galerkin finite element method. The trajectories of the hydrogen bubbles alone were modelled as fluorine bubbles do not contribute significantly to the hydrodynamic behaviour of the electrolyte.

Results of the simulation include the steady-state fluid velocity field and temperature field with streamlines of the cell with a plain sheet cathode are shown in Figure 2-13. It should be noted that only the velocity of the hydrogen

bubbles were considered, as the fluorine bubble tend to stick to the anode and move up slowly along the electrode, propelled by buoyancy forces.

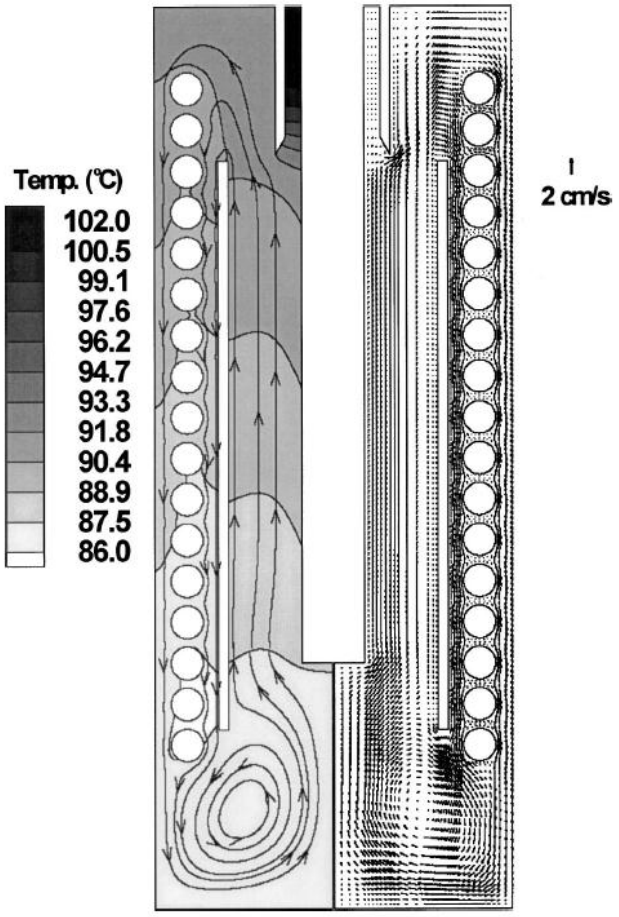

Figure 2-13: Temperature and velocity field as simulated by the Hur group.

The electrolyte is heated between the anode and the cathode and rises up until the electrolyte gets cooled by the cooling tubes at the back of the cathode and it starts flowing downward. A recirculation eddy forms at the bottom of the reactor. This electrolyte behaviour and temperature distribution is similar to results found by Roustan *et al.* (1997).

Bubbles diameter plays a major role in the hydrogen bubble behaviour as evidenced in Figure 2-14, this figure shows the trajectories of three different bubble sizes that evolve at the cathode. , Movement of larger bubbles is

dominated by buoyancy forces and drag force as bubble size decreases. Trajectory I shows movement for bubbles of 0.5mm in diameter, not significantly affected by electrolyte flow. The flow of bubbles with a diameter of 0.37mm is shown by trajectory II, now more affected by electrolyte flow. Drag force completely dominates as bubble diameter is decreased to 0.2mm as indicated by trajectory III. The bubble cannot escape through the surface of the electrolyte, but it circulates within the cell, following the flow of the electrolyte. If it is trapped in the recirculating eddy formed near the bottom of the cell.

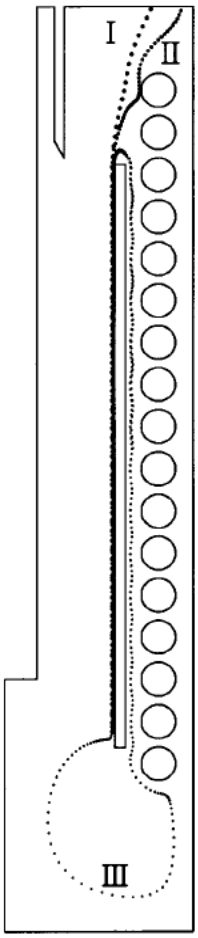

Figure 2-14: Bubble trajectories for hydrogen bubbles of various sizes; 0.5mm (I), 0.37mm (II) and 0.2mm (III) by *Hur et al. (2003)*..

2.5.3 Effect of hydrodynamics on Faradaic current efficiency in a fluorine electrolyser (Espinasse et al., 2006)

The writers of this article conducted a two dimensional simulation of a fluorine electrolyser using two software packages called Flux-Expert® (FE) and Estet-Astrid (EA). The mesh was obtained from the Simail code. FE was used to model the charge and heat transfer phenomena inside the reactor. The data obtained from these simulations was then used as input into the second simulation which used EA to calculate the two phase (H_2 and $KF \cdot 2HF$) momentum transfer simulation. This partial coupling is justified in the text by the fact that previous experiments by the authors found the current distribution and temperature fields to be almost homogeneous in this reactor setup. It was therefore assumed that there is very little contribution by these phenomena to the hydrodynamics of the reactor.

The simulation looks at hydrogen gas formation along the cathode of a pilot reactor and the effects this will have on the hydrodynamics of the reactors. The separator skirt attempts to confine hydrogen to the cathode compartment of the reactor, but electrolyte swirls tend to transport hydrogen bubbles to the fluorine compartment. The percentage of formed hydrogen gas that flows into the fluorine compartment of the cell is then related to the Faradaic current efficiency of the reactor. Hydrogen incursion leads to hydrogen and fluorine recombination in the fluorine compartment and results in a reduction in current efficiency. It should be mentioned that fluorine bubbles were not included in this publication, but the effects thereof were included by making the anode boundary a moving boundary. This simplification is justified by the fact that fluorine bubbles stick to the anode as they move upward and the fact that hydrogen bubble movement causes most of the stirring and hydrodynamic effects in the reactor. This simulation also makes use of a quasi-steady state; it is assumed that the flow in the reactor reaches equilibrium when the hydrogen gas plume is fully developed.

The reactor used in their simulation can be seen in Figure 2-15. The simulation only uses the right side of the reactor along the symmetry axis. This simulation uses a set of partial differential equations to account for the momentum transfer and bubble formation. A modified Navier-Stokes that takes into account the volume gas fraction similar to Equations 3-1, 3-2 and 3-3 was used to calculate mass transfer. Bubble behaviour was modelled using a set of equation that take into account all the forces that interact with the hydrogen bubbles as they rise, like gravity, buoyancy and electrolyte flow.

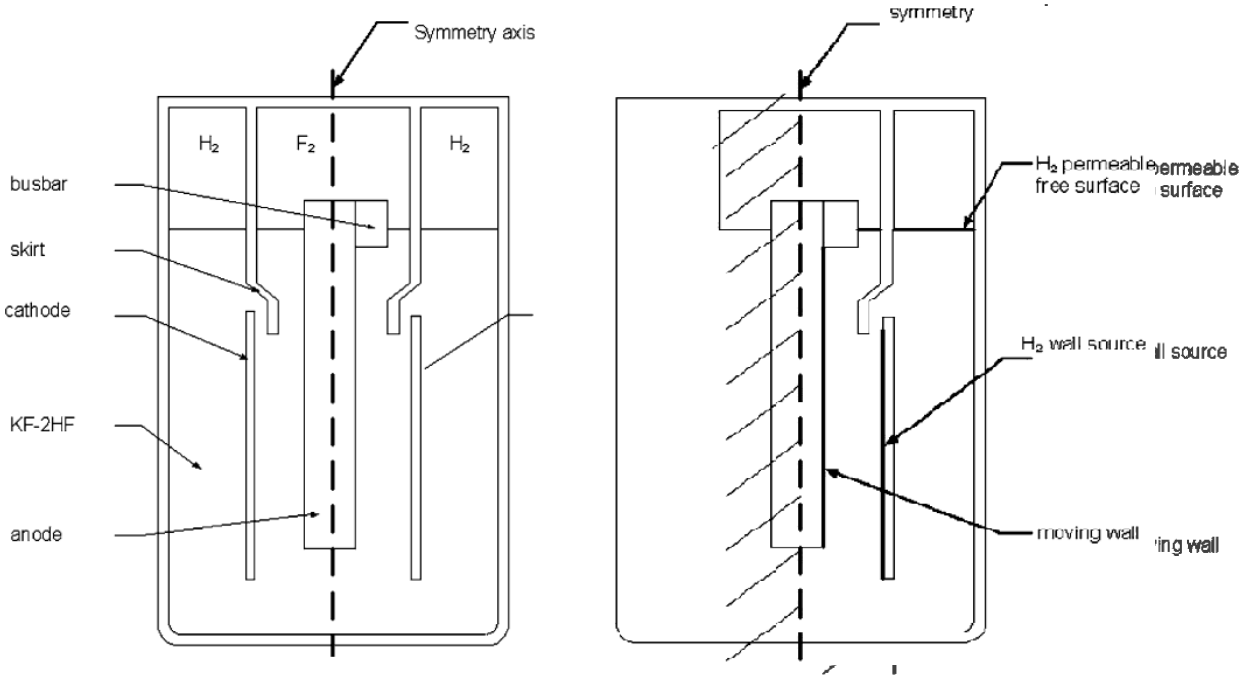

Figure 2-15: Cross-section of the reactor used by Espinasse et al., 2006.

The simulation assumes a uniform current distribution, due to the large gap between the electrodes. This in turn means that the hydrogen production is also assumed to be constant all along the cathode. The flow rate was calculated using a mean cell current, the formula was not specified, but it was stated that the flow rate is related to the current density. The simulation further assumes a single bubble size of hydrogen gas produced, which in turn forms the hydrogen plume. The resulting numerical calculation of gas distribution in the cell is shown in Figure 2-16.

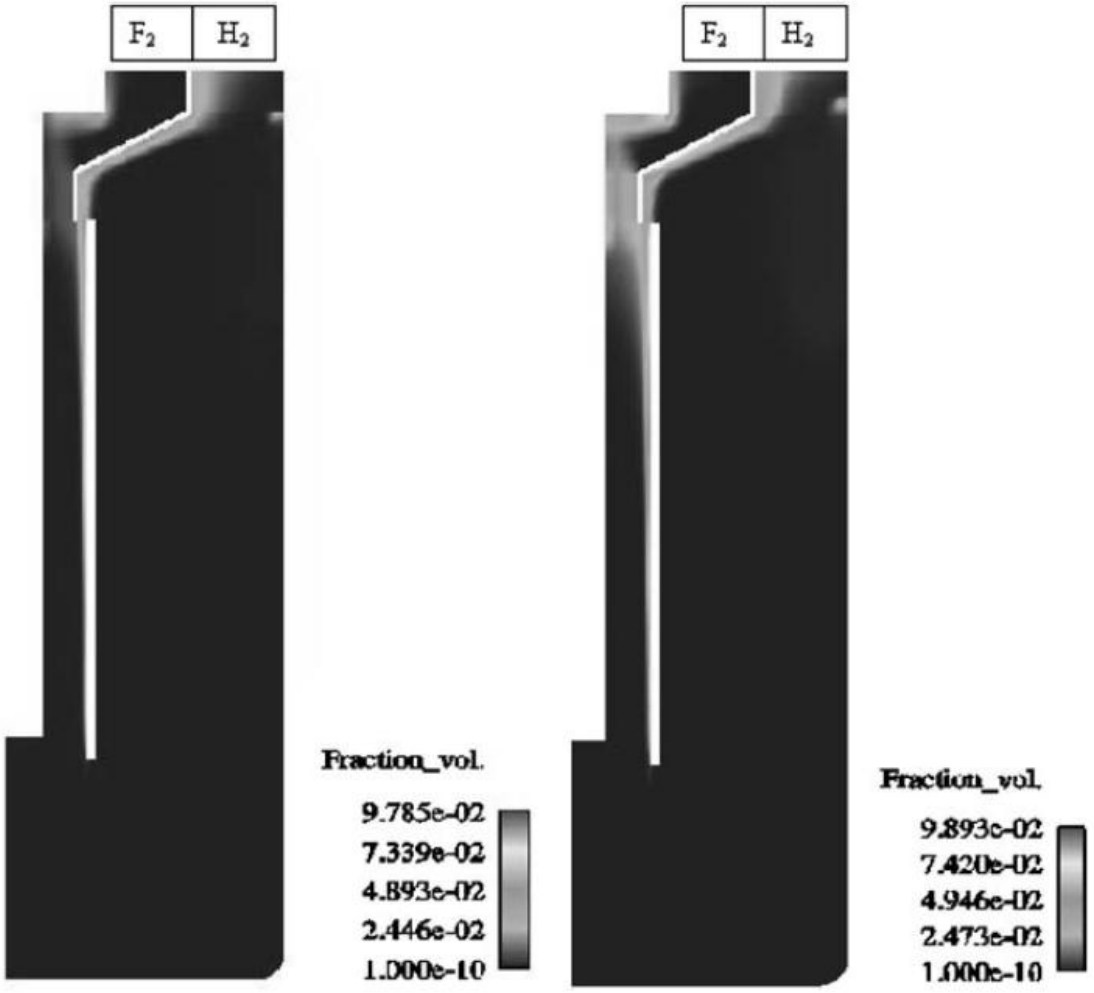

Figure 2-16: Hydrogen mean gas distribution for two different current densities, low on the left and high on the right (Espinasse *et al.,* 2006).

Figure 2-16 shows a well-developed hydrogen plume in both cases, with a higher gas fraction in the case of a higher current density. In both cases it is clear that there is hydrogen ingress into the fluorine compartment. It is clear that a higher current density leads to a more hydrogen ingress.

Other results from this publication relate to the effects of bubble size on the hydrodynamics and efficiency of the reactor. It was found that smaller bubbles are more like to be entrained in the fluorine compartment leading to a drop in current efficiency.

2.5.4 Electrochemical Engineering Modelling of the Electrodes Kinetic Properties during Two-Phase Sustainable Electrolysis (Mandin et al., 2009)

Industrial production of fluorine, hydrogen or aluminium by electrolysis creates bubbles at the electrodes. These bubbles play a major roll on the electrochemical and electrical properties of the electrolyte as well as having a stirring effect on the electrolyte. The goal of this publication was to better investigate the properties of bubbles on electrolysis as bubble properties have a major influence on the economics of electrolysis.

Experiments were conducted in an electrolysis reactor described in the publication. Photographic results of bubble formation near an electrode are shown in Figure 2-17.

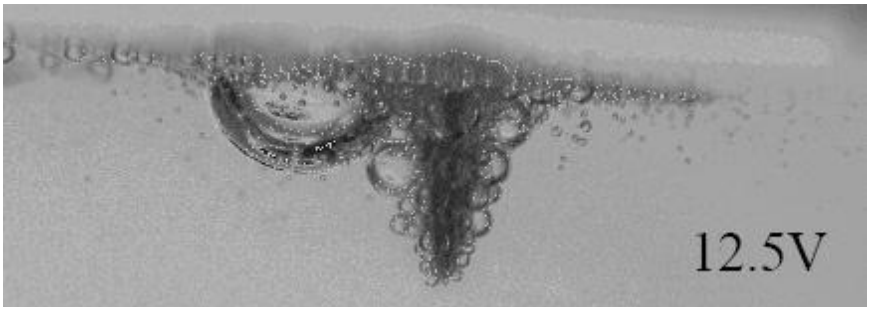

Figure 2-17: Bubble accumulation at 12.5 V around the working electrode during alkaline water electrolysis (Mandin *et al.*, 2009).

From Figure 2-17 we can deduce the shape of a hydrogen bubble plume and approximately estimate gas fraction. The shape of the bubble plume is that of an inverted pyramid formed due to buoyancy forces acting on the bubbles.

2.5.5 Modeling and Simulation of Dispersed Two-Phase Flow Transport Phenomena in Electrochemical Processes (Nierhaus *et al.*, 2009)

Only select chapters from this thesis were studied, particularly the fifth chapter "Coupling of two-phase flow and electrochemistry". The reader is introduced to the basics of electrochemistry, the chapter then progresses to more advanced concepts and fundamental laws that exist in an electrolysis cell. Modelling requirements for a representative electrochemical system are also listed.

Transport equations are discussed next. Equations used for mass conservation, potential field, current density field in the multi-ion transport and reaction model (MITReM) are listed. The MITReM model was used by Nierhaus *et al.* (2009) to model behaviour in an electrochemical cell. Boundary conditions for the electrodes, Insulators, inlets and outlets used in the MITReM is also listed. A lot of overlap exists in the equations used by Nierhaus *et al.* (2009) and the author of this thesis. The use of an integrated Butler-Volmer equation that does not require the calculation of an exchange current density, but still incorporates reactive species concentration was of particular interest.

The discussion continues to consider gas evolving electrodes and the effect they have on electrolyte motion, ion concentration and potential drop between the electrodes. Bubble effect on conductivity and diffusion coefficients and correlations to calculate these parameters are discussed in some detail. Bubble formation and detachment is discussed as well as the forces that influence bubble motion and the effect bubbles have on the electrolyte is discussed at length.

In the next section focus shifts towards the modelling procedure. The software packages used are explained, their various functions and how they are integrated into one multi-physics solver package. These packages calculate the Navier-Stokes, ion-flux, charge and current density distribution, bubble formation and

bubble trajectory data. The solution method and interconnectivity of all these modules and boundary conditions are also explained.

A parallel plate gas evolving reactor is modelled in the next section of the thesis. The reactor is shown in Figure 2-17. In this cell a range of ions exist in solution; Na^+, SO^{2-}, $NaSO^-$, HSO^-, OH^- and H^+, all in H_2O. Hydrogen forms at the cathode and oxygen at the anode. The anode (top) is located downstream of the cathode (bottom).

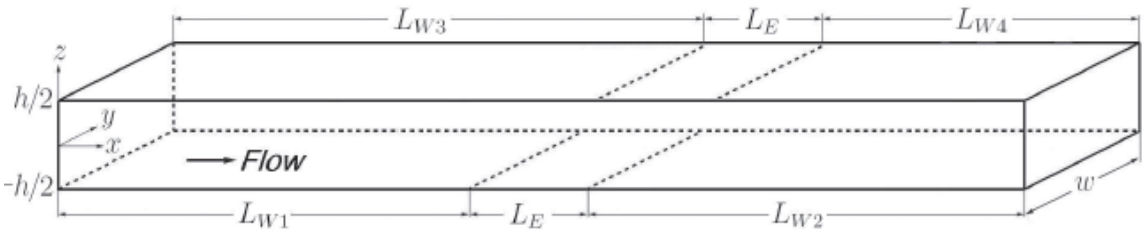

Figure 2-18: Parallel flow reactor as simulated by Nierhaus *et al.* (2009).

Gas production was calculated at incremental potential differences after 2 s. Results are shown in Figure 2-19. A clear impression of bubble rise and dispersion is obtained from the images. Bubble rise due to buoyancy is influenced by drag force induced by electrolyte movement. Larger bubbles seem to rise faster than smaller bubbles, as expected.

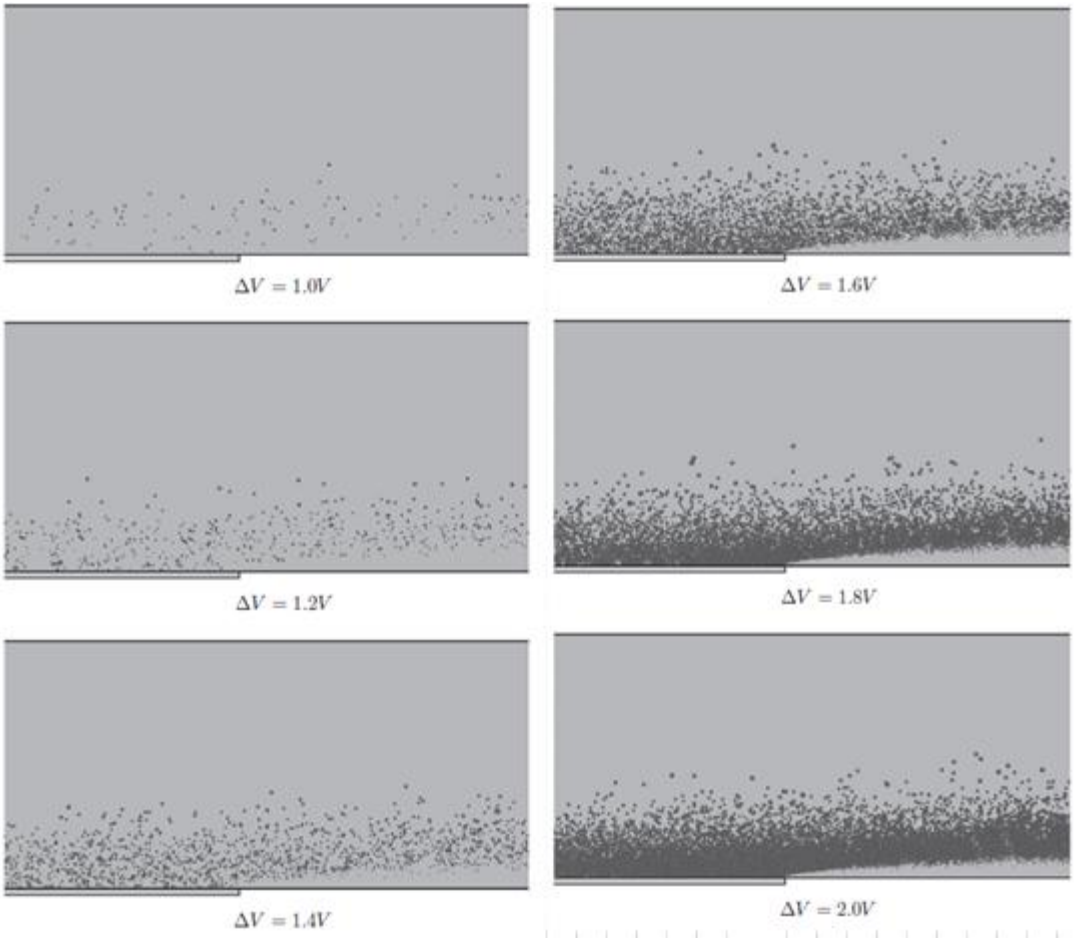

Figure 2-19: Gas production in a parallel flow reactor after 2 s as simulated by the Nierhaus group.

2.6 Summary Conclusion

As an introduction to this thesis a survey was done on a range of industrially relevant electrolysis reactors. In these reactors non-spontaneous chemical reactions are completed with the application of a direct current to two electrodes placed inside a conductive electrolyte medium. Gas evolution, metal deposition and other industrially relevant reactors were discussed. Electrolysis enabled modern society to attain a range of materials that was impossible or extremely expensive to produce in the past.

Focus was then shifted to specifically fluorine electrolysis. The only commercially viable way to produce fluorine is *via* electrolysis of hydrogen fluoride. Due to the low electrical conductivity of the reactant gas the first cells were cooled to -50 °C. Later cells used a molten potassium acid fluoride electrolyte and become known a high temperature cell. It was found that the melting temperature of the electrolyte can be decreased by controlling the amount of hydrogen fluoride in solution and as a result the medium temperature cell was born and is still in use today.

Fluorine progressed from a laboratory curiosity to industrial scale production with the discovery of nuclear fission where it is used in the uranium enrichment process. Fluorine compounds were also used during the Second World War as an incendiary agent. Today it can be found in a range of fluorine compounds ranging from refrigerants, polymer compounds, the electronics industry to specialty chemicals.

As mentioned before, fluorine is produced from the electrolysis of hydrogen fluoride in a potassium acid fluoride electrolyte. Hydrogen is produced as a side product. The hydrogen fluoride is produced from fluorspar reacted in sulphuric acid. Following electrolysis the gaseous products must be purified to remove any entrained hydrogen fluoride.

The electrolysis process is discussed in much detail. Detail is given on the electrolyte, its manufacture and physical properties. The carbon anode and anode phenomena is discussed, specifically polarisation and overvoltage phenomena. The cathode, separator skirt and cell body are discussed next. Electrochemical concepts such as reversible and working voltage are discussed in the subsection that follows. Next heat production specifically is discussed within the cell followed by a subsection on other fundamental transport and modelling equations. The section describing a fluorine cell is concluded with a discussion on the gasses produced during electrolysis.

The literature review of this report is concluded with a study of published fluorine electrolysers. Valuable knowledge was gained from these works, knowledge used to aid in the set-up of the model presented later in this contribution. Due to the incompletion of the experimental reactor the model could not be compared to experimental results. The modelling approach was consequently evaluated by comparing published fluorine electrolysis simulations to simulations done by the author on COMSOL Multiphysics®.

Two papers were chosen for this the first by Roustan *et al.* (1997) where the charge, heat and momentum transfer in a lab-scale fluorine electrolyser was modelled and compared to experimental results. The second was a publication by Espinasse *et al.* (2006) where two phase bubbly flow was modelled in a fluorine electrolyser. Two phase flow results were compared to results found in this paper. Other works included a paper published by Hur *et al.* (2003) where bubble flow inside a fluorine electrolyser was modelled. Knowledge gained here served as a warning of the danger of small bubbles becoming entrained in the electrolyte flow which could lead to explosive recombination of product gases. The contribution by Mandin *et al.* (2009) was studied to get a rough idea of the shape of a hydrogen bubble in an electrolyte. The bubble shown is that of hydrogen in an aqueous medium and does not give an accurate portrayal of a hydrogen bubble in a potassium acid fluoride electrolyte. Lastly parts of the thesis of Nierhaus *et al.* (2009) were studied to gain more knowledge on the workings of two phase simulations of electrolysers.

The knowledge gained from the lliterature review was used in later parts of this thesis to aid in the design of the simulation and interpret results gained from the simulation. Looking at published works it was clear that a fully coupled model is absent from literature. The review further revealed ways in which the model presented in this report could be improved upon.

3 Model Development

3.1 Reactor Description

A cross-section of the electrolysis reactor is shown in Figure 3-1. The reactor construction material is mild steel. The anode is non-porous carbon and the cathodes are mild steel. Gasses produced during electrolysis are separated by a mild steel separator skirt. The skirt (which has been electrically isolated) is submerged by 1.5 cm into the electrolyte; this ensures that a very small area of the skirt is available to produce hydrogen if bipolarisation does occur.

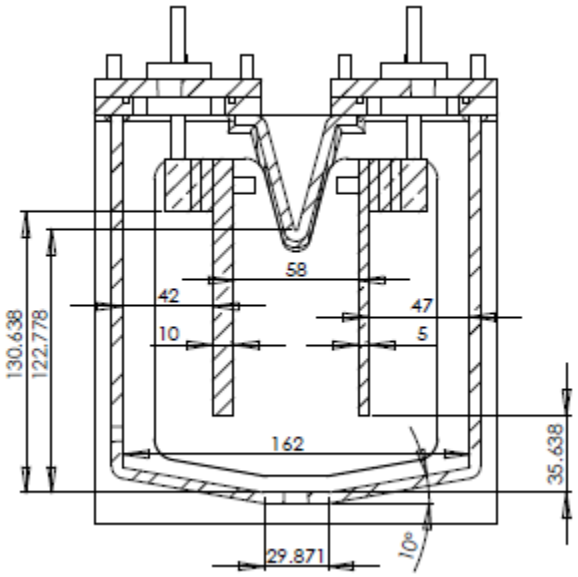

Figure 3-1: Cross-section of the electrolysis reactor.

3.2 Model Description

The model is based on a laboratory scale experimental F_2-electrolysis reactor built at the University of Pretoria constructed to better understand the inner workings of the industrial scale F_2-electrolysis reactors at NECSA. Industrial reactors decompose $KF \cdot 2HF$ on a continuous basis, re-supplying HF to the reactor as HF is decomposed by electrolysis into H_2 and F_2. The laboratory-

scale reactor works as a semi-batch reactor *i.e.* there is no re-supply of HF as it is consumed in the electrolysis reaction.

Modelling was conducted using the software package COMSOL Multiphysics. For the sake of reproducibility the modelling procedure will be explained in a stepwise fashion corresponding to the method employed during modelling with the software package.

The cross sectional-area of the reactor that was modelled is shown in Figure 3-2.

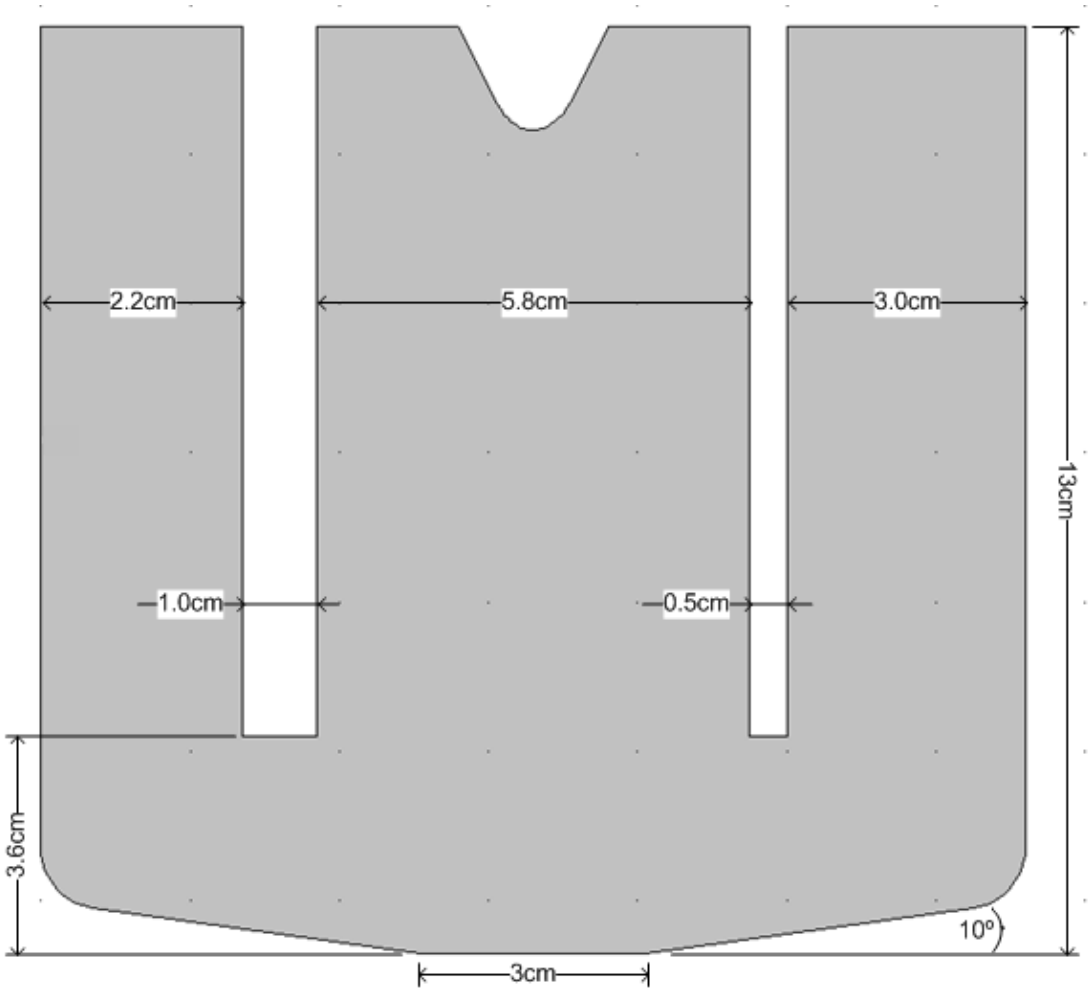

Figure 3-2: Model dimensions.

The COMSOL model only includes the reactor contents up to the electrolyte level and uses the electrolyte properties as specified in Table 3-7. The electrodes were also modelled; the anode material was modelled as carbon and the cathode as mild steel (properties indicated in Table 3-7).

The following physical and chemical transfer solutions were selected and reconciled with the information provided in the literature review.

3.2.1 Momentum Transfer

Flow induced inside the reactor is modelled by Equation 3-1, Equation 3-2 and Equation 3-3; the momentum transport, continuity and laminar bubbly flow equations respectively. These equations are found in the "Laminar Bubbly Flow" physics node of the software suite used.

$$\phi_l \rho_l \frac{\partial \vec{u}_l}{\partial t} + \phi_l \rho_l \cdot \nabla \vec{u}_l = -\nabla P + \nabla \cdot \left[\phi_l (\eta_l + \eta_T) \left(\nabla \vec{u}_l + \nabla \vec{u}_l^{\,T} - \frac{2}{3} (\nabla \cdot \vec{u}_l) \vec{I} \right) \right] + \phi_l \rho_l g + \vec{F} \qquad 3\text{-}1$$

$$\nabla \cdot \vec{u}_l = 0 \qquad 3\text{-}2$$

$$\frac{\partial \rho_g \phi_g}{\partial t} + \nabla \left(\phi_g \rho_g \vec{u}_g \right) = 0 \qquad 3\text{-}3$$

Subscripts "l" and "g" denotes the gas and liquid phases.

Using these equations modelling of mixtures and gasses can easily be achieved by solving for the averaged volume fraction occupied by each of the two phases, rather than tracking each bubble in detail. This procedure assumes two different velocity fields, one for each phase. The following assumptions are adhered to (COMSOL Multiphysics (a), 2010, Espinasse *et al., 2006,* Loth *et al.,* 2006):

- The gas density is negligible compared to the liquid density.
- The motion of the gas bubbles relative to the liquid is determined by a balance between viscous drag and pressure forces.
- The two phases share the same pressure field.
- Gas volume fraction is less than 0.1.

Flow is induced in the reactor due to the following interactions:

- Ionic migration due to concentration gradients.
- Ionic migrations due to electric field interactions.
- Convection due to gas bubble formation at the electrodes.
- Convection caused by temperature gradients due to heating.

Laminar bubbly flow (Reynolds number<0.1) was assumed for the hydrogen bubbles and the assumption was later justified by calculation. Additionally it was assumed that the bubbles are small and perfectly spherical. Therefore Stokes law was applied to calculate the terminal velocity of hydrogen gas bubbles (Talalia, 2007). An estimated bubble size of 1 mm was used during calculations (Espinasse *et al*., 2006). It should be noted that fluorine bubbles are long lenticular bubble that do not detach from the anode and therefore Stokes law will not give valid terminal velocity results.

The largest bubble terminal velocity (H_2 at $3.63\times10^{-4}\ m\cdot s^{-1}$) had a Reynolds number of 2.421×10^{-4}, a value less than 0.1 (justifying the earlier assumption) and validating the use of laminar bubbly flow for bubble movement.

The reader should take note that the physical properties of only one gas (hydrogen) was used to model both product gasses in the simulation, this is due to lack of data concerning both gasses in the reactor and an inability of the modelling software to model two gasses in a two-phase problem. To overcome this shortcoming both gasses were modelled as Hydrogen. Seeing as the two

gasses have massive differences in physical, particularly bubble properties and behaviour, some modifications had to be made to the gas produced at the anode.

The flow rate of fluorine was adjusted with a constant factor (0.1). This ensures that the upward moving effect of the fluorine bubbles on the anode is included in the simulation, but that the fluorine bubble retains its key properties (slow moving lenticular bubbles that stick to the anode and slowly move to the electrolyte surface. These bubbles do not break away from the electrode surface and are propelled by buoyancy forces. These qualities are adequately retained as can be seen in the results section (Hur *et al*, 2003, Rudge, 1971). In other works by Roustan *et al.* (1997), Hur et al. (2003) and Espinasse *et al.* (2006), the effect of the fluorine bubbles were either completely neglected or compensated for as a moving boundary.

3.2.2 Heat Transfer

Heat transfer due to convection and conduction inside the reactor is modelled using in Equation 3-4 below, found in the "Heat Transfer" physics module of the software package (COMSOL Multiphysics (b), 2010, Çengel, 2006:74-76,). Heat generation due to viscous heating was ignored. The walls of the reactor where temperature was specified will be the only heat sink during the modelling procedure. The remaining reactor walls will additionally remove heat *via* radiation to ambient atmosphere and the electrolyte level will remove heat *via* convection.

$$\rho C_p \frac{\partial T}{\partial t} + \nabla \cdot (-k\nabla T) = Q - \rho C_p \vec{u} \nabla T \qquad 3\text{-}4$$

The internal source of heat in Equation 3-4 is heat generation due to resistive losses, or Ohmic heating in the electrolyte seen in Equation 3-5 (Rudge, 1971: 34). This equation is used throughout the entire electrolyte domain during simulation. Heat generated within the electrodes will be predicted using Equation 2-7.

$$Q = \left\{ i \cdot \left(\Phi - \Phi_{RV} \right) + i \cdot \left[2.81 \cdot \frac{\left(100 - E \right)}{100} \right] \right\} \cdot {}^{1}\!/\!_{d_{ie}} \qquad 3\text{-}5$$

3.2.3 Charge Transfer

The chemical reaction (electrolytic decomposition of the electrolyte into F_2 and H_2) is induced by electric potential predicted by Equations 3-6 (Laplace Equation) which predicts the primary current distribution and adheres to the assumption of Equation 3-7. The Laplace Equation is the default equation used in the "Electric Currents" physics node of COMSOL Multipysics.

$$-\nabla \cdot d(\sigma \nabla \Phi) = 0 \qquad 3\text{-}6$$

$$\nabla \Phi^2 = 0 \qquad 3\text{-}7$$

The physics model used in COMSOL assumes that the electric field only varies in two dimensions (*xy*-plane) and is constant in the z-direction. By implication this means the electric filed is tangential to the *xy*-plane (COMSOL Multiphysics (c), 2010, Roustan *et al.,* 1997).

3.2.4 Mass Transfer

Mass transfer inside the reactor is modelled using Equation 3-8 (Newman, 1991: 194, Welty *et al., 2001,* COMSOL Multiphysics (d), 2010).

$$\frac{\partial C_i}{\partial t} + \nabla \cdot (-D_i \nabla C_i - z_i \mu_{m,i} F C_i \nabla \Phi + C_i \vec{u}) = r_i \qquad 3\text{-}8$$

The "Transport of Diluted Species" physics node in the software suite was used because the reactive solvent concentration is approximately 60 % (molar) of the

solution and the solute will not be re-supplied during experimentation, further diluting the reacting species. The three species assumed to be in solution are given in Table 3-1. The electrolyte dissociation reaction is given by Equation 3-9 (Crouse, 2010).

$$KF \cdot 2HF \rightarrow K^{+} + HF + HF_2^{-} \qquad 3\text{-}9$$

Table 3-1: Chemical species assumed to be present during electrolytic production of hydrogen and fluorine (Crouse, 2010).

Species	***Charge Number*** (z_i)
K^{+}	+1
HF_2^{-}	-1
HF	0

Dilute species flux at the electrodes was further modified to include the effect of bubbles near the electrode surface. This was achieved by finding the product of the calculated diluted species flux and the calculated liquid fraction at the specific point in the electrolyte.

3.2.4.1 Electrode Reactions

Electrode reactions occurring in the reactor are assumed to be Equations 3-10 and Equation 3-11 (Groult, 2003). Reaction 3-10 occurs at the anode and reaction 3-11 at the cathode.

$$HF_2^{-} \rightarrow HF + \tfrac{1}{2} F_2 + e^{-} \qquad 3\text{-}10$$

$$2HF + e^{-} \rightarrow HF_2^{-} + \tfrac{1}{2} H_2 \qquad 3\text{-}11$$

Equations 2-7, 2-8 & 2-9 are used to predict gaseous production rate of both product gasses. These consumption rate equations are stoichiometrically adjusted to predict production rate of reactant species and product gasses at the electrode surfaces. The reaction rate was calculated with data supplied by Crouse, 2010 (2010). The production rate of fluorine is further adjusted by a fractional value (0.1). Fluorine bubbles tend to stick to the electrode and move up the anode at low speed; therefore a detached bubble model for fluorine would overestimate the stirring effect of fluorine in the cell.

3.2.5 Starting Conditions

The starting conditions in the reactor are given in Table 3-2.

Table 3-2: Starting conditions used in the model.

Transfer Process	***Description***
Momentum Transfer	Velocity equals zero
Heat Transfer	Reactor temperature equals 80 °C
Charge Transfer	Cell Voltage equals 0 V
Mass Transfer	Reactive species concentration equals 1000 $mol \cdot m^{-3}$

3.2.6 Boundary Conditions

Boundary conditions used in the model are given in Table 3-3 (Momentum-Transfer), Table 3-4 (Heat-Transfer), Table 3-5 (Charge-Transfer) and Table 3-6 (Mass-Transfer).

It should be noted that the reactor wall boundary conditions for heat- (radiation) and charge transfer (insulation) are chosen to correspond to the boundary conditions that would be valid on the outside of the reactor. The values were chosen as such due to the low thickness of the wall, combined with its high

thermal and electrical conductivity. This estimation simplifies the model as only one domain material is now in use for the external boundaries.

Table 3-3: Boundary conditions for momentum transport.

Boundary	***Boundary Condition***	***Description***	***Equation***
Electrolyte level	Liquid boundary condition: slip Gaseous boundary condition: gas outlet	Acts as a gas outlet and allows liquid slip.	$\frac{\partial \vec{u}_l}{\partial t} = 0$ $\frac{\partial \vec{u}_g}{\partial t} = \phi_g \cdot \rho_g \cdot \vec{u}_g$
Anode surface	Liquid boundary condition: no slip Gaseous boundary condition: gas flux	Allows gas production according to specified reaction rate (R_A). No liquid flow.	$\vec{u}_l = 0$ $\frac{\partial \vec{u}_g}{\partial t} = n \cdot \rho_g \cdot R_A$
Cathode surface	Liquid boundary condition: no slip Gaseous boundary condition: gas flux	Allows gas production according to specified reaction rate (R_C). No liquid flow	$\vec{u}_l = 0$ $\frac{\partial \vec{u}_g}{\partial t} = n \cdot \rho_g \cdot R_C$
All other boundaries	Liquid boundary condition: no slip Gaseous boundary condition: no gas flux	Allows neither gas or liquid flow, both without slip	$\frac{\partial \vec{u}_i}{\partial t} = 0$

Table 3-4: Boundary conditions used to model heat transfer within the reactor.

Boundary	***Boundary Condition***	***Description***	***Equation***
Walls in contact with heating/cooling jacket	Temperature specified	Wall temperature set to T_w, a constant 80 °C	$T = T_w$
Walls in contact with ambient air	Ambient radiation	Heat flux set to radiate to ambient conditions	$T = T_w$
Top of electrolyte	Convective cooling	Heat flux set to convective cooling	$T = T_w$
All other boundaries	Thermal insulation	No heat flux allowed	$\vec{n} \cdot (-k\nabla T) = 0$

Table 3-5: Boundary conditions used to model charge transfer within the reactor.

Boundary	***Boundary Condition***	***Description***	***Equation***
Anode	Inward current density	Current density i_A as determined by the Butler-Volmer equation	$\vec{n} \cdot i_n = i_A$
Cathode	Inward current density	Current density i_C as determined by the Butler-Volmer equation	$\vec{n} \cdot i_n = i_C$
All other boundaries	Electric insulation	No current flow allowed	$\vec{n} \cdot i_n = 0$

Table 3-6: Boundary conditions used to model mass transfer within the reactor.

Boundary	***Boundary Condition***	***Value/Expression***	***Equation***
Anode	Dual mass flux	Reactive species HF flows into electrode and HF_2^- out of electrode as defined by R_A	$\vec{n}\cdot(-D_i\nabla C_i + C_i\vec{u}) = -n\cdot R_A$
Cathode	Inward current flow	Reactive species HF_2^- flows into electrode and HF out of electrode as defined by R_C	$\vec{n}\cdot(-D_i\nabla C_i + C_i\vec{u}) = 0$
All other boundaries	Mass flow insulation	No mass flow allowed	$\vec{n}\cdot(-D_i\nabla C_i + C_i\vec{u}) = -n\cdot R_C$

3.2.7 Constants

Constants used during modelling are given in Table 3-7.

Table 3-7: Model constants.

Constant	*Description*	*Value*	*Reference*
C_{p_0}	Constant pressure heat capacity at 25 °C	$10.8\ J \cdot \mathrm{kg}^{-1}K^{-1}$	Rudge, 1971
d_b	Average bubble diameter	$1\ mm$	Espinasse *et al., 2006*
D_{HF}	Mass transfer coefficient for HF	$2.8 \times 10^{-5} m^2 \cdot s^{-1}$	Estimated
$D_{HF_2^-}$	Mass transfer coefficient for HF_2^-	$3 \times 10^{-5} m^2 \cdot s^{-1}$	Estimated
E	Current efficiency	$95\ \%$	Rudge, 1971
F	Faraday's constant	$96485\ C \cdot mol^{-1}$	
g	Gravitational acceleration	$9.81\ m \cdot s^{-2}$	
$k_{t,c}$	Thermal conductivity of carbon	$150\ W \cdot m^{-1} \cdot K^{-1}$	Estimated
$k_{t,e}$	Thermal conductivity of electrolyte	$1.25\ W \cdot m^{-1} \cdot K^{-1}$	Estimated
$k_{t,s}$	Thermal conductivity of steel	$44.5\ W \cdot m^{-1} \cdot K^{-1}$	Estimated
k_A	Effective rate constant for HF_2^-	$1\ m \cdot s^{-1}$	Estimated
k_C	Effective rate constant for HF	$1\ m \cdot s^{-1}$	Estimated
P_rtr	Atmospheric pressure inside the electrolysis cell	$86\ kPa$	Crouse, 2010
R_g	Ideal gas constant	$8.314\ J \cdot mol^{-1} \cdot K^{-1}$	
T_0	Starting temperature of electrolyte	$353.15\ K$	Crouse, 2010
T_w	Wall temperature of electrolysis cell in contact with heating jacket	$353.15\ K$	Crouse, 2010
α_A	Anode electron transfer coefficient	0.50	Newman, 1991: 17

α_C	Cathode electron transfer coefficient	$(1-\alpha_A) = 0.50$	Newman, 1991: 17
β	Thermal expansion coefficient of electrolyte	$7.11\times10^{-4}\ {}^{\circ}C^{-1}$	Rudge, 1971
ε_r	Relative permittivity	9	Estimated
Φ	Cell electric potential	$12\ V$	Crouse, 2010
Φ_{RV}	Reversible cell voltage	$2.9\ V$	Rudge, 1971
$\Phi_{0,A}$	Electric potential at anode	$2.9\ V$	Crouse, 2010
$\Phi_{0,C}$	Electric potential at cathode	$0\ V$	Crouse, 2010
η_l	Liquid (electrolyte) viscosity (assumed constant)	$0.0113\ Pa\cdot s$	Espinasse *et al., 2006*
η_g	Gas viscosity (assumed constant)	$0.001\ Pa\cdot s$	Crouse, 2010
σ_c	Electrical conductivity of carbon	$3\times10^{3}\ S\cdot m^{-1}$	Crouse, 2010
σ_e	Electrical conductivity of electrolyte	$6.67\ S\cdot m^{-1}$	Crouse, 2010
σ_s	Electrical conductivity of steel	$4\times10^{6}\ S\cdot m^{-1}$	Crouse, 2010
ρ_g	Gas molar density	$22.41\ kg\cdot mol^{-1}$	
ρ_0	Density of electrolyte at 25 °C	$2000\ kg\cdot m^{-3}$	Crouse, 2010

3.2.8 Expressions

Expressions used during modelling are given in Table 3-8.

Table 3-8: Model expressions

Expression Name	***Description***	***Expression***	***Reference***
C_p	Temperature dependent heat capacity	$C_p = C_{p_0} + 0.00284\cdot T$	Rudge, 1971

Q	Total heat production	$Q = i \cdot (\Phi - 1.9V) + i \cdot \left[2.81 \cdot \frac{(100-95)}{100} \right]$	Rudge, 1971
R_A	HF consumption at anode	$R_A = -\frac{1}{F} i_A$	Crouse, 2010
R_C	HF_2^- consumption at cathode	$R_C = -\frac{2}{F} i_C$	Crouse, 2010
i_0	Exchange current density	$i_0 = F k_c^{0.5} k_a^{0.5} C_{HF_2^-}^{0.5} C_{HF}^{0.5}$	Newman, 1991: 195
i_A	Anode current density	$i_A = i_0 \left[\exp\left(\frac{\alpha_A F}{R_g T} \eta_s \right) - \exp\left(\frac{\alpha_C F}{R_g T} \eta_s \right) \right]$	Newman, 1991: 194
i_C	Cathode current density	$i_C = -i_0 \left[\exp\left(-\frac{\alpha_A F}{R_g T} \eta_s \right) - \exp\left(-\frac{\alpha_C F}{R_g T} \eta_s \right) \right]$	Newman, 1991: 194
ρ	Electrolyte density	$\rho = \rho_0 \cdot \left(\exp\left(\beta \left(T - 25^\circ C \right) \right) \right)^{-1}$	Rudge, 1971: 10
$\eta_{s,A}$	Anode surface overpotential	$\eta_{s,A} = \Phi - \Phi_{0,A}$	Heitz & Kreysa, 1986: 101
$\eta_{s,C}$	Cathode surface overpotential	$\eta_{s,C} = -\Phi - \Phi_{0,C}$	Heitz & Kreysa, 1986: 101

3.2.9 Mathematical Solution

The Finite Element Method (FEM) was used for the calculation of the solution of the mathematical model. The FEM was originally developed to solve problems in civil engineering, but is now used for approximation of mathematical solutions to

Partial Differential Equations (PDEs) in many areas of applied mathematics (Burden *et al.*, 2005: 721).

A big advantage that the FEM has over the Finite Difference Method (FDM) is that irregular boundaries can be handled more easily. FEM makes use of the fundamental result of the calculus of variations which states that the solution of the PDE under consideration is also the functional that minimises a functional, *i.e.* a function of a function (an integral particular to the PDE) within the region of solution. Irregular shaped boundaries and boundary conditions involving derivatives are approached by including boundaries as integrals of the function that is being minimised. This results in the solution construction procedure being independent of the particular boundary conditions of the problem (Burden and Faires, 2005: 721-722).

Triangles, squares or any regular shape are used to divide the region of the PDE into sections or elements. This collection of elements is called “the mesh”. The set of function used to approximate the shape, is commonly a set of linear or bi-linear polynomials of fixed degree in x and y. The polynomial functions must be pieced together so the resulting function is continuous and can be integrated in the first or second derivative over the entire problem region. A typical linear polynomial used with triangular elements is given by Equation 3-11.

$$f(x,y) = a + bx + cy \qquad \text{3-11}$$

The expressions are used to indicate how the value of a variable relates to that variable value at another point (or node) connected by the expression. A sum of these relations weighted by the nodal values is approximated as a solution to the problem. The equations of the weighted sum are then minimized. Rapid changes in variables are more accurately indicated with smaller mesh elements (Burden and Faires, 2005: 722).

3.2.9.1 Solution Method

MUltifrontal Massively Parallel sparse direct Solver (MUMPS) was used as a direct solver, with a memory allocation factor of 1.2. Pivoting was used with a pivoting threshold of 0.1. A constant damping factor of 1 was used. The maximum allowed iterations were set to 5. All solutions were done without the use of inconsistent stabilisation, but rather with consistent stabilisation.

To solve the charge transfer problem (Calculation A) cell potential (Ecell) was used as a changing parameter in a separate stationary parametric sweep calculation step. The value of Ecell was incrementally increased form 3 V to 12 V. This allowed the simulation to use the lower (and easier to solve) value of Ecell as a starting point for the next (higher value).

The final 12 V value of Ecell was then used as a starting value input to a time dependent calculation (Calculation B). In this second calculation the momentum- and heat-transfer phenomena were solved, based on the constant charge transfer values supplied. Momentum and charge-transfer was chosen due to their coupling and large amounts of interaction.

A third calculation (Calculation C) was attempted, where the final results of Calculation B were used as initial input values. In this calculation the mass-transfer in the reactor was calculated, using the values calculated in Calculation B. Mass-transfer was calculated last as it is coupled with all the other transfer modules and presents a significant challenge to the solver.

It is clear that final calculation (Calculation D) was needed to firstly determine time dependent values of all transfer phenomena and to also ensure transient coupling between all transient transfer regimes. In this calculation charge-, mass-momentum and heat-transfer was calculated. It was chosen last as it is the largest and most complex set of equations to solve, where coupling occurs between all transfer modules. In Calculation C stationary values of

charge-transfer and transient values of heat, momentum- and ion-transfer was used to solve for transient values of mass transfer. To achieve calculation D final time-step results of Calculation C was used as an initial value input. Results of Calculation D are presented in the Results and Discussion section. Calculation D includes fully coupled time dependent ion-transfer results.

3.2.9.2 Meshing

Two meshes were used during the solution of this problem. The first (henceforth referred to as Mesh I) was used in Calculations A-C and can be seen in Figure 3-3.

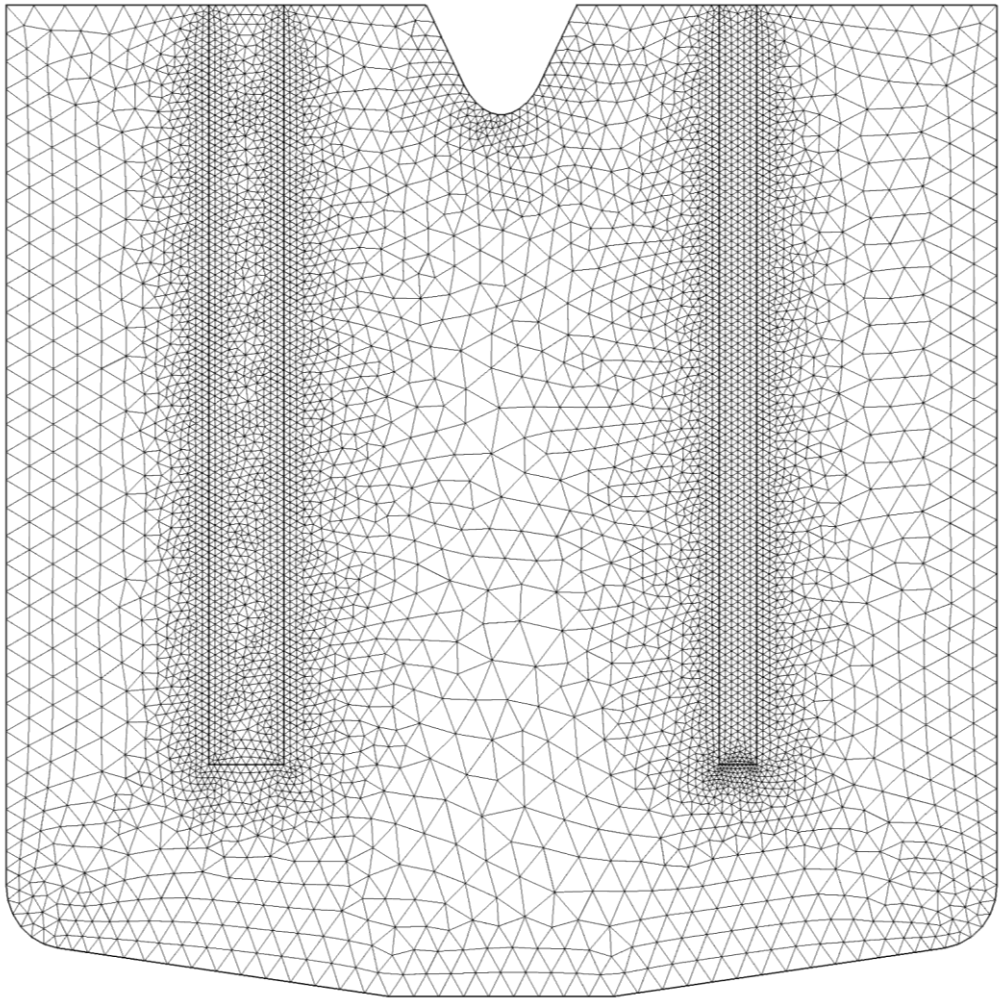

Figure 3-3: Mesh I, used for calculations A-C.

Mesh I has 11398 triangular mesh elements and was set up by the user. Smaller mesh elements were used around perceived complex points in the system. Statistics on Mesh I can be seen in Figure 3-4.

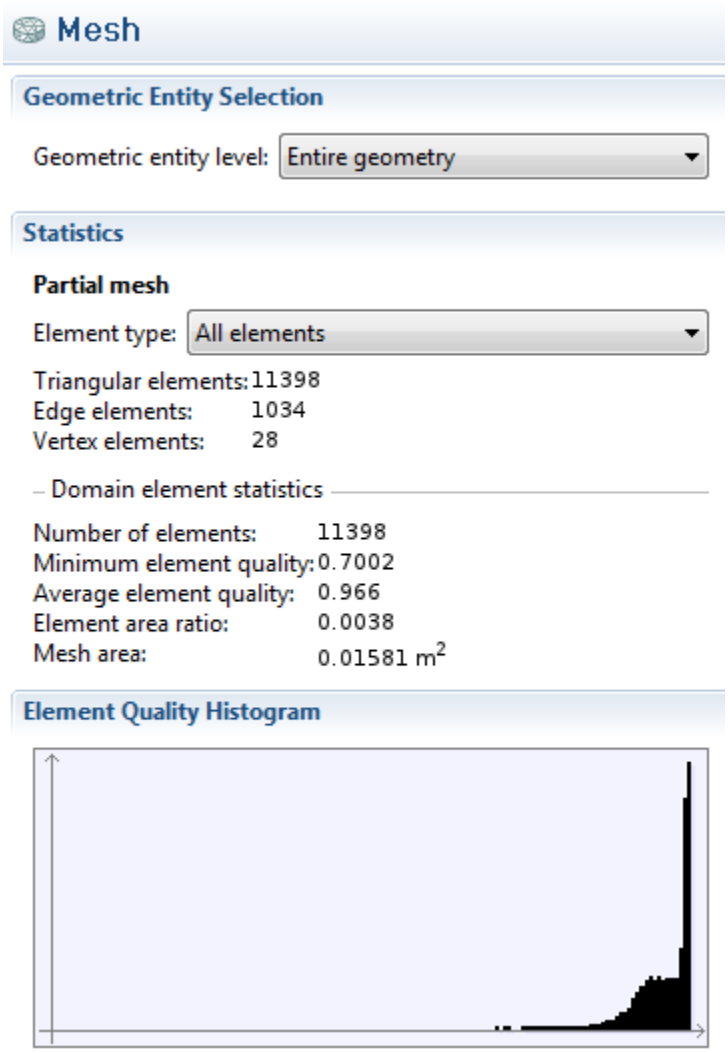

Figure 3-4: Detailed statistical data for Mesh I.

A very fine or “finer” physics controlled mesh in the software suite settings was used for the solution of Calculation D, this resulted in 20621 triangular mesh elements. This mesh will be referred to as Mesh II. The mesh was further refined around the electrodes and separator skirt, where there are very complex interactions occurring between the various transfer processes, specifically the

high current density concentrations. This specific mesh configuration was used to aid in convergence The mesh can be seen in .

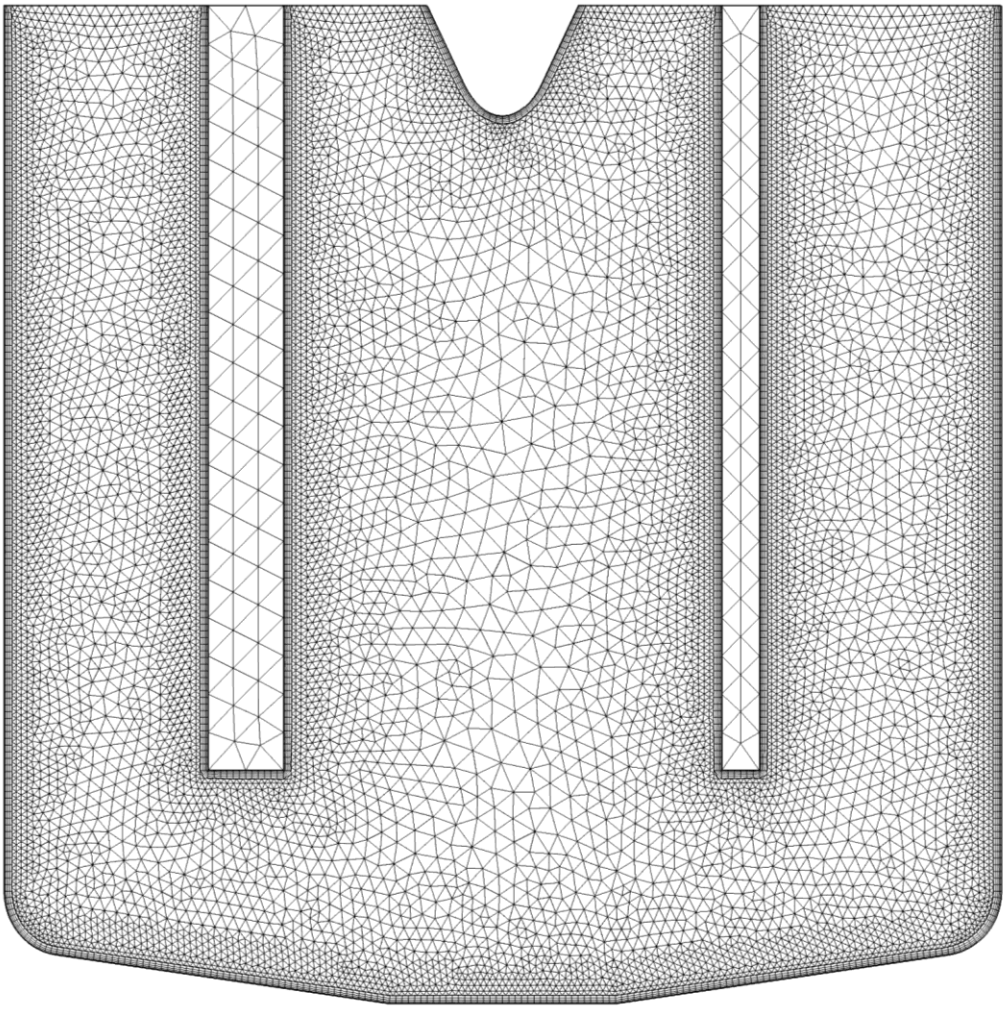

Figure 3-5: Meshing framework of fluorine cell (Mesh II).

Notice the extremely fine mesh around the electrodes; this was used as the finer mesh is more suited to handle complex boundary conditions. It also aids in convergence. Notice the rectangular mesh elements around the electrodes and outer walls. These so-called “Boundary-layer” mesh elements are specifically suited to complex coupled boundary layered conditions and help the model to converge. Further statistics concerning Mesh II is presented in .

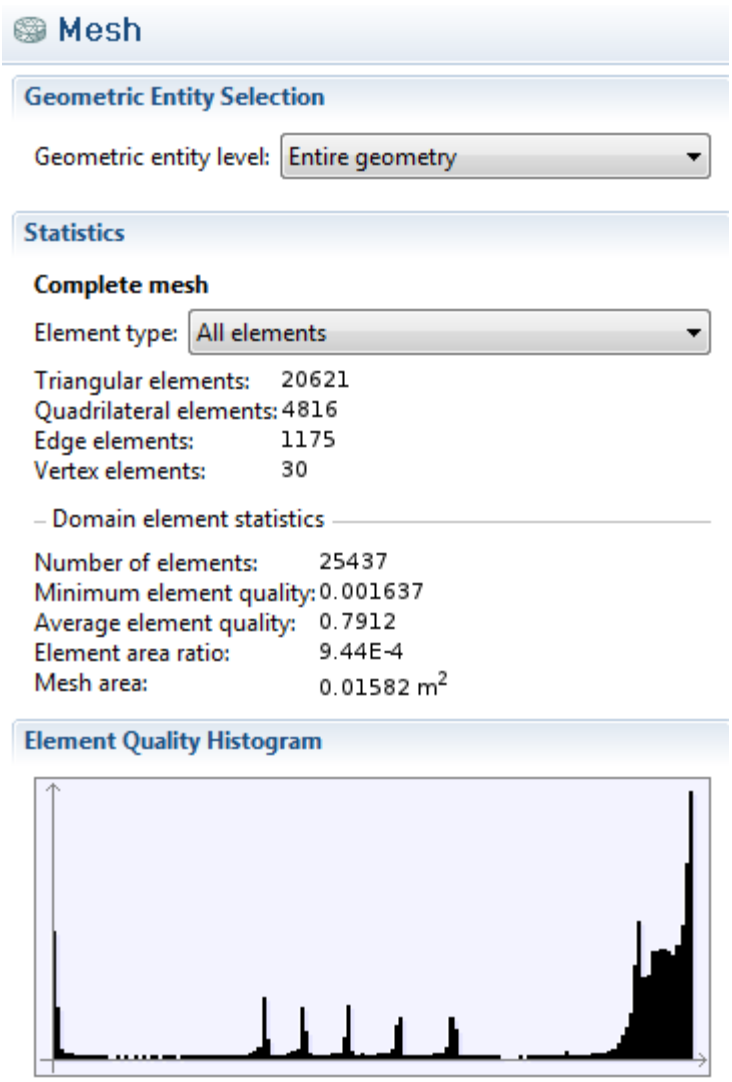

Figure 3-6: Detailed mesh statistics for Mesh II.

3.2.9.2.1 Mesh Dependency

As an additional step to ensure the reliability of the solution, a further study was conducted. In FEM simulations it is possible to obtain a solution to a problem that only solves for a specific mesh. This is called a mesh dependent solution. As a measure to prevent possible mesh dependent solutions or unwanted error propagation two different meshes (Mesh I and Mesh II) were used during calculation. Mesh I was used for calculations A, B and C, while Mesh II was used for Calculation D. Further refinement/convergence test were also done.

Mesh I was refined by an entire order to roughly double the number of mesh elements. Mesh I was chosen as this is the mesh used to ramp up the applied reaction voltage in Calculation A, this is potentially troublesome as it could force the solution to converge from a previous solution. This in could result in a memory effect which could diverge the simulated solution from the real solution. Noise can accumulate and becomes especially troublesome in sensitive areas such as the tips of electrodes. As shown by Caire *et al.* (2002), the current distribution in any electrolyser is very sensitive to mesh quality. Calculation A was repeated, with the smaller sized mesh (over 220000 mesh elements) and results were practically identical. The differences are illustrated in Figure 3-7, using the COMSOL Multiphysics feature that allows data sets to be joined and then compared.

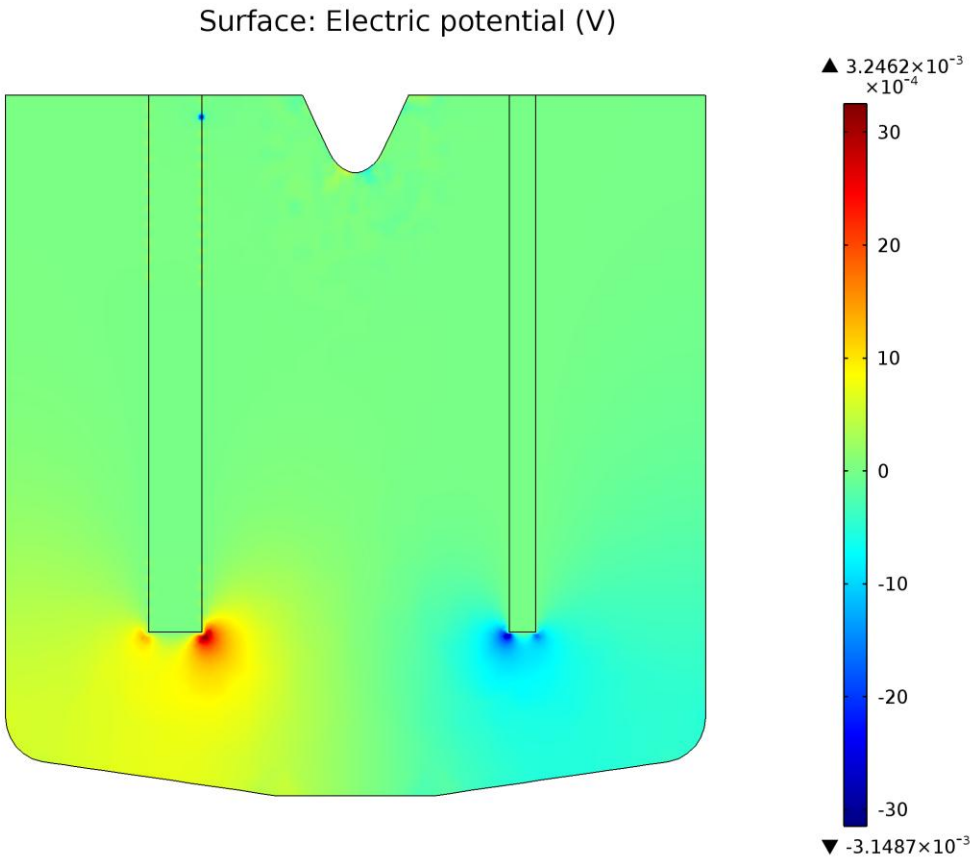

Figure 3-7: Comparative graphic of electric potential for two different meshes.

Figure 3-7, shows the electric potential at a cell voltage of 12 V for the refined mesh of over 220000 mesh elements subtracted from the original mesh (Mesh I) at a cell voltage of 12 V. A refinement in mesh in the direct solver used by the author results in a third power increase in calculation time, therefore due to the lack of a cluster only Calculation A was completed with a finer mesh.

A second study was conducted where the allowed error was decreased from its previous value (1e-5), to a lower value (1e-7) on the original rougher mesh. Calculation A was then repeated and practically identical results were found. It was therefore concluded that the solution is very near to an analytical solution and not “forced”.

Lastly, Calculation D was repeated three times on consecutively finer meshes to check for convergence. This was achieved in all three cases. These results are not shown in this report.

3.2.9.3 Computing

An Intel I7 CPU 870 with 2.93 GHz and 16GB RAM on Windows 7 64bit operating system requires around just over 30 min to compute Calculation D. Calculation A solves in just over 120 s, Calculation B in just over 80 s, Calculation C in 27 s. Calculation D requires Calculation times were significantly improved on the latest version of COMSOL Multiphysics (version 4.2a). As a reference in version 4.2 Calculation D took well over 16 hours. Once Calculation A-C have been completed only Calculation D needs to be run for minor changes in the model setup.

Mesh dependency studies increased the required calculation time due to the increase in the number of mesh elements. Calculation times for Calculation A when on the refined Mesh I took just over 4 hours. While the calculation times for Calculation A where the allowable error was decreased increased calculation

time to just over 150 s. Mesh dependency studies done on Calculation D increased calculation time to exponentially for each incremental decrease in mesh size.

4 Results and Discussion

From Figure 4-1 it is clear that after an initial rapid rise, the average liquid velocity reaches an asymptotic value after a relatively short period. It was therefore be assumed that the hydrodynamic conditions within the reactor will not change much after 100 s as a quasi-steady-state condition was reached. Work by Espinasse *et al.*, assumed that a quasi-steady-state is reached once the hydrogen plume has fully formed. Gaseous movement induces stirring in the electrolyte and remains the major contributor to electrolyte movement throughout reactor operation. Therefore once this flow pattern has been established it can be assumed that flow conditions will not change much as time progresses.

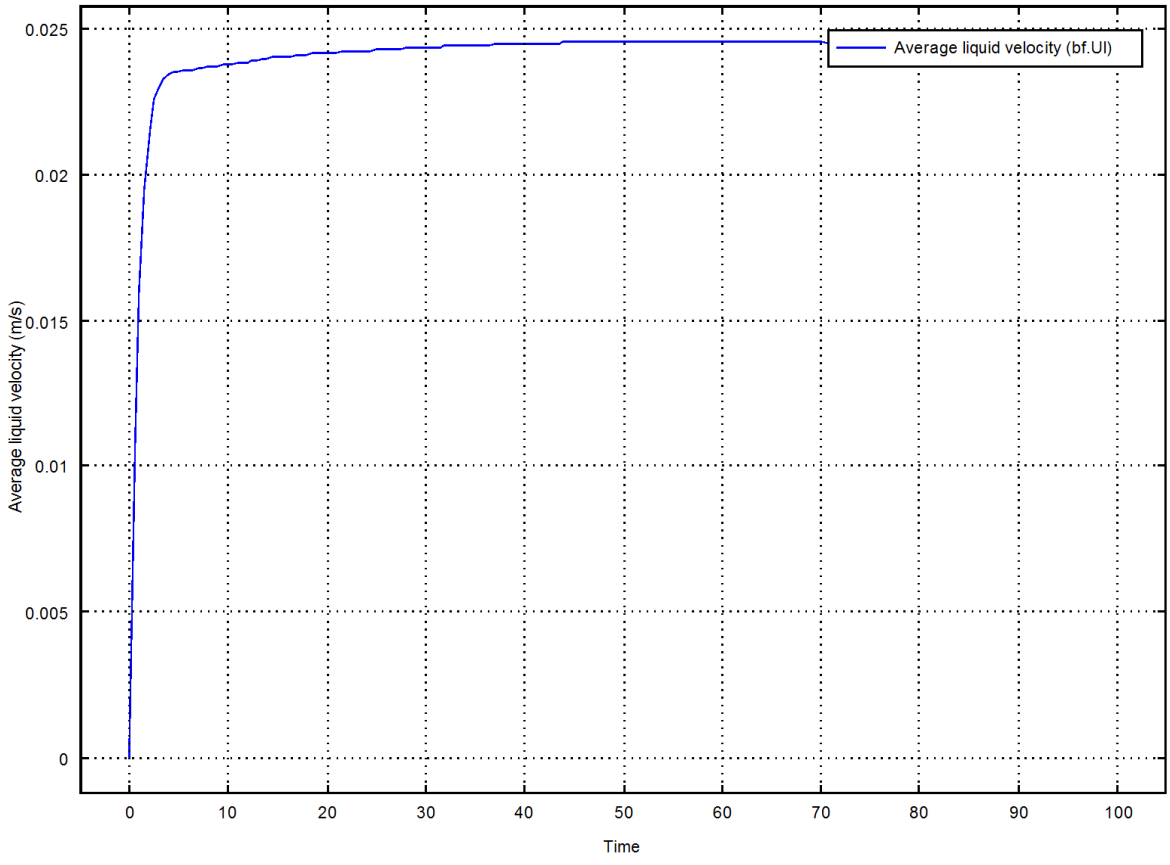

Figure 4-1: Average liquid velocity inside the reactor over time

The value of a transient simulation further lies in knowledge gained in the startup period of a reactor. True steady state is also of importance, but non-existent in a batch reactor. Results will therefore focus on the reactor conditions at 100 s. Transfer phenomena where significant or interesting change did occur will be shown in 11 s intervals.

4.1 Momentum Transfer

The simulation gave the following momentum transfer results. Gaseous movement inside the reactor can be seen in Figure 4-2. The colour scale on the right indicates gaseous velocity in meters per second. Warmer colours indicate higher velocities. The vector arrows indicate the direction of the gaseous flow at the arrow origin. The size of arrows is proportional to the velocity of the gas at the point of origin.

From Figure 4-2 it is clear that gas is produced at both electrodes. The product gasses move away from the electrodes and upwards and out of the reactor. This upward motion contributes to the liquid phase movement inside the reactor. The reader should however note the presence of vector arrows all over the reactor does not necessarily indicate the presence of a gas at that point, but does in fact indicate the path a gaseous element would take if present at that point. The indicated velocity at this point is mainly a function of buoyancy and a bubble placed at that point would move at the indicated velocity in the indicated direction.

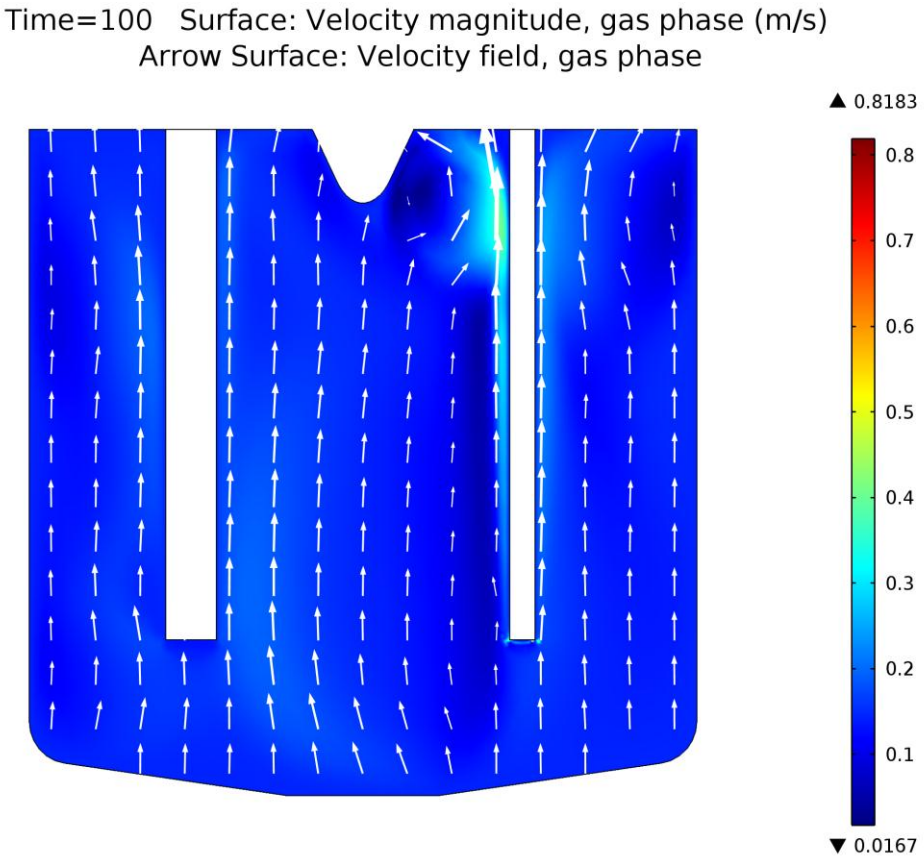

Figure 4-2: Gas phase velocity inside the electrolysis reactor.

Liquid phase movement can be seen in Figure 4-3. The colour scale on the right represents liquid phase velocity inside the reactor, warmer colours represent higher velocities. Arrows indicate direction and is proportional to velocity at the arrow starting point.

The liquid movement induced by gaseous (specifically hydrogen) movement is evidenced by the swirling liquid phase eddy between the separator skirt and the left of the cathode at the top right of the reactor. The downward motion of the liquid eddy in turn influences gas phase movement shown by the reduced gas phase velocity where the liquid moves downward. The downward liquid motion induces stirring in the reactor. This same eddy has the effect of causing stirring throughout the reactor. The downward liquid torrent extends and moves down toward the bottom of the reactor where it starts moving upward once more. This

upward movement is aided by the liquid movement induced by fluorine gas upward motion along the anode. It should be noted that this fluorine flow is in fact hydrogen flow that has been altered to allow the inclusion of the stirring effect fluorine bubbles could have in the reactor. The stirring eddy then turns around once more as it reaches the top of the reactor and joins up with the liquid eddy induced by hydrogen gas movement.

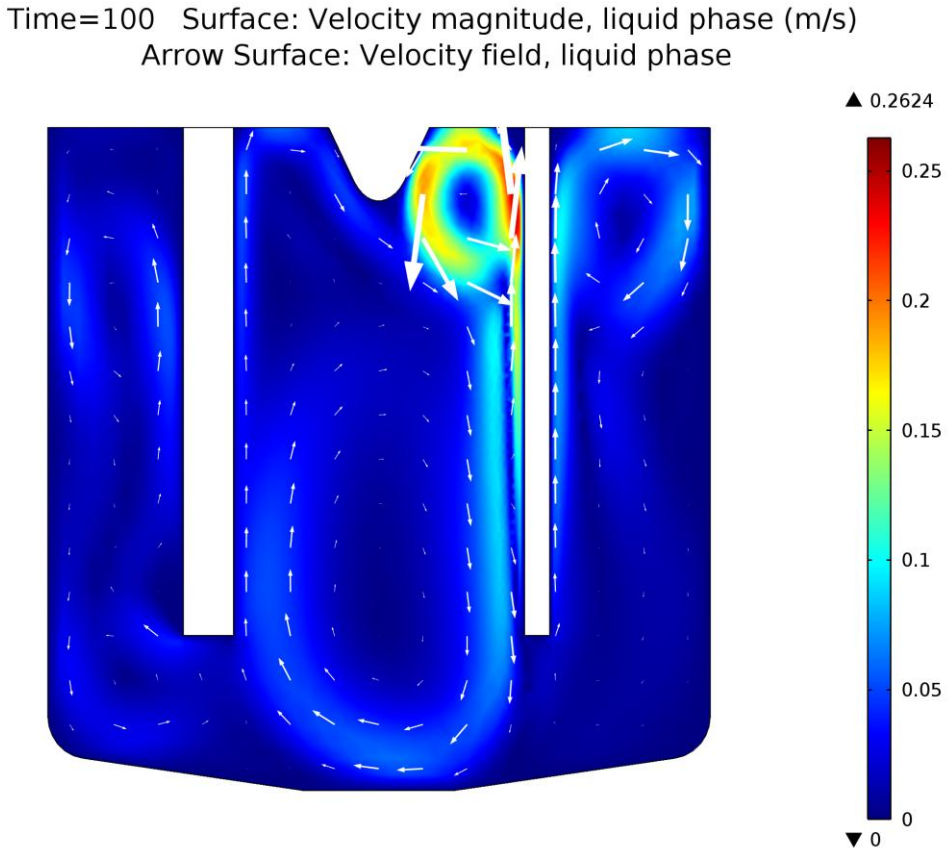

Figure 4-3: Liquid phase velocity inside the reactor.

The relatively low levels of electrolyte movement in the space between the reactor walls and electrodes indicate that the reactor size can possible be reduced, which will in turn reduce costs. Alternatively the distance between the electrodes can be increased to further aid in the prevention of product gas recombination. The fluid flow lines are presented in Figure 4-4.

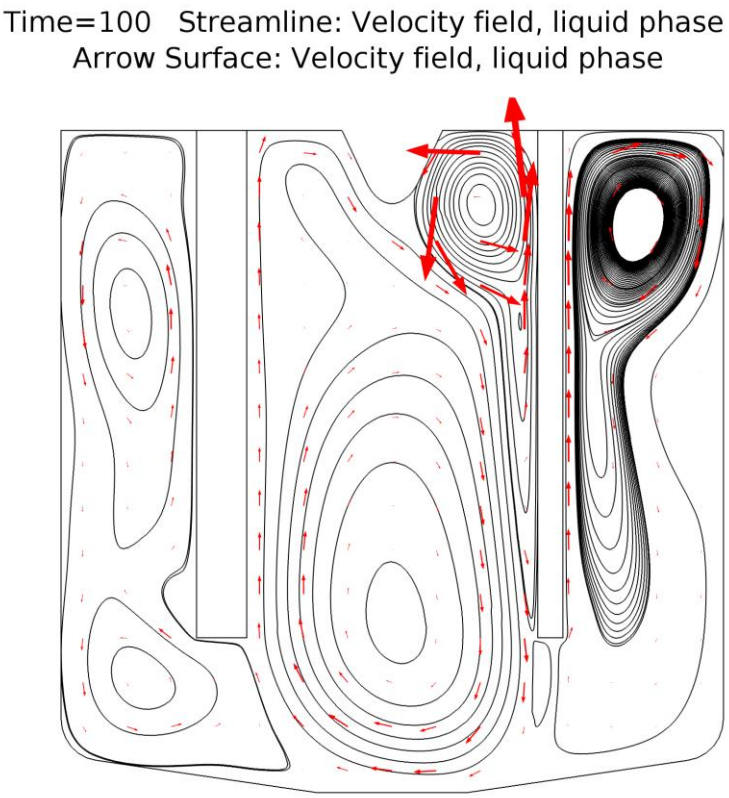

Figure 4-4: Liquid phase velocity streamlines plot and liquid flow arrows inside the simulated reactor.

Figure 4-4 clearly shows the dead volumes and eventual bubble recirculation paths within the reactor. These will be discussed in more detail following the presentation of Figure 4-5. Liquid velocity vector arrows and gas fraction in the reactor are shown in Figure 4-5. Warmer colours indicate higher gas fractions and colder colours indicate a low gas fraction.

Figure 4-5 shows a well-developed hydrogen plume and detachment from the cathode occurs as expected. The fluorine plume on the other hand does not detach from the anode. This is to be expected as fluorine bubbles form long lenticular bubbles that tend to move slowly up along the electrode. Very little hydrogen migration into the fluorine section is observed; therefore the chance of explosive recombination of product gasses is very low. The liquid flow pattern

does suggest that recombination is possible, but the gas velocity profile suggests that the bubble will leave the reactor as soon as it gets to the top. This is also good news from a productivity standpoint, as fewer product gases are lost and less purification of product streams will be required.

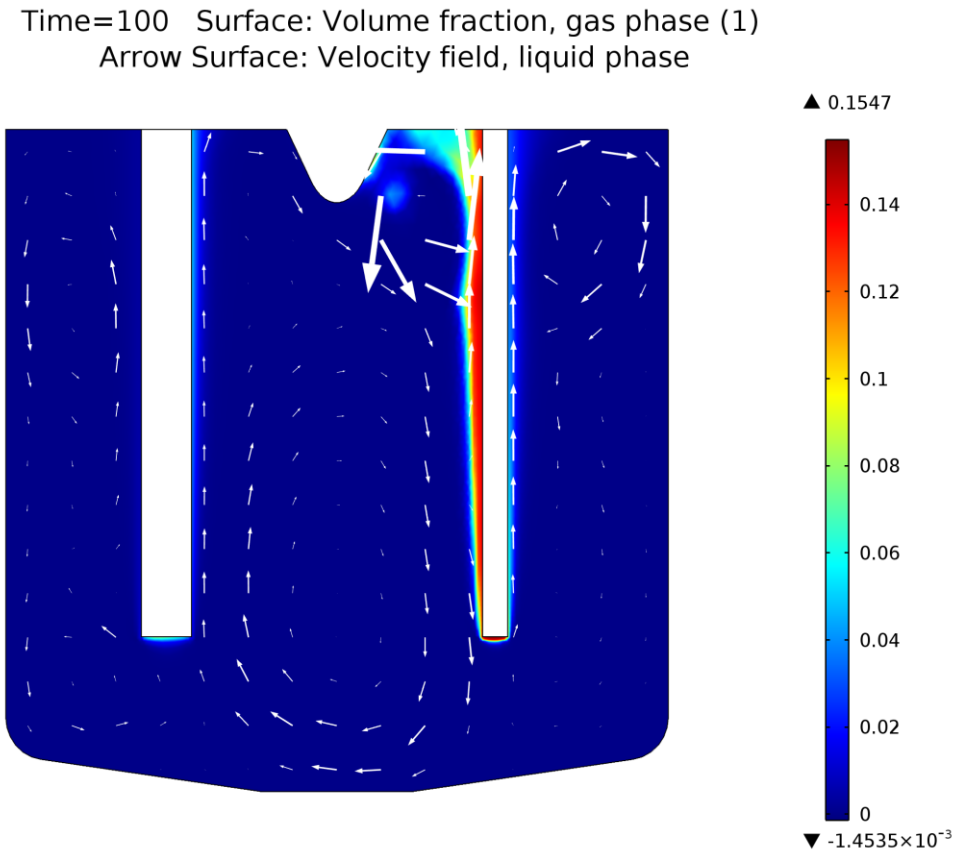

Figure 4-5: Gas phase fraction in the reactor.

It should however be noted that if bubbles become sufficiently small they may be entrained in the liquid velocity flow path. This effect was demonstrated by Hur *et al.* (2003). If this effect does occur it could in fact lead to explosive recombination of product gases. Bubbles in this simulation are all of 1 mm size so buoyancy force should dominate convection in terms of bubble trajectory.

4.1.1 Time Progression

Initially there is little movement in the reactor but as time goes by the convection, due to gaseous flow in the reactor, temperature fluctuations and migration of dissolved species due to electric field migration, results in eddying motion in the reactor. This can be observed in the time progression plots of Figure 4-6, Figure 4-7 and Figure 4-8. From these plots it becomes clear that convection is the major source of movement within the reactor. As mentioned earlier the electrolyte motion in the reactor is induced by gaseous flow. This flow pattern development can be seen in the time progression plots that follow.

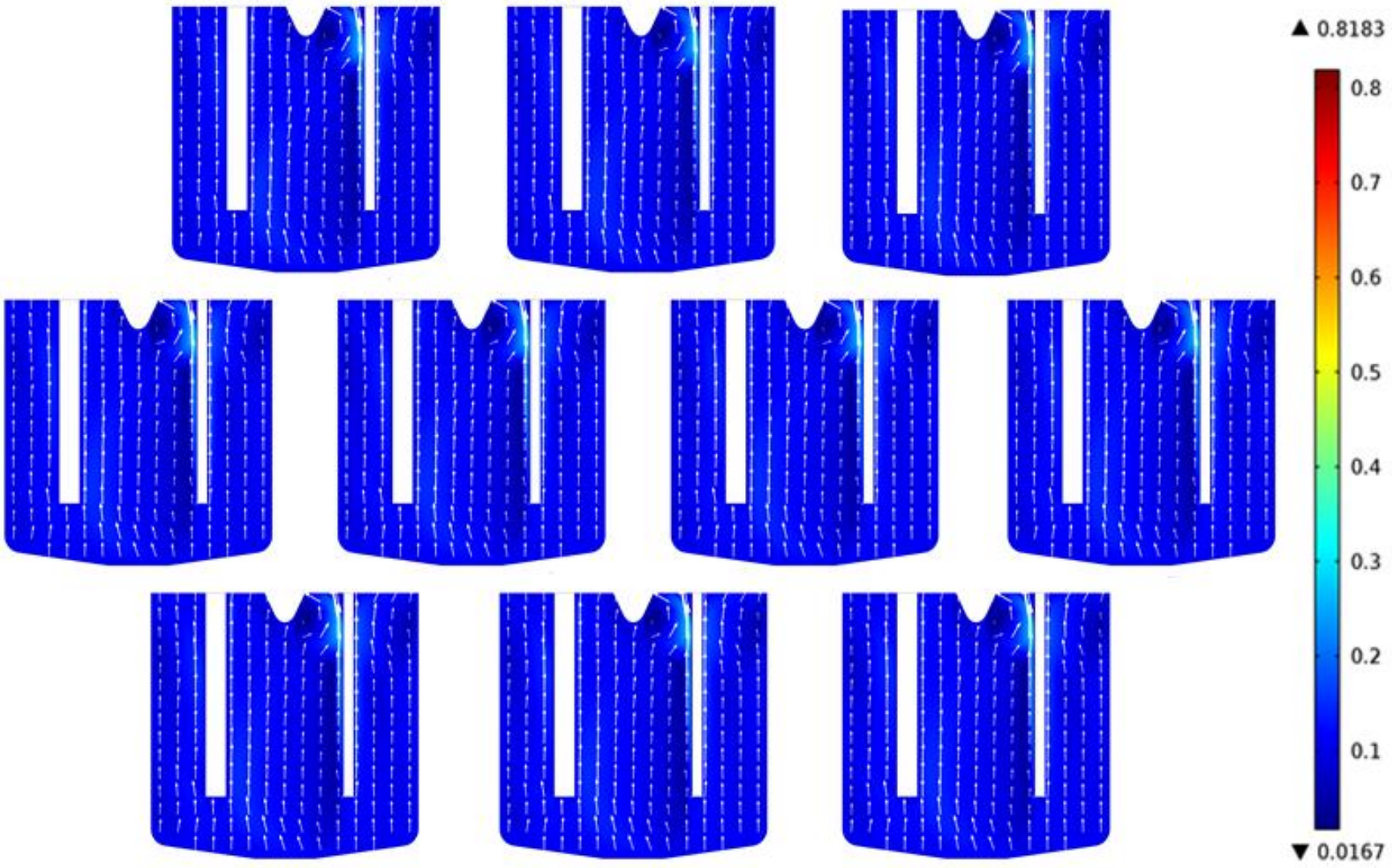

Figure 4-6: Gaseous phase velocity time development sequence.

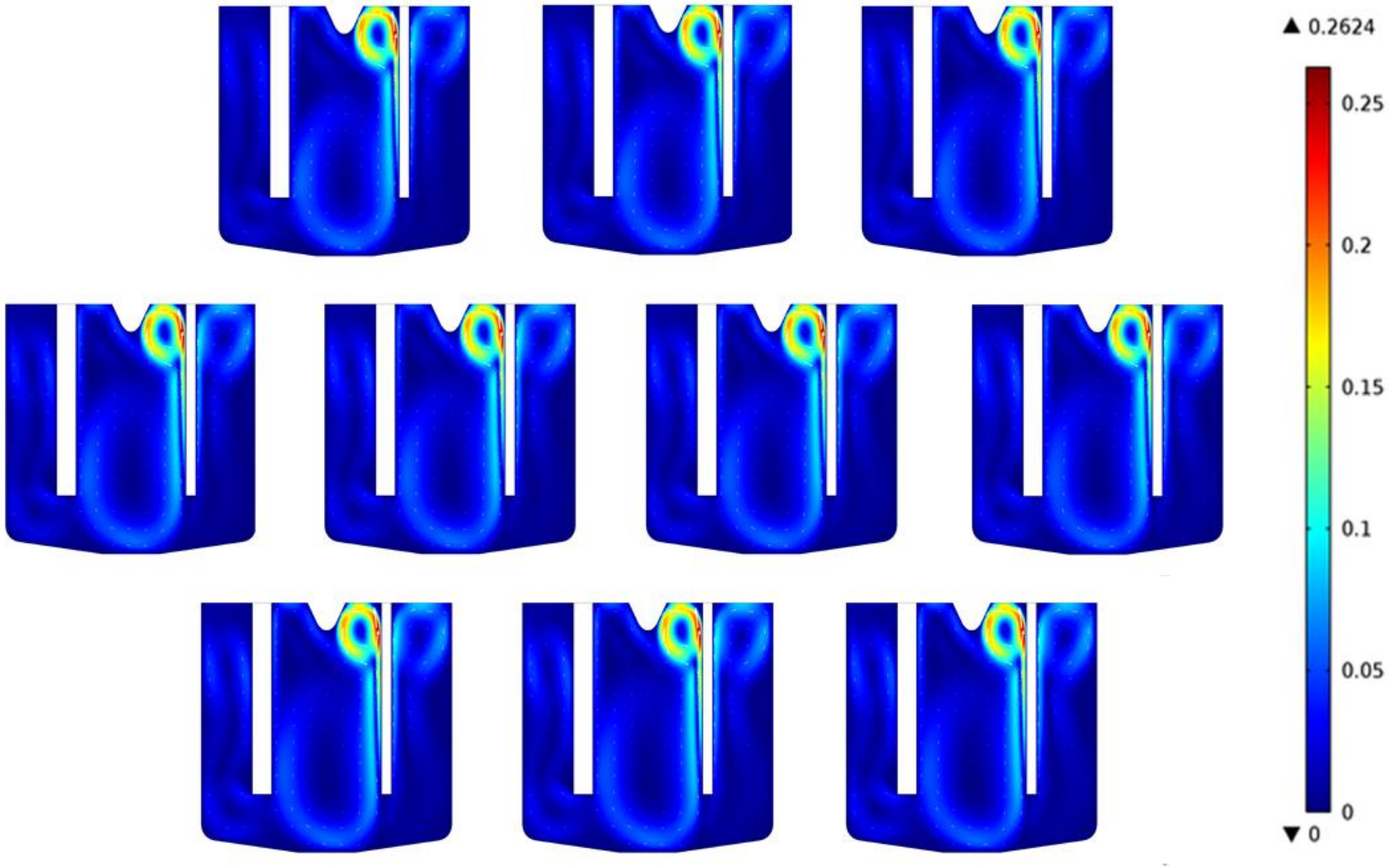

Figure 4-7: Liquid phase velocity time development sequence.

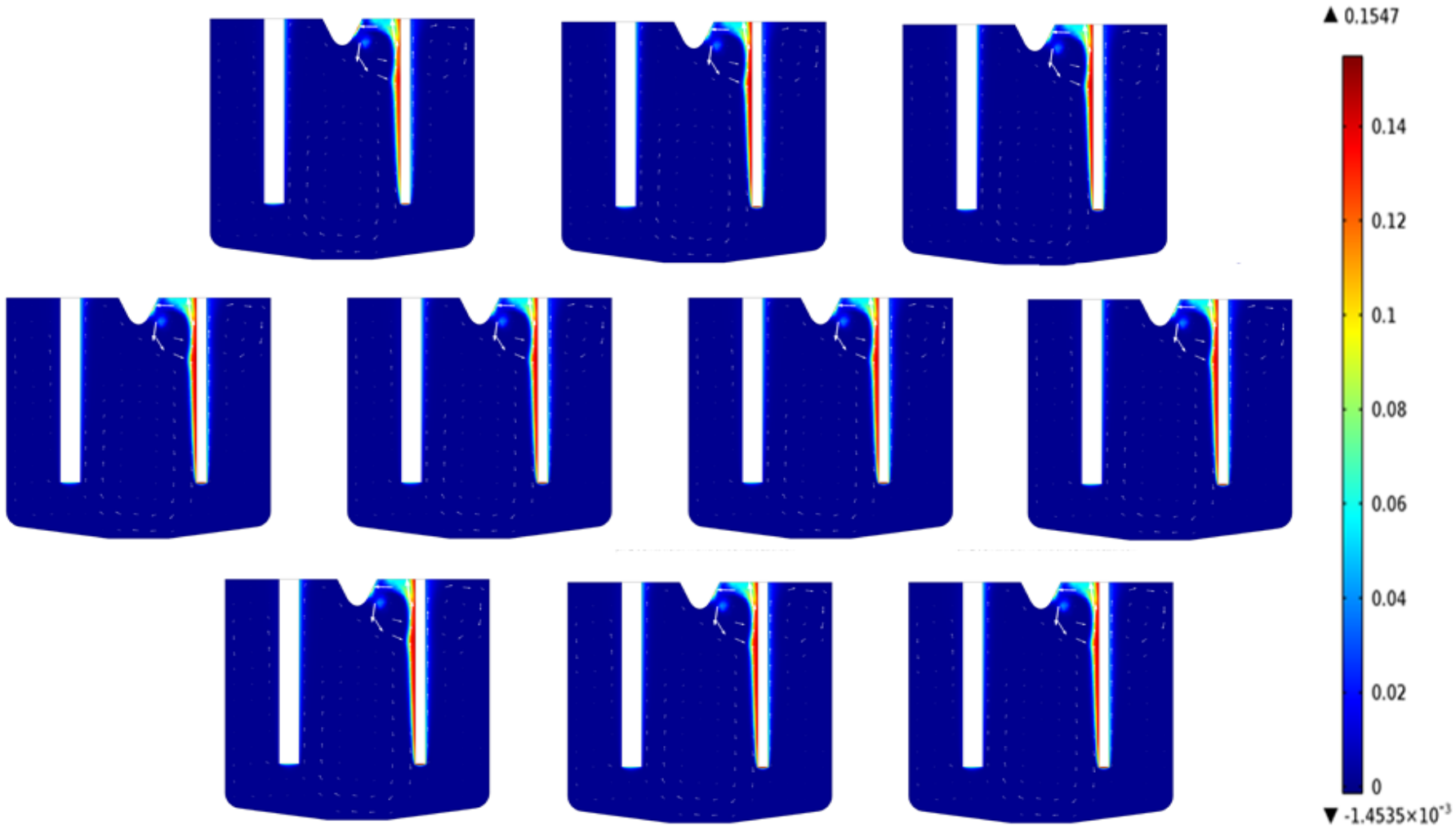

Figure 4-8: Gaseous phase volume fraction time development sequence.

4.2 Heat Transfer

The temperature distribution inside the reactor is shown in Figure 4-9, the colour scale on the right indicates temperature in kelvin; warmer colours represent higher temperatures and *vice versa*.

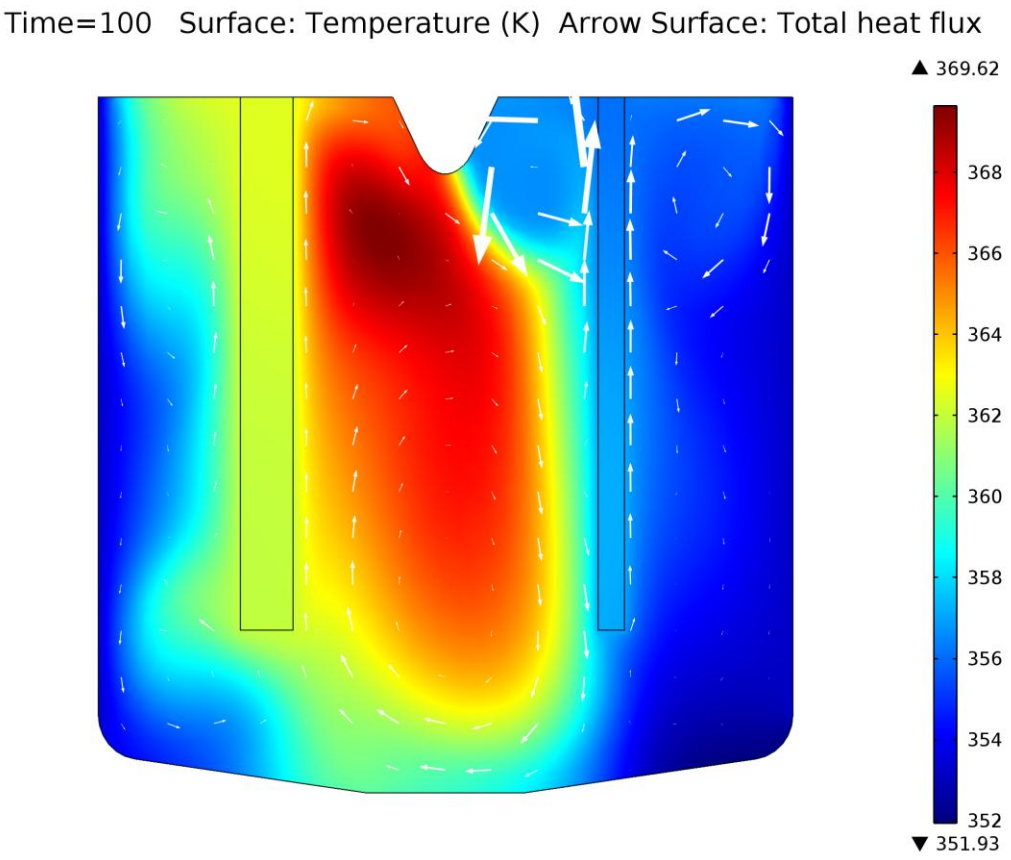

Figure 4-9: Heat flux and reactor temperature profile.

Ohmic heating is the major source of reactor heating as reflected by the current density concentration seen in Figure 4-17. A lot of heat is generated at the bottom of the electrodes as these are the points where the highest current density exists and therefore the most heat is generated here. The stirring effect of the moving liquids, induced by the moving gases, and shown by the vector arrows are visible in Figure 4-9. These arrows represent total heat flux inside the reactor. The size of the arrow is proportional to magnitude of the heat flux and

the arrow points in the direction of heat flux at the arrow origin. The heat flux arrows indicate that convection as the dominant heat transfer contributor, as heat flux takes up the same “shape” as that of the electrolyte motion. The cooling effect of the reactor walls and radiation heat loss can also be seen as the temperature decreases closer to the cooled wall and bottom of the reactor.

The heat flux within the reactor is further broken down in to conductive (Figure 4-12) and convective (Figure 4-12) heat flux to supply additional information concerning heat flux and its contributing components. Super-imposed on both images are arrow that indicate direction and magnitude of flux.

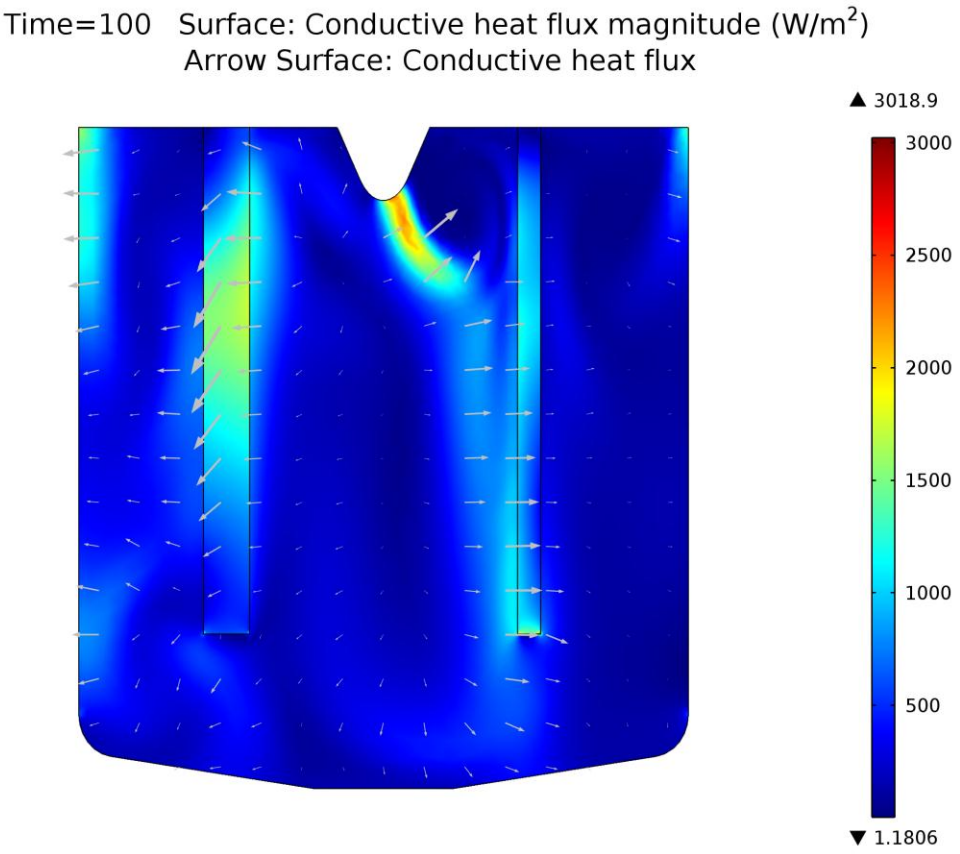

Figure 4-10: Conductive heat flux within the reactor.

From Figure 4-12 it is clear that heat is removed at the sides of the reactor *via* the cooled walls and some *via* radiation from the bottom of the reactor. Although

convection from the top of the electrolyte was included in the model, the effects appear negligible.

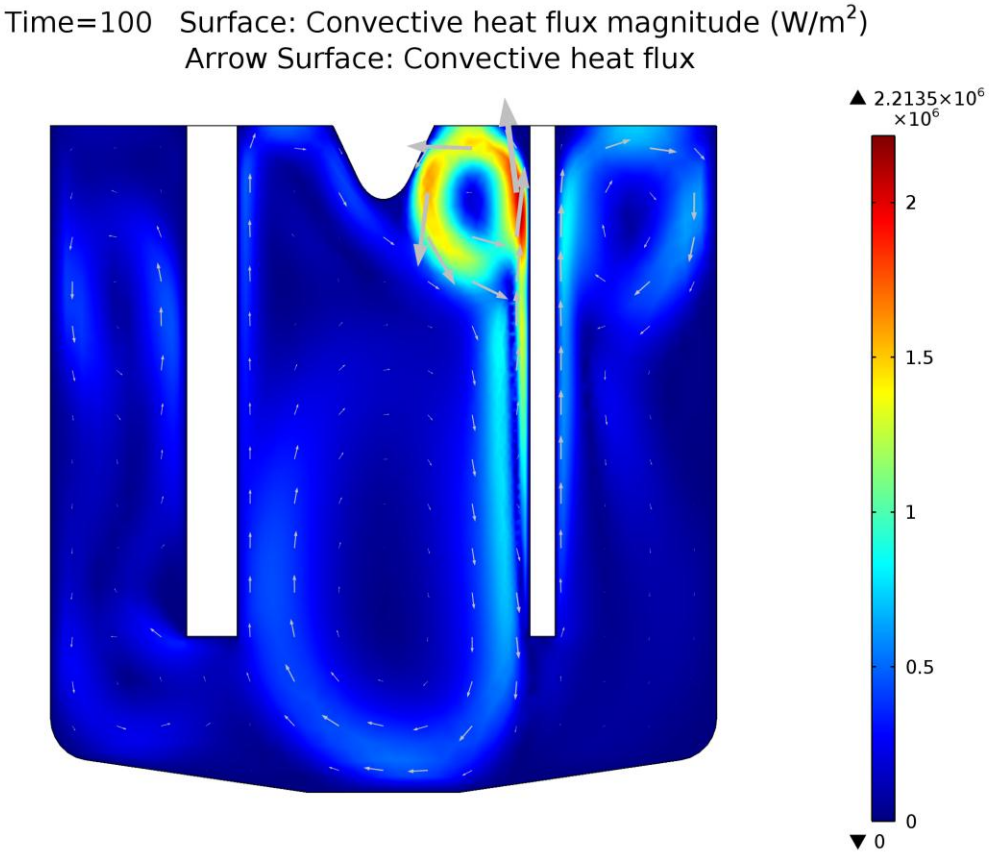

Figure 4-11: Convective heat flux within the reactor.

Looking at the magnitude of the heat flux vector in Figure 4-12, it can be concluded that convection is the major contributor to heat transfer within the reactor with a seven hundred times higher maximum flux than conduction.

4.2.1 Time Progression

The progression of temperature in the reactor can be seen in Figure 4-12. The time progression plots show how the temperature within the reactor changes from the starting temperature of 80 °C to the maximum temperature shown due to Ohmic-heating. The rise in temperature is initially fast but slows as time passes.

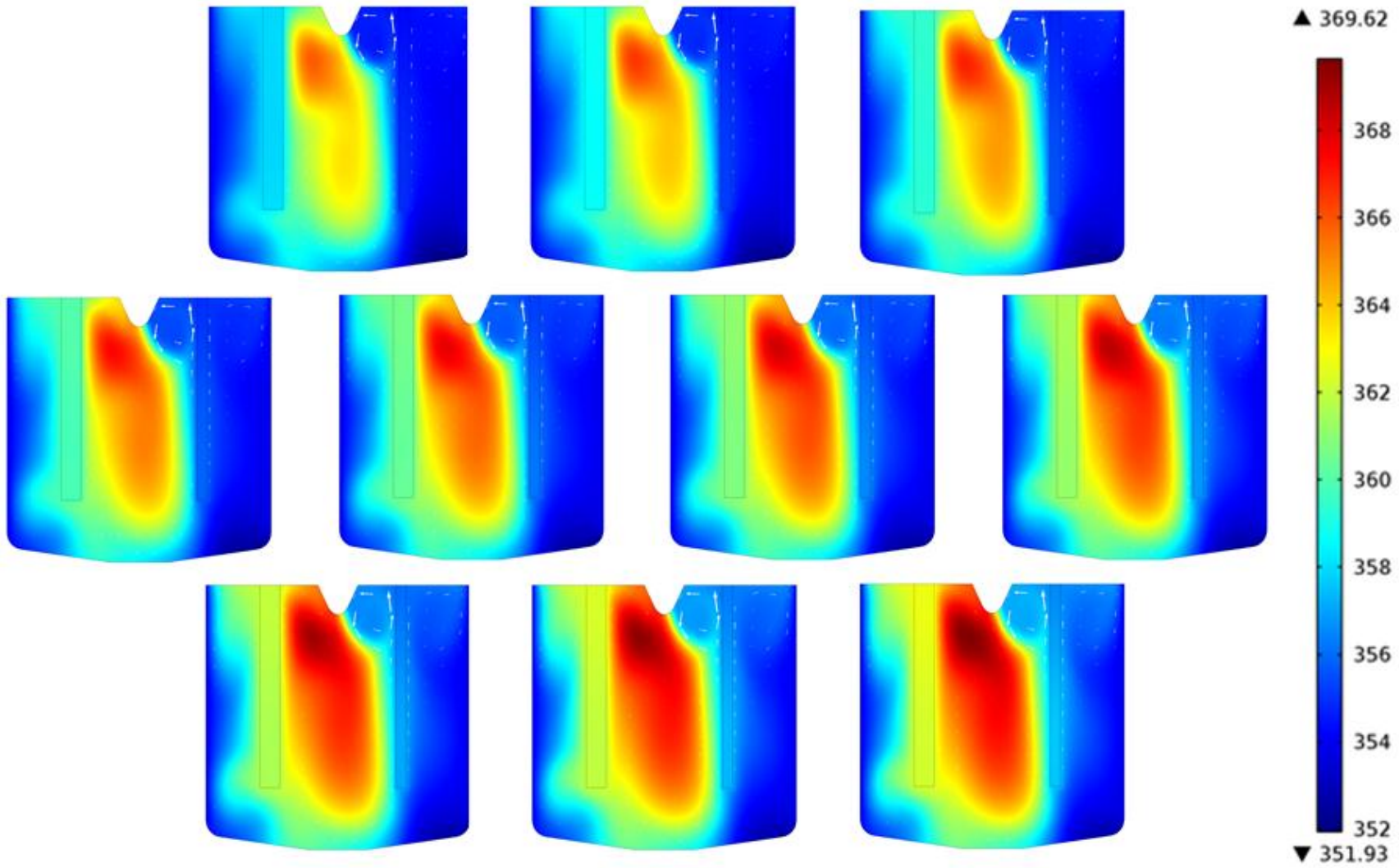

Figure 4-12: Temperature time progression sequence.

4.2.2 Parametric Study

A parametric study was done on how different values of electrolyte thermal conductivity influence the temperature profile in the reactor. Thermal conductivity was chosen as it has a very large influence on the temperature of the reactor. Further reasons include the fact that the value thermal conductivity used in the initial simulations was estimated from the value of the thermal conductivity of potassium fluoride. The temperature is turn is coupled to charge-, mass- and momentum transfer. Scale factors chosen for thermal conductivity was: 0.1, 0.5, 5 and 10. The results can be seen in Figure 4-13, Figure 4-14, Figure 4-15 and Figure 4-16 respectively. Work by Roustan et al. (1997) also indicated the importance of the thermal conductivity term during simulation.

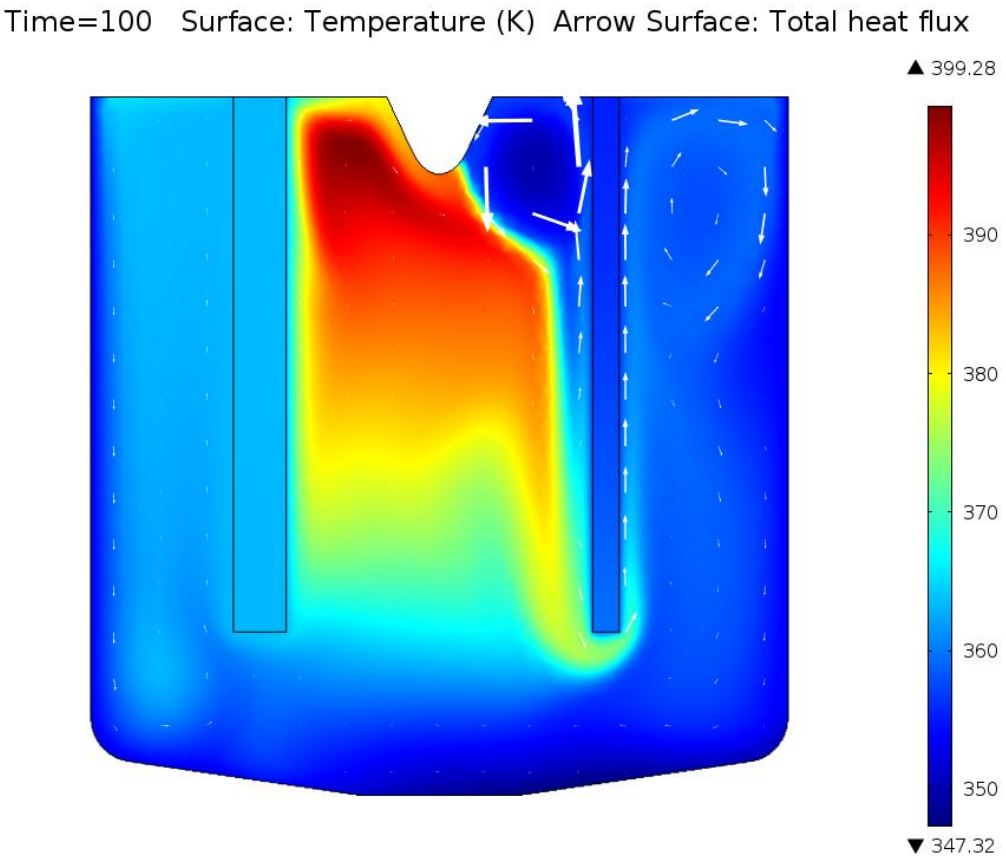

Figure 4-13: Heat flux and reactor temperature profile for an electrolyte thermal conductivity one tenth of the value stated in Table 3-7.

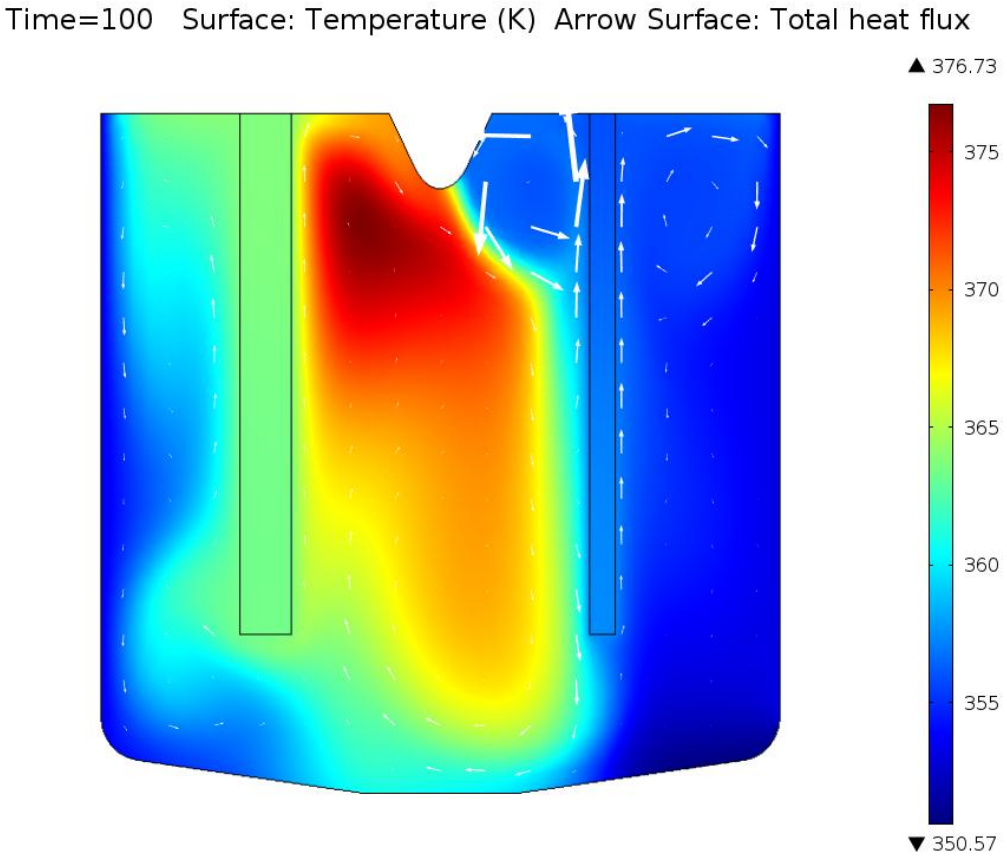

Figure 4-14: Heat flux and reactor temperature profile for an electrolyte thermal conductivity half of that stated in Table 3-7.

Results from the parametric study show that the maximum temperature as well as the heat distribution in the reactor varies with a change in thermal conductivity. It is however noted that even an increase in thermal conductivity by a factor 10 only changes the maximum reactor temperature by less than 30 *K*. The same can be said for lowering the conductivity by a factor of 10, a maximum temperature increase of only 13 *K*. An increase in thermal conductivity leads to a more symmetric temperature distribution.

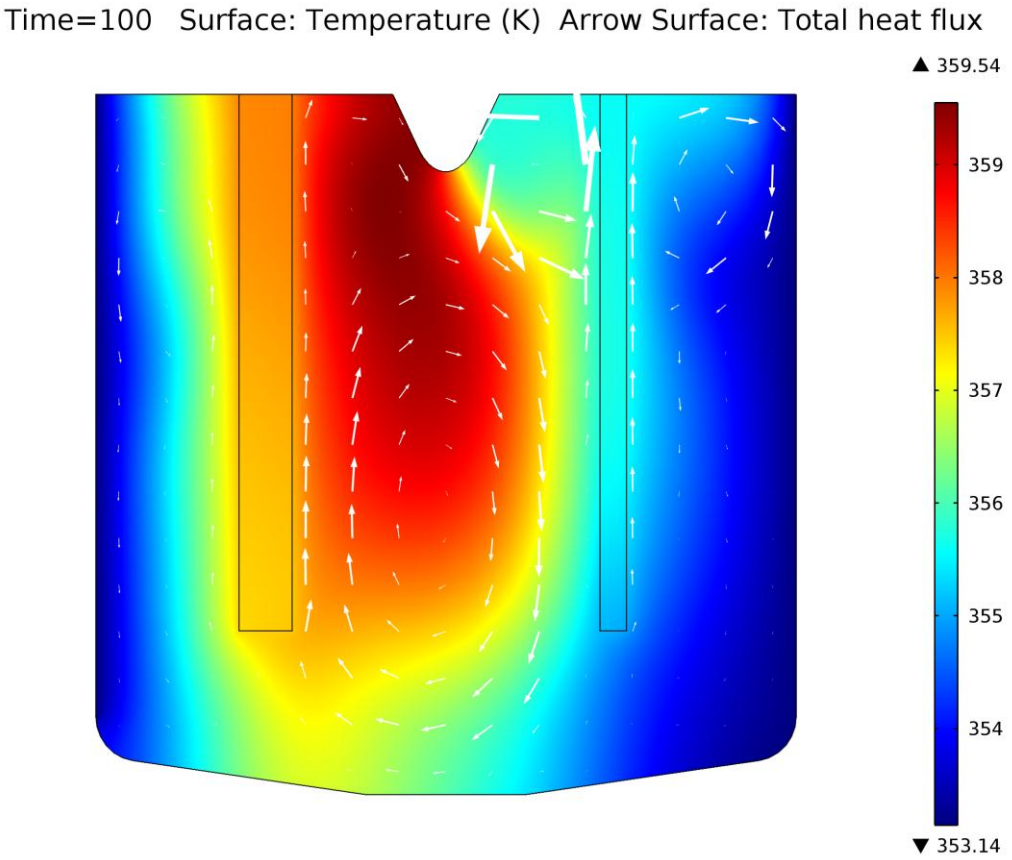

Figure 4-15: Heat flux and reactor temperature profile for an electrolyte thermal conductivity five times higher than stated in Table 3-7.

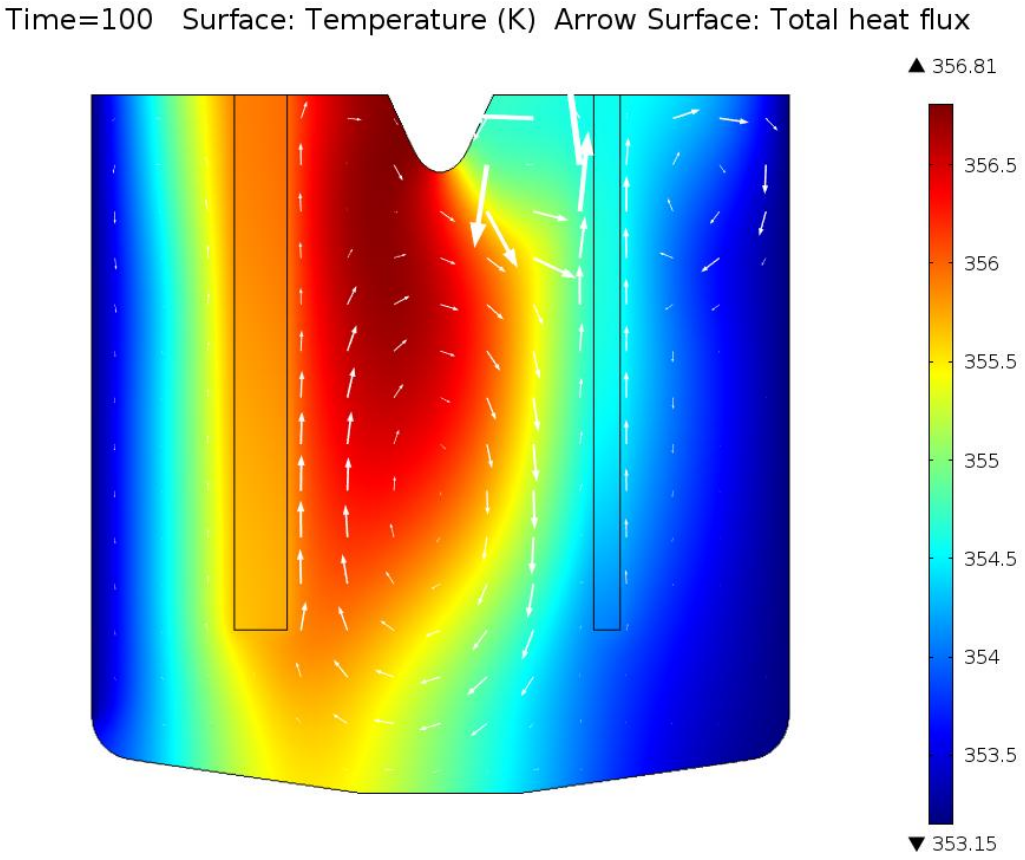

Figure 4-16: Heat flux and reactor temperature profile for an electrolyte thermal conductivity ten times higher than stated in Table 3-7.

4.3 Charge Transfer

The normal current density distribution inside the electrolysis reactor can be seen in Figure 4-17. The colour scale represents current density in $A \cdot m^{-2}$, warmer colours indicate higher densities. This figure also contains streamlines indicative of electric field lines between the electrodes.

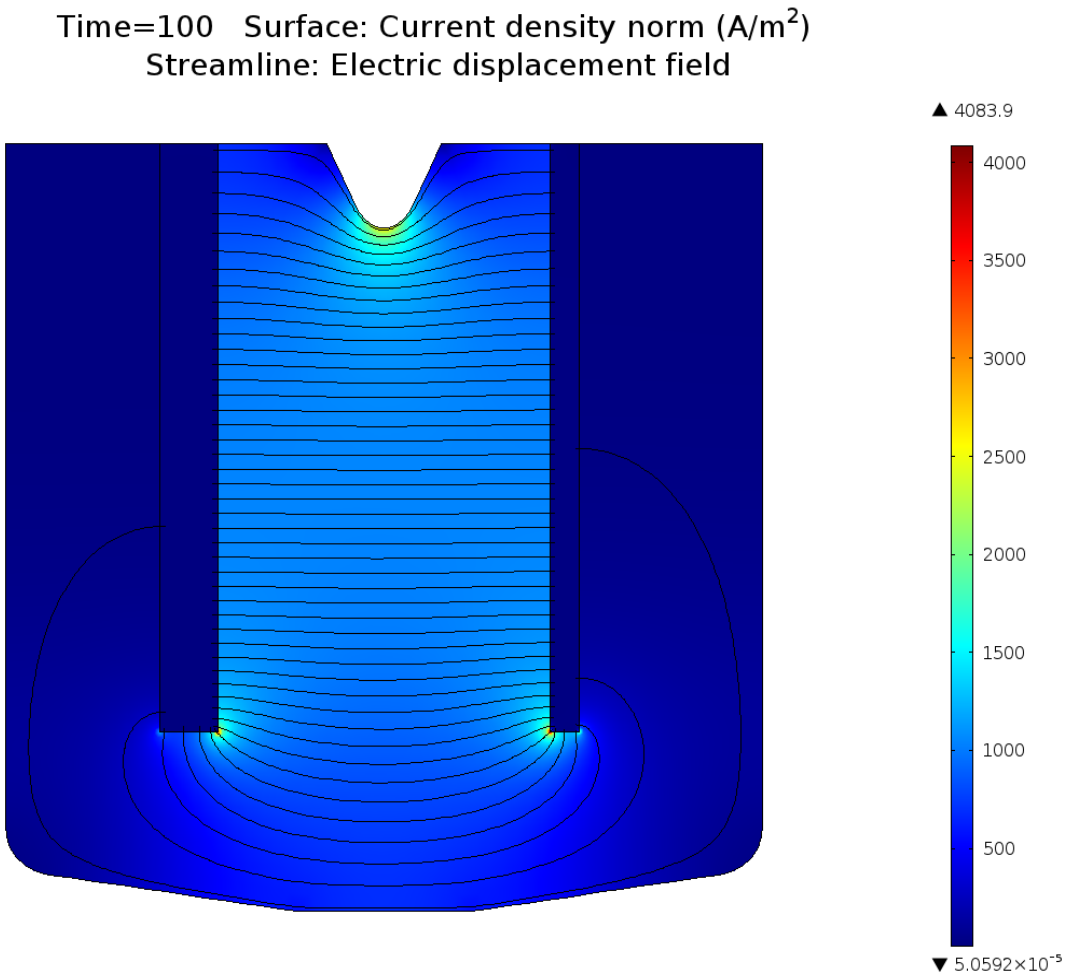

Figure 4-17: Current density distribution and electric field streamlines.

High current densities appear on sharp corners of the electrodes; especially high values are visible on tips between the two electrodes. Current density is also very high on the tip of the separator skirt. The tip of the skirt has such a high current density due to the fact that the charged ions flow around this point to travel between electrodes. These are major heat sources during electrolysis.

Current density variation along the anode is shown in Figure 4-19. It should be clarified at this point that “Arc-length” is in fact the distance travelled along the anode (and cathode). The “Arc length” axis starts on the top left of the anode and ends at the top right. This is further explained in the underlying image (Figure 4-17).

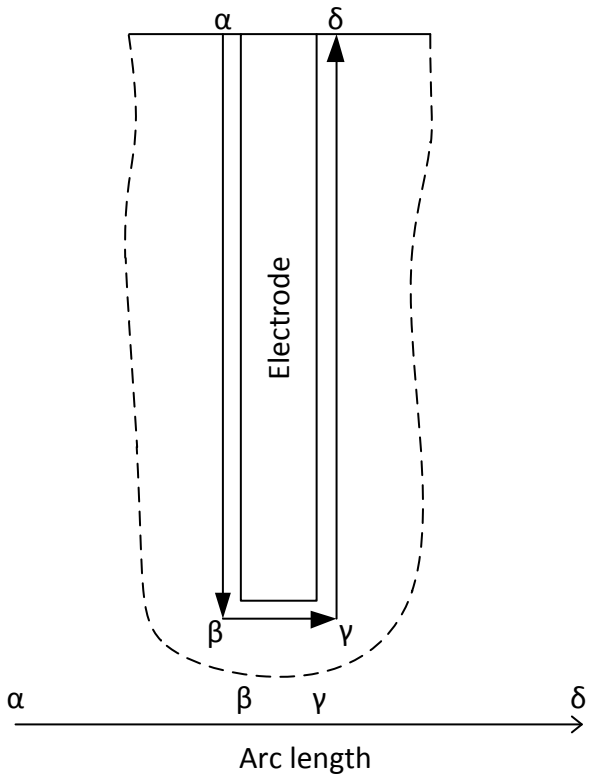

Figure 4-18: Graphical explanation of "Arc-length" as used in underlying figures.

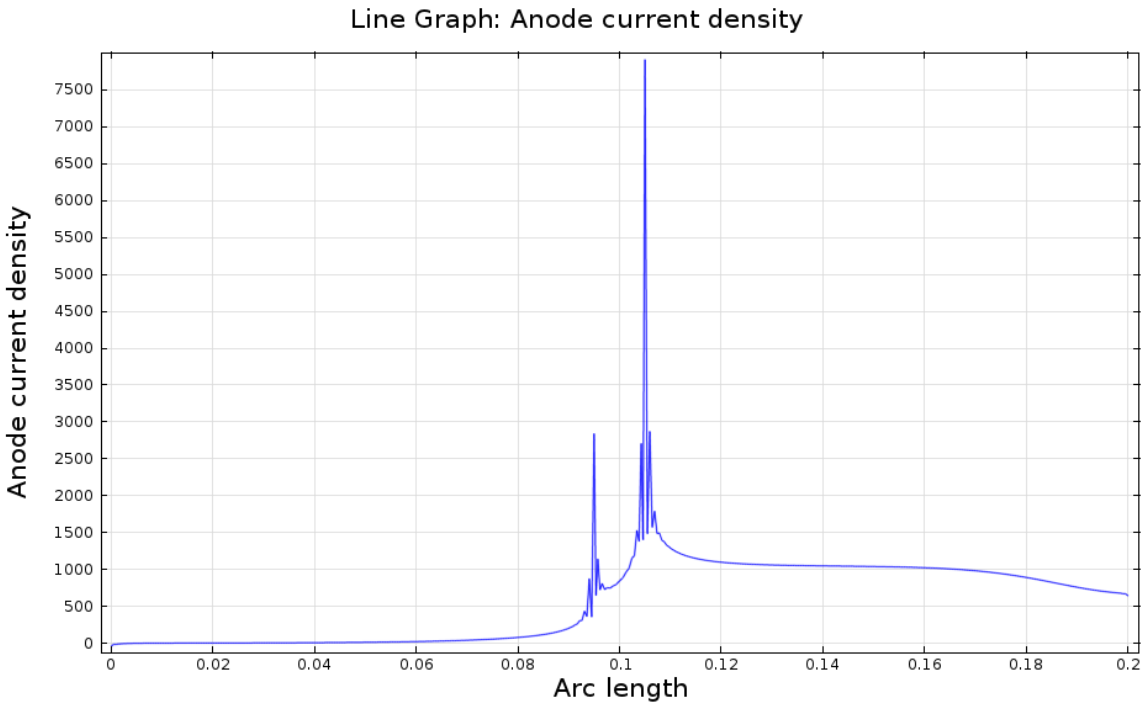

Figure 4-19: Anode current density variation along the electrode.

From Figure 4-19 it is clear that the current density is exceptionally high at the tips of the electrode. This caused some difficulty during the mathematical solution procedure. The current density spikes serve as a virtual discontinuity when moving between mesh nodes, making it difficult for the Newtonian solver to find a solution. The problem was overcome by refining the mesh around the high current density areas and by decreasing the size of steps taken by the solver. In reality these current density spikes can lead to electrode degradation in the reactor. The mirror of this image (Cathode Current Density Variation) is shown in Figure 4-20. In Figure 4-20 the “Arc Length” axis starts on the top left of the cathode and ends at the top right.

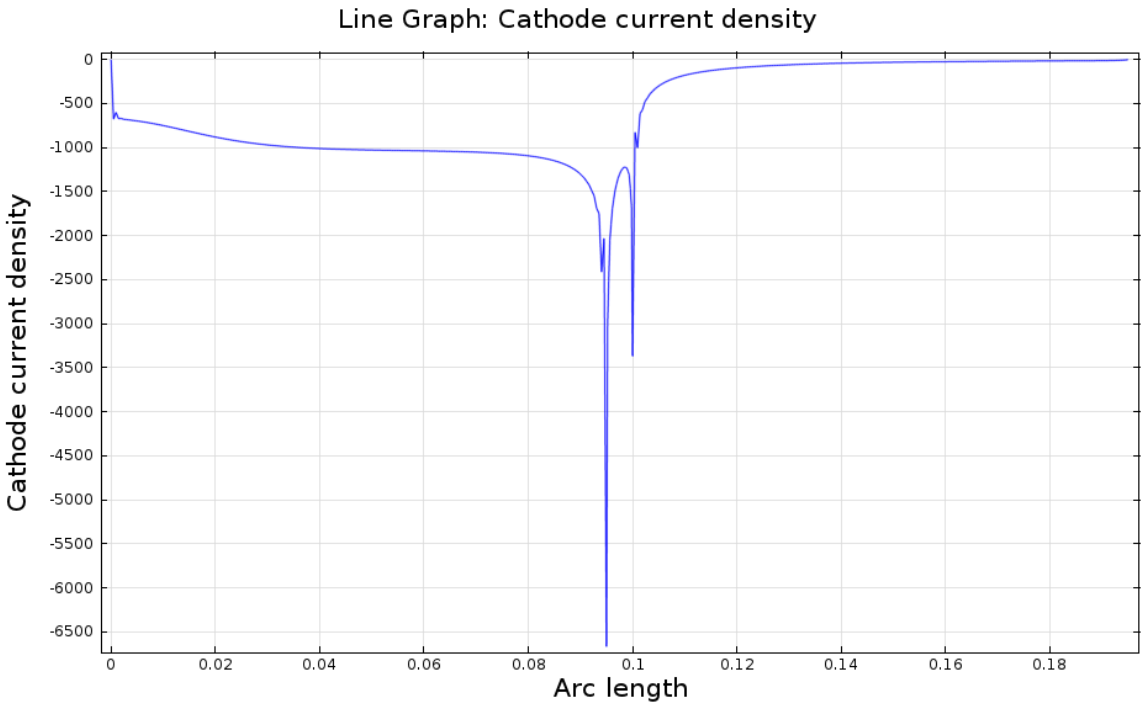

Figure 4-20: Cathode current density variation along the electrode surface.

Figure 4-21 shows the electric potential and electric potential contour lines within the electrolyte. The colour scale indicates electric potential in V, warmer colours indicate higher voltages.

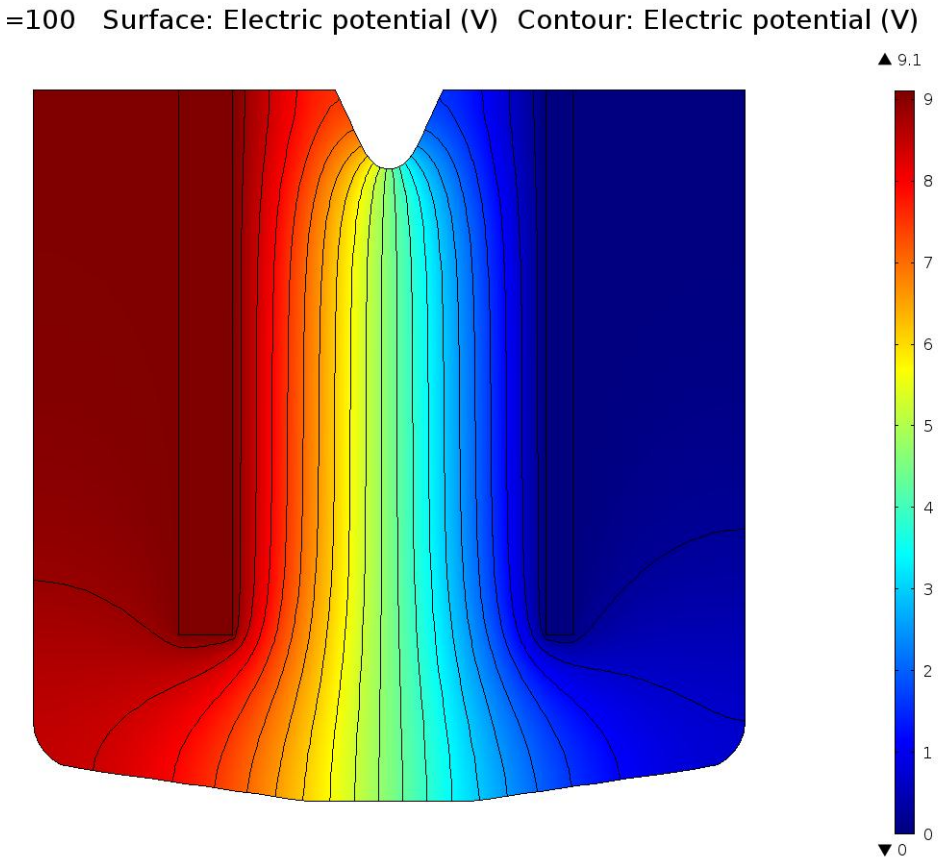

Figure 4-21: Electric potential plot.

Electric potential drops linearly from the anode to the cathode from 9.1 V and 0 V as expected. This result corresponds to the potential change expected from the literature. Literature however shows that the potential drop is in fact not linear. Boundary affects such as bubbles causes a large potential drop, due to the low conductivity of the gaseous phase resulting in an exponential potential drop over these bubbles on the boundaries.

The bending of the electric potential contour lines along the separator skirt corresponds to the electric current density field lines that bend around the skirt.

4.4 Mass Transfer

HF concentration in mol·m^{-3} is shown in Figure 4-22; the colour scale shown indicates high HF concentrations at warm colours and low concentrations at cold colours. The vector arrows indicate direction- and the size of the arrows indicate magnitude of flux at the arrow origin.

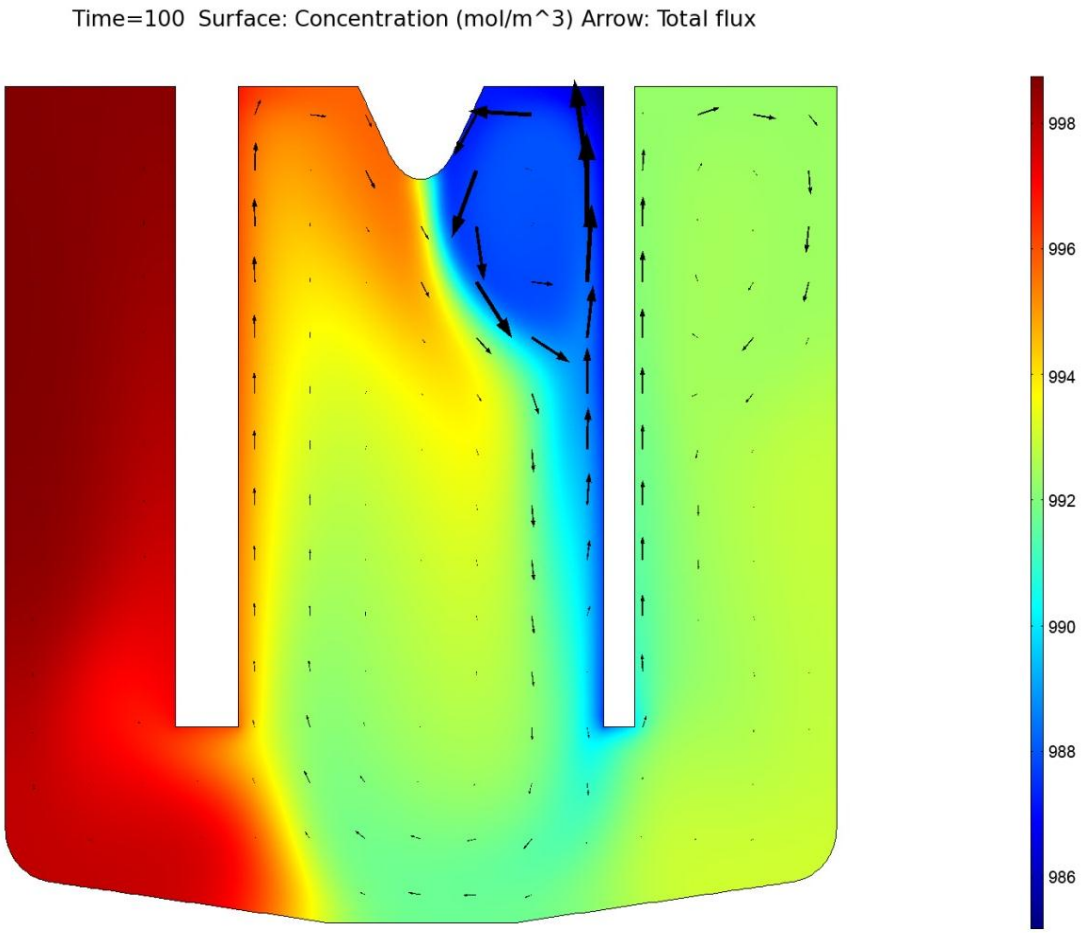

Figure 4-22: Dissolved hydrogen fluoride flux and flux vectors.

HF is produced at the anode and consumed at the cathode. The concentration gradient due to consumption at the cathode is a contributor to flux in the form of diffusion. From the scale-bar on the right it is clear that more HF is consumed than produced, as was predicted by the electrode half-reactions (Equation 3-8

and Equation 3-9). From Figure 4-22 it is evident that the secondary contributors to flux are convection and migration due to electric field.

HF_2^- ion-flux and concentration are shown in Figure 4-23. Arrows size indicates flux magnitude at arrow origin and arrow directions indicate flux direction. Concentration is in $mol \cdot m^{-3}$ and warmer colours represent higher concentrations.

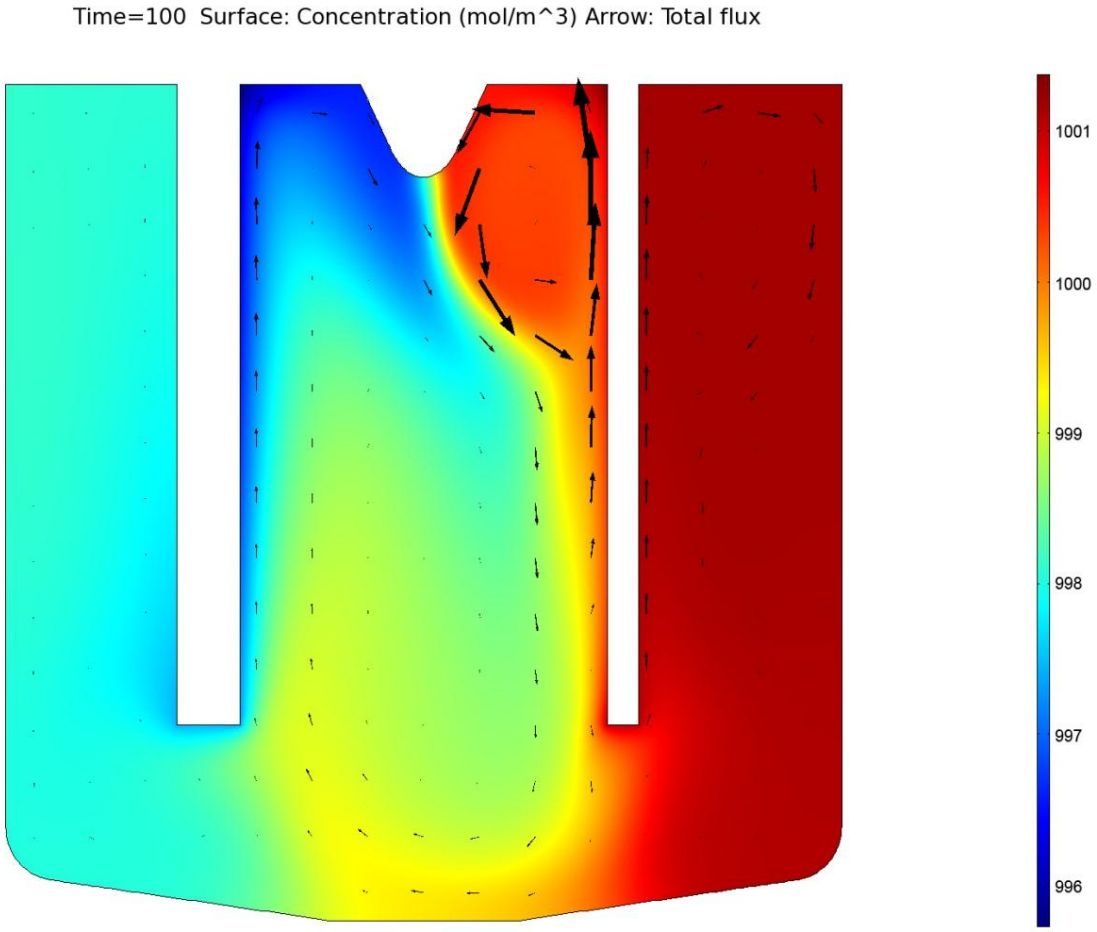

Figure 4-23: Hydrogen difluoride anion-flux

The HF_2^- ion is produced at the cathode and consumed at the anode. This is reflected in Figure 4-23. The concentration gradient indicates ion-flux from the cathode to the anode as expected. Convection is evident as the major contributor to ion-flux in the simulation, with diffusion due to concentration gradient and migration due to electric field acting as secondary contributor.

4.4.1 Time Progression

Figure 4-24 and Figure 4-25 shows the time dependent development of the hydrogen fluoride and hydrogen difluoride dissolved species respectively. It is clear when looking at Figure 4-24 and Figure 4-25 that initially there is consumption and formation at both electrodes. The gas-phase induced electrolyte movement is major contributor to mixing of diluted species. Other than the formation of a clearly defined mixing pattern within the reactor, not much else changes except the diluted species concentrations. The change in reactant concentration relative to the starting value is extremely low. The quasi-steady state assumption was therefore not violated.

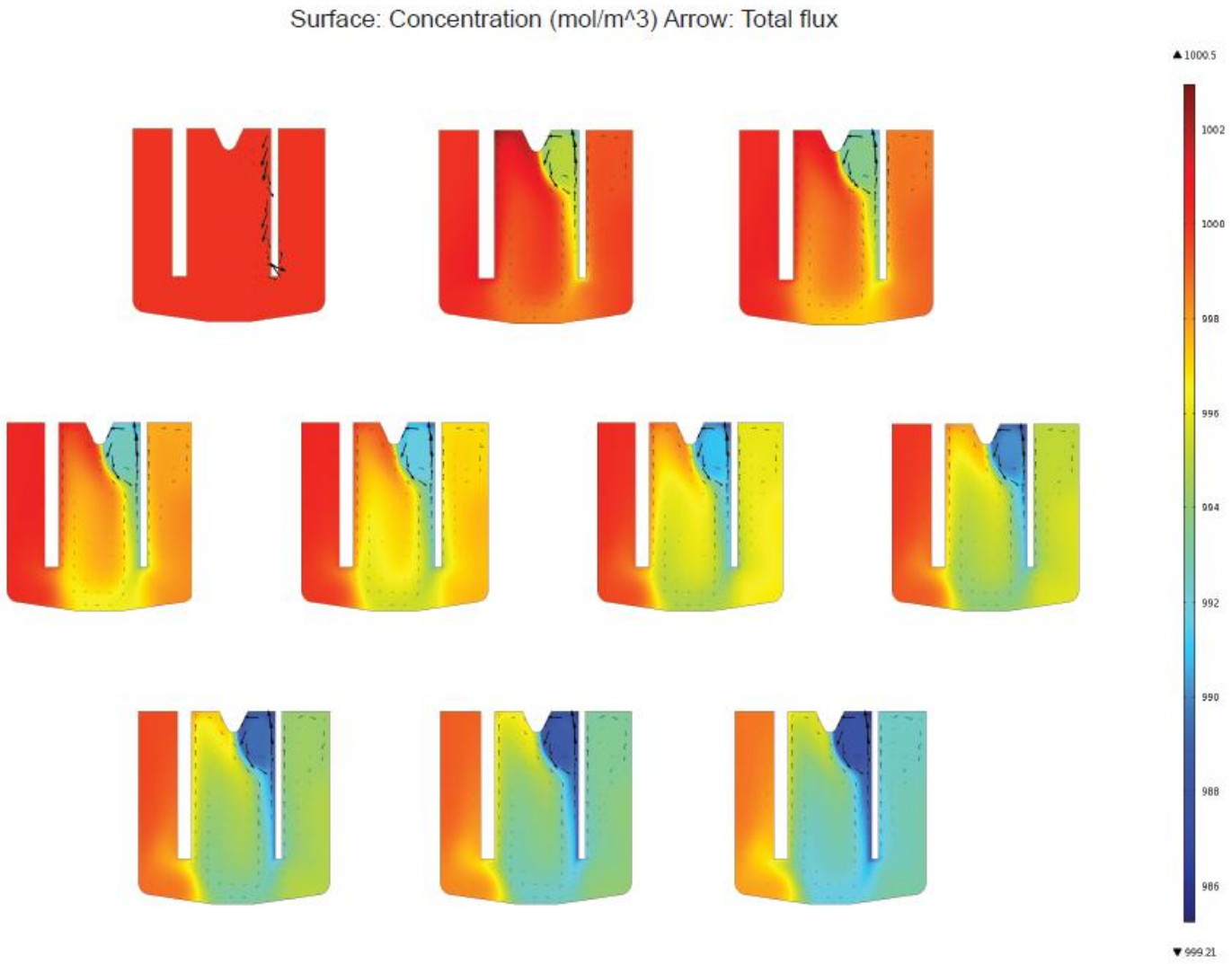

Figure 4-24: Time dependent representation of HF concentration over time.

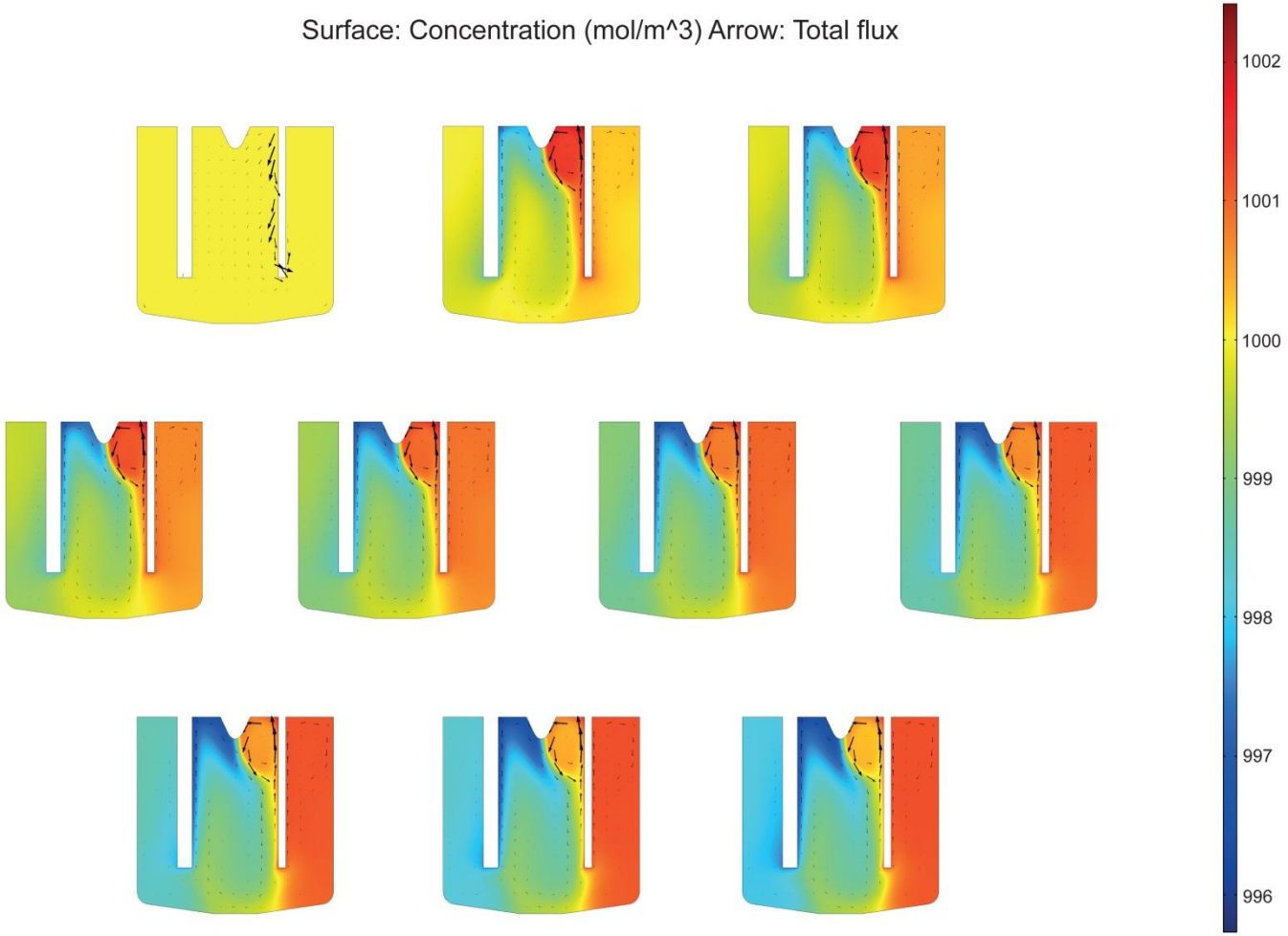

Figure 4-25: Time dependent representation of HF_2^- concentration over time.

4.5 Simulations of Published Results

This section contains the results of the authors' attempts to simulate published results. Simulations used parametric data if available in a publication. Assumptions were made where parametric data was unavailable. Specialised correlations and equations used in published works that could not be reproduced were supplemented with the modelling procedure as described in section 3.2 of this report.

4.5.1 Modelling coupled transfers in an industrial fluorine electrolyser (Roustan et al., 1997)

A COMSOL Multiphysics simulation of the fluorine electrolyser published by the Roustan *et al.* (1997) was also completed by the author. Dimensions supplied were used as well as parameters supplied. Not all data required for simulation were supplied in the publication. The missing information required for simulation was taken from Table 3-7 and Table 3-8 as used for own work. Extracted expressions from these tables are presented in Table 4-1. Parameter values that were unavailable or unusable when extracted are shown in Table 4-2.

Table 4-1: Extracted expressions as used in COMSOL simulation.

Extraction	***Description***	***Expression***
Non-uniform current distribution	Current density along the electrodes was described by the Butler-Volmer equation. Data concerning the uniform current density used in the publication was unavailable.	Equation 2-8
Total heat production	The expression used in the publication to describe total heat production requires a value for the thermo-neutral voltage of the cell, this was not supplied, and a value was therefore extracted.	Equation 3-5

Table 4-2: Assumed parametric values as used in COMSOL simulation.

Assumed value	***Description***	***Value***
Exchange current density	A constant value was assumed over the anode	$12\ A \cdot m^{-2}$
Cooling coil temperature	Data concerning the cooling capacity of the coils were unavailable, a constant value for coil temperature was assumed	$325\ K$

The resulting equipotential curve is shown in Figure 4-26.

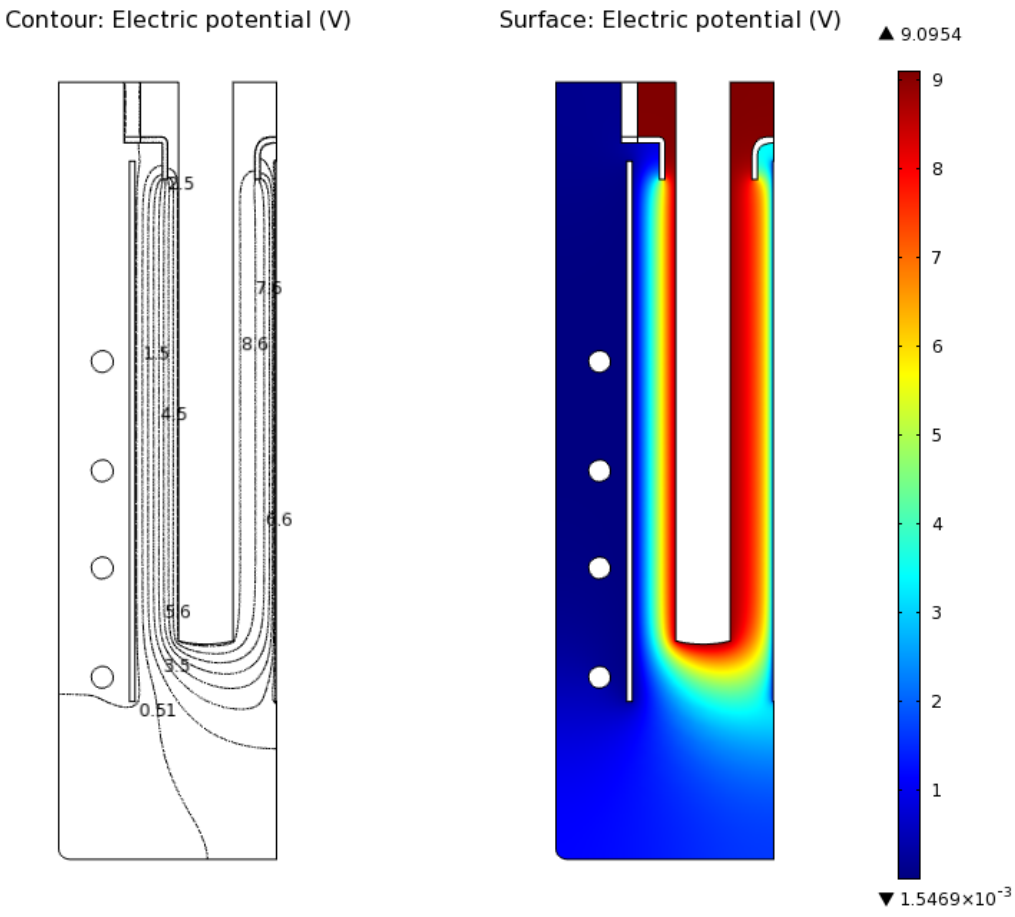

Figure 4-26: Equipotential curves from the COMSOL simulation of the cell as published by Roustan *et al.,* (1997).

When comparing the equipotential curves to those obtained in Figure 2-7 by Roustan and co-workers a similar voltage drop between the electrodes can be observed. The shape of the curves are nearly identical between the electrodes, but differs for the rest of the cell. A possible explanation could be that the minimum voltage corresponds, but the maximum voltage is 1.9 V lower. The results from Figure 2-7 and Figure 4-26 align well with the results found in Figure 4-21, both in shape and value.

Comparison of these curves with those obtained in Figure 2-7 by Roustan and co-workers, reveals a similar voltage drop between the electrodes. These curves are shaped nearly identically between electrodes, and differ only slightly at the tip of the anode. There are also differences in terms of the potential drop on the opposite side of the cathode. The equipotential curves, shown in Figure 4-26, match well to those seen in Figure 2-7.

Using this electric potential data of the electrolyser as input to a coupled thermal simulation delivers the simulation seen in Figure 4-27. The model further makes us of a coupled velocity profile model as induced by thermal differences throughout the reactor. The velocity field can be seen in Figure 4-28.

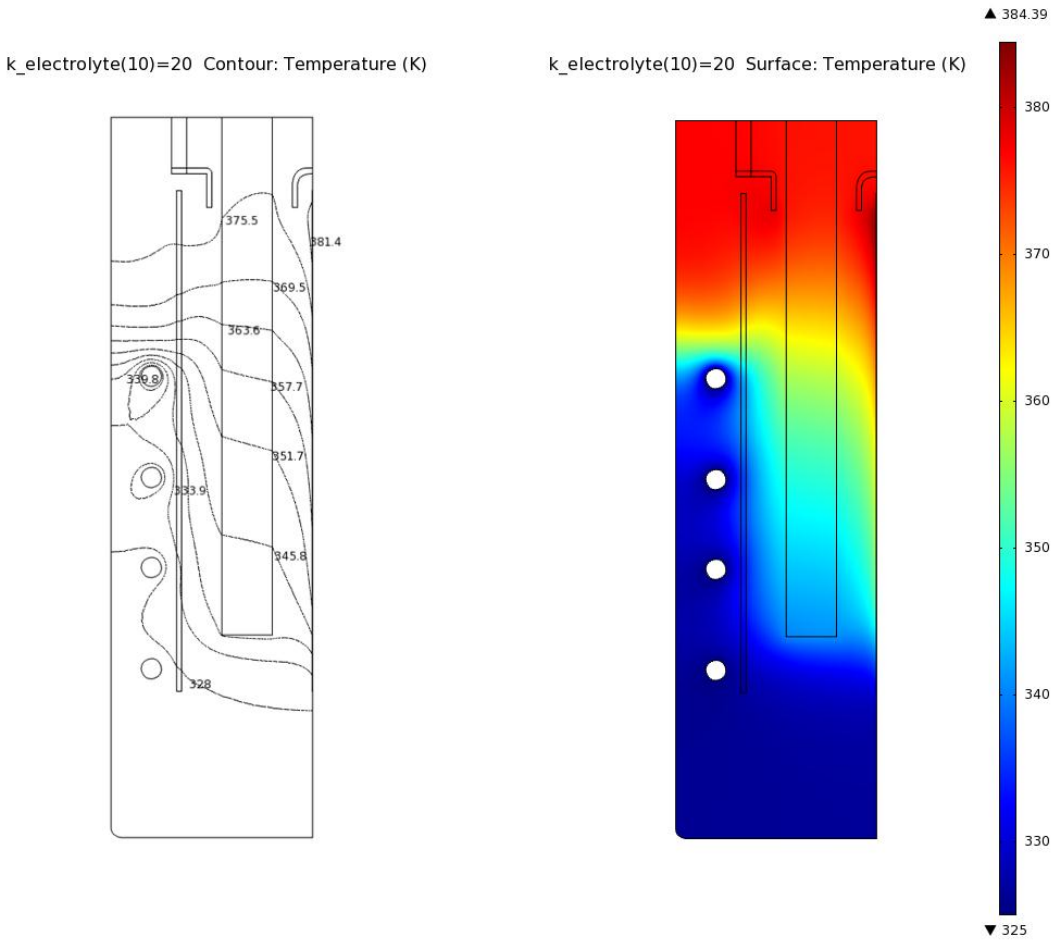

Figure 4-27: Temperature profiles inside the reactor as simulated in COMSOL.

Note that initially a value for thermal conductivity of $1.25\ W \cdot m^{-1} \cdot K^{-1}$ was used in the author's simulation. With a thermal conductivity value of $20\ W \cdot m^{-1} \cdot K^{-1}$ (as used by Roustan *et al.,* 1997) a temperature distribution that matches up well with that of the Roustan group (Figure 2-10) is observed (Figure 4-27).

The remaining deviation can possibly be attributed to the fact that the Roustan simulation removes heat from the electrolyte with an undisclosed equation. The author merely specifies a temperature of 325 *K* at the cooling coils (as stated earlier). Another explanation could be that the author does not incorporate radiative heat losses from the sides of the reactor. This was not included as it

would complicate the simulation without adding significant accuracy to the results.

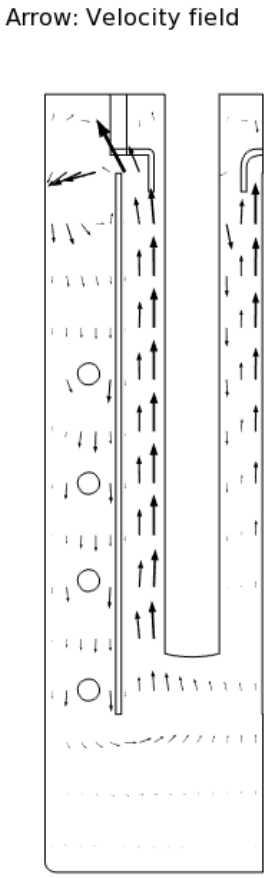

Figure 4-28: Velocity vectors of electrolyte movement inside the reactor as simulated by COMSOL.

Results from Figure 4-28 compare well with that of Figure 2-11. The eddies observed at the bottom and top of the reactor are however absent (bottom) or less intense (top). A favourable comparison between Figure 4-3 and 2-13 is also observed.

A possible explanation for the simulations not matching up even at such extreme parameter modification could be the cooling potential of the four cooling coils. In this simulation they are all set to a constant value of 325 K instead. The

simulation by Roustan *et al.* (1997) uses a cooling flow determined experimentally and not presented in the publication. Furthermore the deviation could also possibly be explained by the fact that the Roustan simulation incorporates heat loss *via* radiation. This was not done by the author as it complicates the simulation without adding significantly to the results.

4.5.2 Effect of hydrodynamics on Faradaic current efficiency in a fluorine electrolyser (Espinasse et al., 2006)

The cell described in the publication by Espinasse *et al.* (2006) was simulated using COMSOL Multiphysics. Pressure, viscosity and density of electrolyte and hydrogen as well as bubble diameter as specified in the publication were used in this simulation. The reader should note that due to insufficient data supplied in the aforementioned publication, assumptions were made concerning the dimensions, electrical- and hydrodynamic conditions within the cell. The values used are supplied in Table 4-3. Boundary values were kept similar wherever possible. The size of the cell was estimated from measurements made of the published graphical results.

The result of the first COMSOL simulation is presented in Figure 4-29. The gas fraction shown in Figure 4-29 is the gas fraction of hydrogen. The flow rate as stated in Table 4-3 was chosen to ensure a similar hydrogen plume shape as that obtained by the Espinasse group.

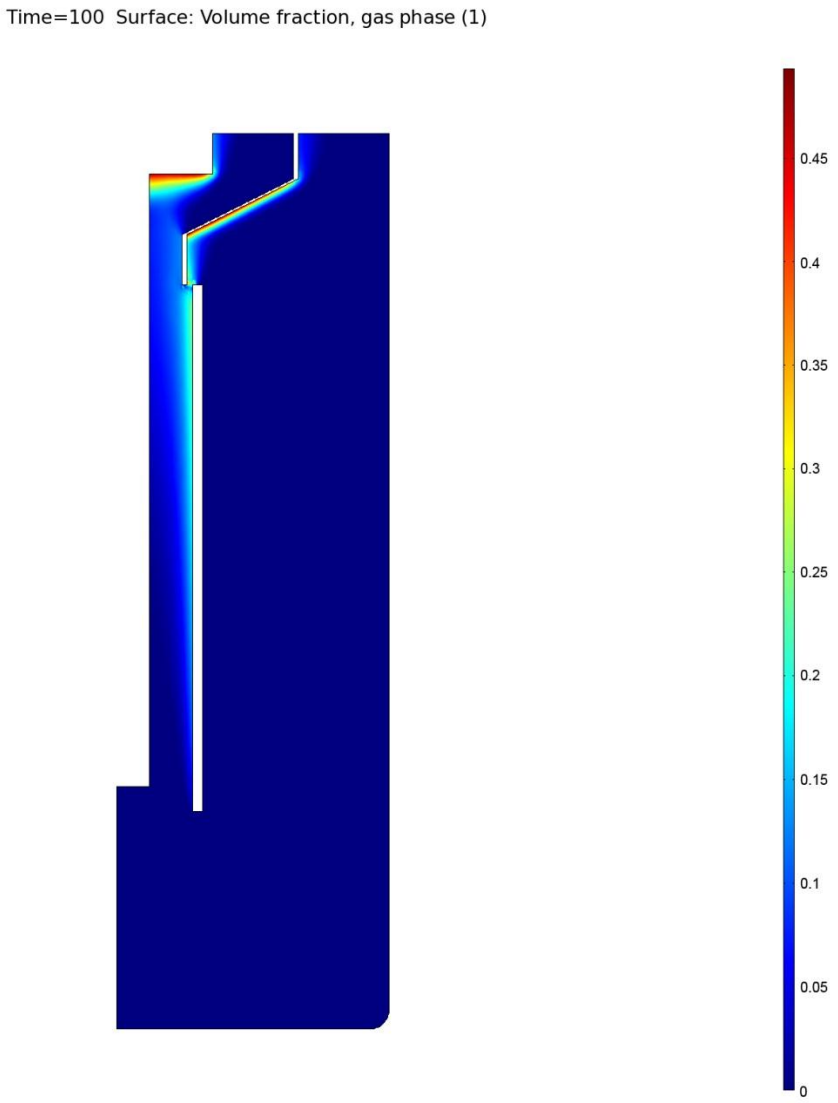

Figure 4-29: COMSOL simulation of published (*Ibid.*) electrolyser.

Table 4-3: Assumed parametric values as used in COMSOL simulation.

Assumed value	***Description***	***Value***
Temperature	The reactor temperature was assumed to remain constant at the value given.	$273\ K$
Gas flux from cathode	This value was assumed to remain constant over the entire surface of the cathode	$1\times10^{-4}\ kg\cdot m^{-2}s^{-1}$

A comparison can be drawn between Figure 4-29 and Figure 2-16. Comparison of the two sets of results shows a similar hydrogen plume but significantly higher gas fractions to those of the Espinasse group. There is also significantly more overflow of hydrogen into the fluorine compartment. A second attempt was made to obtain similar gas fractions. These results are shown in Figure 4-30.

The hydrogen flow rate from the cathode was reduced by two orders of magnitude in an attempt to get similar gas fraction results as those shown in Figure 2-16. A maximum gas fraction of the same order of magnitude was obtained. These values are however too small to be noticeable on the simulation produced by COMSOL Multiphysics.

Compared with Figure 2-15, a similar gas fraction is seen, but a significant loss of hydrogen plume shape is observed. In Figure 2-17 from section 2.5.4 a bubble plume in a water solution can clearly be observed. If one assumes that a hydrogen plume in a fluorine electrolyser has the same shape and gas fraction, it becomes clear that the shape obtained by Espinasse *et al.* (2006) and this author's simulations are correct. It does however cast some doubt on the gas fraction values obtained by in the publication. The image of a hydrogen plume from Mandin *et al.*, (2009) has shown that the expected gas fraction of a gaseous plume formed during water electrolysis is at least one order of magnitude higher than that obtained by Espinasse *et al.* (2006). It is however noted that a hydrogen bubble in water (shape, volume or size) cannot be used as an exact template for hydrogen bubbles in any other electrolytic medium. It is merely used as a rough reference in this case. The gas fraction published by Espinasse and co-workers also compares unfavourably with the results from Figure 4-5 where a gas fraction value higher by an entire order of magnitude was found.

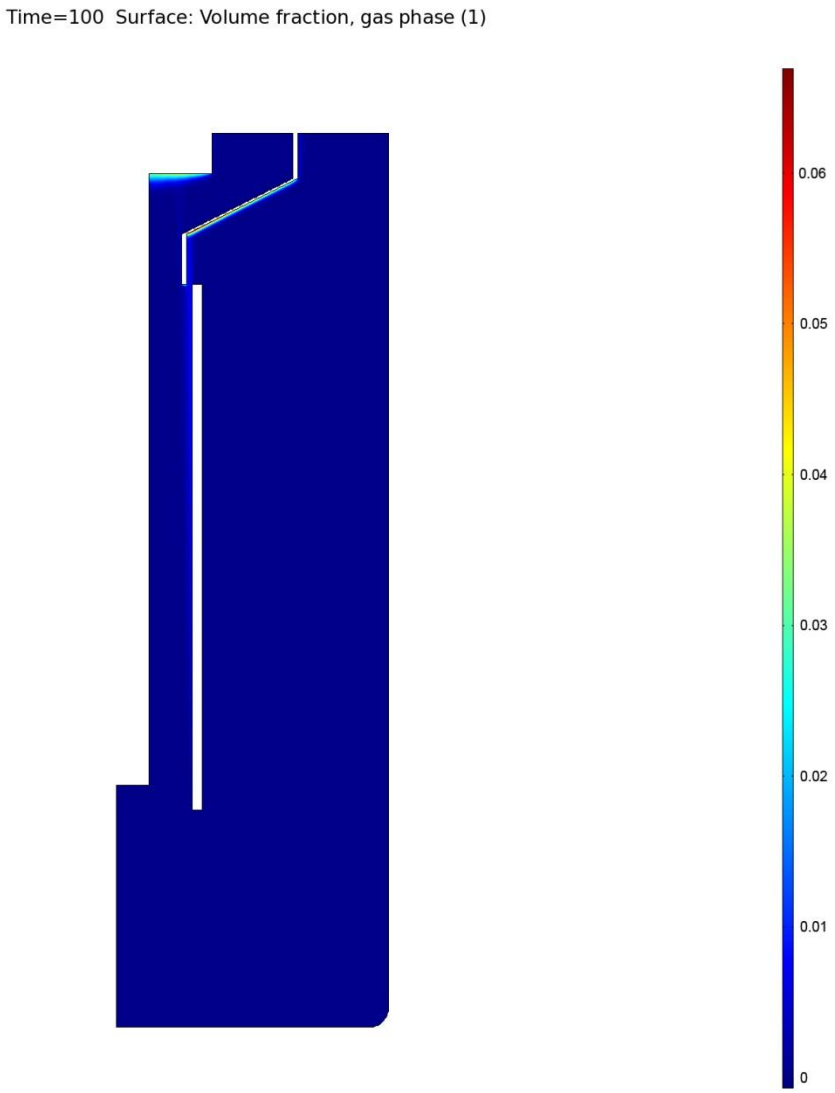

Figure 4-30: COMSOL simulation of published (*Ibid.*) electrolyser where similar gas fractions are attempted.

5 Conclusions and Recommendations

5.1 Experimental Design Simulation

Results obtained from the simulations are reasonable and within expectations. A plot of average liquid velocity in the reactor (Figure 4-1) shows that the flow conditions within the reactor very rapidly reach a steady state, indicating that one can easily assume that the conditions within the reactor will not change much as time progresses. In other words a quasi-steady-state condition has been reached. This is observation is also reflected in the time progression plots of the section four of this report. The results will act as a workable lead in the experimental enquiry that is to follow.

5.1.1 Momentum Transfer

The simulated results show a strong correlation between the gaseous phase movement (induced by buoyancy forces) and that of the liquid phase. When comparing Figure 4-2 and Figure 4-3 it can be seen that the liquid phase flow is induced by the gas phase flow. This in turn causes eddying of the gas near the hydrogen compartment exit. The gas-phase flux seen in Figure 4-5 shows that little or no hydrogen gas transfers to the fluorine compartment which could lead to explosive recombination during experimentation. Small bubbles may however be entrained in the electrolyte flow. The time progression images of Figure 4-6, Figure 4-7 and Figure 4-8 show that the quasi-steady state assumption is valid, as there is very little observable change even after just 20 s of simulated time progression.

A *posteriori* evaluation of the liquid velocity at the anode could indicate a modification of the fluorine production might be advantageous in increasing the accuracy of the model.

The shape of the gaseous plume of hydrogen that forms at the anode has the same shape as that published in literature when compared to the results from Espinasse *et al.* (2006) and Mandin *et al.* (2009). There is however a difference in the gaseous fraction between the published and simulated reactors.

5.1.2 Heat Transfer

The steady-state results obtained from Figure 4-9 shows that there is a build-up of thermal energy in-between the electrodes. Figure 4-9 further shows that convection induced by electrolyte movement aids in thermal energy redistribution within the reactor towards the cooled walls and radiation cooled bottom of the reactor. The change of temperature with time within the reactor shown in Figure 4-12 indicates that the temperature continuously rises within the reactor. It is however also observed that the rate of heating slows down significantly after 55 s. It can therefore be assumed that the maximum reactor temperature will only be a few degrees higher than that shown in Figure 4-9. It was shown that convective heat transfer is the major contributor to heat flux by Figure 4-11 and Figure 4-11.

When comparing the parametric study results obtained from Figure 4-13 to Figure 4-16 to that of Figure 4-9 it can be seen that the heat transfer conditions inside the reactor are dependent on the thermal conductivity of the electrolyte. Values of thermal conductivity lower than those used in the initial simulations indicate the formation of hotspots and higher maximum temperatures. Values of thermal conductivity higher than those used in the initial simulation show a more even temperature distribution and a lower maximum temperature. Despite the large variation in thermal conductivity values (values of between a tenth and ten times higher) there is very little change in average reactor temperature (±1,5 ^{o}C/increase in k_t) and maximum reactor temperature (±30 ^{o}C). It is therefore the conclusion of the author that the values of electrolyte conductivity used is a satisfactory value to use in future simulations.

A good correlation was found when comparing simulated reactor temperature results and those found by Roustan *et al.* (1997), even though radiative heat loss was neglected.

It is recommended that parametric data and mathematical correlations be refined to achieve maximum accuracy for temperature distribution inside a fluorine electrolysis reactor. This will be beneficial for the current and future models.

5.1.3 Charge Transfer

The current density distribution seen in Figure 4-17 is within expected limits. Higher current density concentrations are observed on the sharp corners of the electrodes, as expected. It is however recommended that a correlation be included in future models that will account for the resistivity of the bubbles forming on the electrode surfaces (as done by Roustan *et al.,* 1997). The effects of the double layer should also be included. These modifications will serve to more accurately portray the potential drop between the two electrodes. Field lines also assume the shape expected. Electric potential observed in Figure 4-19 have satisfactory shapes and values. These values also match up satisfactorily with those found by Roustan *et al.* (1997).

5.1.4 Mass Transfer

Results from Figure 4-22 and Figure 4-23 are exactly what were expected. Consumption and production of relevant species occur where expected. Mixing of the diluted species occur by electrolyte motion induced by gaseous production. It can be concluded that liquid phase movement induced by gas phase movement is the main contributor to mixing within the reactor. Convection completely overshadows that mixing effect of electric field migration of charged species and that diffusion due to concentration gradients. It is recommended that

the fluorine production kinetics be investigated to deliver more accurate mass transfer results in future.

Mass transfer is the only transfer process that continuously changes with time as observed in Figure 4-24 and Figure 4-25. The change is however so slight that it does not significantly alter results of the other transfer processes.

5.2 Comparison with Published Results

5.2.1 Effect of hydrodynamics on Faradaic current efficiency in a fluorine electrolyser (Espinasse et al., 2006)

A comparison of the published results by Espinasse *et al.* (2006) and those simulated by the author on COMSOL using similar reactor conditions show some deviation. When a similar plume shape was obtained the gas fraction differed from those obtained by the Espinasse group. An attempt to achieve the same gas fraction resulted in a very dissimilar hydrogen plume. Comparison of the gas fraction obtained by Espinasse co-workers with Figure 2-17 of Mandin *et al.* (2009), casts some doubt on the gas fraction reported.

5.2.2 Modelling coupled transfers in an industrial fluorine electrolyser (Roustan et al., 1997)

An attempt by the author to model the results published by Roustan *et al.* (1997) resulted in good comparison between the electric field contour plots. The same can be said for the velocity profile. The reactor temperature profile deviated only slightly. This could be attributed to the heat production equation used by the author and/or the heat removal in the COMSOL simulation (i.e. the exclusion of radiative heat loss). The Roustan group uses an unspecified heat flux at the cooling coils, where the COMSOL simulation uses a boundary condition constant at 325 *K*.

6 Acknowledgments

I would like to thank a few people who made this project possible: J.P. Caire as external examiner, whose valuable critique, advice and insights during the marking of the initial draft of this dissertation, were incorporated in the final edition; C. J Hattingh from MTC cc, local representative of COMSOL Multiphysics for the software and on-going support during this investigation. Lastly I would like to thank Paul Sonnendecker for the design and construction of the fluorine cell simulated in this report, and Necsa whose financial support made this study possible.

7 References

Burden, LB, Faires, J D (2005) *Numerical Analysis*, Thomson Brooks/Cole, Belmont.

Burkhardt, ER, Brüning, J (2003) Ullman's Encyclopedia of Industrial Chemistry, WILEY-VCH GmbH & Co. KGaA, Weinheim. Volume 29, "Potassium and Potassium Alloys", Chapter 1 p81-83.

Çengel, YA (2006) *Heat and Mass Transfer,* McGraw-Hill, Singapore.

CHENCO GmbH, 2007 "CHENCO Company Presentation", `http://chenco.de/downloads/` [2011, March 23].

Caire, JP, Chifflet H (2002) "Meshing Noise Effect in Design of Experiments Using Computer Experiments" Environmetrics 13: 437–444 (2001).

Clark, DL, Neu, MP, Runde, W, Keogh, DW (2005) "Uranium and Uranium Compounds", in *Kirk-Othmer Encyclopaedia of Chemical Technology,* 25, Seidel Arza (Editor-in-Chief), John Wiley & Sons, Inc., New Jersey.

COMSOL Multiphysics (a), Chemical Engineering Modules User's Guide, *Bubbly Flow*, Version 4.0, 164-173 (April 2010). COMSOL and COMSOL Multiphysics are registered trademarks of COMSOL AB.

COMSOL Multiphysics (b), Heat Transfer Modules User's Guide, *Theory of Heat Transfer*, Version 4.0, 1-14 (April 2010). COMSOL and COMSOL Multiphysics are registered trademarks of COMSOL AB.

COMSOL Multiphysics (c), AC/DC Modules User's Guide, *Fundamentals of Electromagnetics*, Version 4.0, 40-46 (April 2010). COMSOL and COMSOL Multiphysics are registered trademarks of COMSOL AB.

COMSOL Multiphysics (d), Chemical Engineering Modules User's Guide, *Transport of Diluted Species*, Version 4.0, 253-268 (April 2010). COMSOL and COMSOL Multiphysics are registered trademarks of COMSOL AB.

Crouse, PL (2010) “Properties of Lab-Scale Fluorine Electrolysis Cell” Personal Communication, Department of Chemical Engineering, University of Pretoria, Pretoria.

Crassous, I, Groult H, Lantelme, F, Devilliers, D, Tressaud, A. Labruge` re, C, Dubois, M, Belhomme, C, Colisson, A, Morel, A (2009) “Study of the Fluorination of Carbon Anode in molten KF-2HF by XPS and NMR Investigations” Journal of Fluorine Chemistry, 130 1080–1085.

Espinasse, G, Peyrard, M, Nicolas, F and Caire JP (2006) “Effects of hydrodynamics on Faradaic current efficiency in a fluorine electrolyser” Journal of Applied Electrochemistry (2007) 37:77-85.

Frank, BF, Warren, WE (2003) Ullman's Encyclopedia of Industrial Chemistry, WILEY-VCH GmbH & Co. KGaA, Weinheim. Volume 2, "Alumium", Chapters 1-4 p227-240.

Groult, H, Devilliers, D (2000) "Fluorine evolution at carbon/KF-2HF interface" *Journal of Fluorine Chemistry*, 263-267.

Groult, H (2003) "Electrochemistry of Fluorine Production" *Journal of Fluorine Chemistry*, 119 173-189.

Groult, H, Lantelme, F, Salanne, M, Simon, C, Belhomme, C, Morel, B, Nicolas, F (2007) "Role of Elemental Fluorine in Nuclear Field" *Journal of Fluorine Chemistry*, 128 285–295.

Häussinger, P Lohmüller, R and Watson, AM (2003) Ullman's Encyclopedia of Industrial Chemistry, Sixth Edition, WILEY-VCH GmbH & Co. KGaA, Weinheim. Volume 17, "Hydrogen", Chapters 1-4 p85-155.

Klose, F (2004) "Elements and Compounds, Atoms and Molecules – Structures and Bonds", Course on Inorganic Chemistry for the University of Magdeburg, Magdeburg.

Loth, E, Tryggvason, Y, Tsuji, Y, Elghobashi, SE, Clayton, Crowe, CT, Berlemond, A, Reeks, M, Simonin, O, Frank, Th, Onishi, Y and van Wachen, B (2006) "Modeling", in *Multiphase Flow Handbook,* Chapter 13, Crowe, CT (Editor-in-Chief), Taylor & Francis Group, Florida.

Newman, JS (1991) *Electrochemical Systems*, Prentice Hall, New Jersey.

Mandin, Ph, Wüthrich, R and Roustan, H (2009) “Electrochemical Engineering Modelling of the Electrodes Kinetic Properties During Two-Phase Sustainable Electrolysis” 10th International Symposium on Process Systems Engineering

Minz, FR (2003) Ullman’s Encyclopedia of Industrial Chemistry, WILEY-VCH GmbH & Co. KGaA, Weinheim. Volume 33, “Sodium Hydroxide”, Chapters 1-3 p235-240.

Heitz, E and Kreysa G (1986) *Principles of Electrochemical Engineering*, VCH Verslasgesellschaft mbH, Weinheim.

Hur, JS, Shin, CB, Kim, H and Kwonb, YS (2003) “Modeling of the Trajectories of the Hydrogen Bubbles in a Fluorine Production Cell” Journal of The Electrochemical Society, 150 (3), (2003) D70-D78.

Rudge, AJ (1971) “Production of elemental fluorine by electrolysis”, Industrial Electrochemical Processes, Kuhn, A (Editor), Elsevier Publishing Company, Amsterdam.

Roustan, H, Caire, JP, Nicolas, F, Pham, P (1997) “Modelling coupled transfers in an industrial fluorine electrolyser” Journal of Applied Electrochemistry, 28 (1998) 237-243.

Schmittinger (2003) Ullman’s Encyclopedia of Industrial Chemistry, Sixth Edition, WILEY-VCH GmbH & Co. KGaA, Weinheim. Volume 8, “Chlorine”, Chapters 1-4 p186-197.

Schumb, W C, Young, R C and Radimer, *K* J (1947) "Electrolytic Generation of Fluorine", Industrial Engineering Chemistry, vol 39 no. 3, 244-248.

Seidel, A (2004) (a) Kirk-Othmer Encyclopedia of Chemical Technology, Fifth Edition. John Wiley and Sons, Inc. Hoboken, New Jersey. Volume 7, Chapters 1-4 in “Copper” p670-688.

Seidel, A (2004) (b) Kirk-Othmer Encyclopedia of Chemical Technology, Fifth Edition. John Wiley and Sons, Inc. Hoboken, New Jersey. Volume 9, Chapters 1-11 in “Electrochemical Machining”, p590-605.

Seidel, A (2004) (c) Kirk-Othmer Encyclopedia of Chemical Technology, Fifth Edition. John Wiley and Sons, Inc. Hoboken, New Jersey. Volume 9, Chapters 1-4 in “Electrochemical Processing, Inorganic” p618-642.

Seidel, A (2004) (d) Kirk-Othmer Encyclopedia of Chemical Technology, Fifth Edition. John Wiley and Sons, Inc. Hoboken, New Jersey. Volume 9, Chapter in “Electrochemical Processing, Organic” p652-653.

Seidel, A (2004) (e) Kirk-Othmer Encyclopedia of Chemical Technology, Fifth Edition. John Wiley and Sons, Inc. Hoboken, New Jersey. Volume 9, Chapters 1-4 in “Electroplating” p759-767.

Seidel, A (2004) (f) Kirk-Othmer Encyclopedia of Chemical Technology, Fifth Edition. John Wiley and Sons, Inc. Hoboken, New Jersey. Volume 9, Chapters 1-5 in “Lithium and Lithium Compounds” p120-130.

Seidel, A (2004) (g) Kirk-Othmer Encyclopedia of Chemical Technology, Fifth Edition. John Wiley and Sons, Inc. Hoboken, New Jersey. Volume 15, Chapters 1-5 in “Magnesium and Magnesium Alloys” p321-338.

Seidel, A (2004) (h) Kirk-Othmer Encyclopedia of Chemical Technology, Fifth Edition. John Wiley and Sons, Inc. Hoboken, New Jersey. Volume 26, Chapters 1-5 in “Zinc and Zinc Alloys”, p554-578.

Shia, G (2005) “Fluorine”, in *Kirk-Othmer Encyclopedia of Chemical Technology,* 14, Seidel Arza (Editor-in-Chief), John Wiley & Sons, Inc., New Jersey.

Smith, JM, Van Ness, HC and Abbot HM (2005) *Introduction to Chemical Engineering Thermodynamics,* McGraw-Hill, Singapore.

Speciality Gasses of America, Inc. (2009), a “Tetrafluoromethane Material Safety Data Sheet”, Specialty Gases of America, Inc., Toledo.

Speciality Gasses of America, Inc. (2009), b “Hydrogen Material Safety Data Sheet”, Specialty Gases of America, Inc., Toledo.

Speciality Gasses of America, Inc. (2009), c “Fluorine Material Safety Data Sheet”, Specialty Gases of America, Inc., Toledo.

Speciality Gasses of America, Inc. (2009), d “Hydrogen Fluoride Material Safety Data Sheet”, Specialty Gases of America, Inc., Toledo.

Talaia, MAR (2007) “Terminal Velocity of a Bubble Rise in a Liquid Column”, *World Academy of Science, Engineering and Technology*, 28, 264-268.

Walsh, FC (1993) *A First Course in Electrochemical Engineering,* The Electrochemical Consultancy (Romsey) Ltd., Romsey, England.

Welty, JR, Wicks, CE, Wilson, RE, Rorrer, GL (2001) *Fundamentals of Momentum, Mass and Heat Transfer 4th Edition*, John Wiley and Sons, Inc., United States of America.